

## INFORMATION TO USERS

This manuscript has been reproduced from the microfilm master. UMI films the text directly from the original or copy submitted. Thus, some thesis and dissertation copies are in typewriter face, while others may be from any type of computer printer.

**The quality of this reproduction is dependent upon the quality of the copy submitted.** Broken or indistinct print, colored or poor quality illustrations and photographs, print bleedthrough, substandard margins, and improper alignment can adversely affect reproduction.

In the unlikely event that the author did not send UMI a complete manuscript and there are missing pages, these will be noted. Also, if unauthorized copyright material had to be removed, a note will indicate the deletion.

Oversize materials (e.g., maps, drawings, charts) are reproduced by sectioning the original, beginning at the upper left-hand corner and continuing from left to right in equal sections with small overlaps. Each original is also photographed in one exposure and is included in reduced form at the back of the book.

Photographs included in the original manuscript have been reproduced xerographically in this copy. Higher quality 6" x 9" black and white photographic prints are available for any photographs or illustrations appearing in this copy for an additional charge. Contact UMI directly to order.

# U·M·I

University Microfilms International  
A Bell & Howell Information Company  
300 North Zeeb Road, Ann Arbor, MI 48106-1346 USA  
313/761-4700 800/521-0600



**Order Number 9321191**

**Hole burning and pump probe spectroscopy of photosynthetic particles**

**Lyle, Paul A., Ph.D.**

**Iowa State University, 1993**

**U·M·I**  
300 N. Zeeb Rd.  
Ann Arbor, MI 48106



**Hole burning and pump probe spectroscopy  
of photosynthetic particles**

by

Paul A. Lyle

A Dissertation Submitted to the  
Graduate Faculty in Partial Fulfillment of the  
Requirements for the Degree of  
**DOCTOR OF PHILOSOPHY**

Department: Chemistry  
Major: Physical Chemistry

**Approved:**

Signature was redacted for privacy.

**In Charge of Major Work**

Signature was redacted for privacy.

**For the Major Department**

Signature was redacted for privacy.

**For the Graduate College**

Iowa State University  
Ames, Iowa

1993

## TABLE OF CONTENTS

GENERAL INTRODUCTION	1
Explanation of Dissertation Format	1
Photosynthesis	2
Electron Transfer Theory	12
EXPERIMENTAL	26
Samples	26
Pump Probe	27
Hole Burning	37
SECTION I. PUMP PROBE SPECTROSCOPY OF PROSTHECOCHLORIS AESTUARI	44
INTRODUCTION	45
PAPER I. EVIDENCE FOR ULTRAFAST EXCITON LOCALIZATION IN THE Q <sub>y</sub> BAND OF A BACTERIOCHLOROPHYLL A-PROTEIN FROM <i>PROSTHECHOCHLORIS AESTUARI</i>	53
ABSTRACT	55
INTRODUCTION	56
EXPERIMENTAL SECTION	58
RESULTS	60
AKNOWLEDGEMENTS	66
REFERENCES	67
PAPER II. DYNAMIC LINEAR DICHROISM IN CHROMOPROTEINS	68
ABSTRACT	70
INTRODUCTION	71
RESULTS AND DISCUSSION	73
Dynamic Linear Dichroism of Chromoproteins in Solution	73

Dynamic Linear Dichroism in Oriented Monolayers	87
AKNOWLEDGEMENTS	93
REFERENCES	94
SECTION CONCLUSIONS	96
SECTION REFERENCES	97
SECTION II. PUMP-PROBE AND HOLE BURNING SPECTROSCOPY OF PHOTOSYSTEM I PARTICLES	99
INTRODUCTION	100
Review of PSI	100
Electron Transfer Theory	107
PAPER I. TEMPERATURE DEPENDENCE OF ANTENNA EXCITATION TRANSPORT IN NATIVE PHOTOSYSTEM I PARTICLES	120
ABSTRACT	122
INTRODUCTION	123
EXPERIMENTAL METHOD AND DATA ANALYSIS	127
RESULTS	131
DISCUSSION	140
Delocalized Phonon Model	140
Localized Phonon Model	144
REFERENCES	152
SECTION CONCLUSIONS	155
SECTION REFERENCES	156
SECTION III. HOLE BURNING STUDIES OF REACTION CENTER COMPLEXES FROM PURPLE BACTERIA	159

INTRODUCTION	160
Bacterial Reaction Centers	160
Hole Burning Theory	165
 PAPER I.    HIGH RESOLUTION SIGNAL TO NOISE PHOTOCHEMICAL HOLE-BURNED SPECTRA OF PROTONATED AND DEUTERATED REACTION CENTERS OF <i>RHODOBACTER SPHAEROIDES</i>	 174
INTRODUCTION	176
EXPERIMENTAL	181
THEORY OF THE HOLE PROFILE	185
RESULTS	189
Experimental and Simulated Spectra	189
Zero Phonon Hole Widths	199
Temperature Dependencies of the ZPH Intensity and Width	199
DISCUSSION	204
Dependence of the ZPH Width on Site Excitation	
Frequency ( $\omega_B$ )	204
The Underlying Structure of P870	208
Modeling of the Low Frequency "Phonons"	209
The Special Pair Marker Mode $\omega_{sp}$	211
REFERENCES	218
 SECTION CONCLUSIONS	 222
SECTION REFERENCES	223
GENERAL CONCLUSIONS	226
GENERAL REFERENCES	228
ACKNOWLEDGEMENTS	232
APPENDIX A: RATE EQUATION PROGRAMS	234
APPENDIX B: HOLE CALCULATION PROGRAM	243



## GENERAL INTRODUCTION

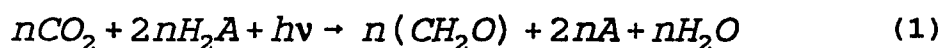
### Explanation of Dissertation Format

This dissertation contains the candidate's original work on spectral hole burning of reaction center proteins from *Rhodobacter Sphaeroides* and pump probe spectroscopy of *Prosthecochloris aestuarii* and native photosystem I particles (PSI). Section I contains two published papers which describe a theoretical treatment of time dependent linear dichroism and its application to exciton localization in the Q<sub>y</sub> band of a bacteriochlorophyll *a*-protein from *P. aestuarii*. Section II contains one published paper which reports the temperature dependence of polarized photobleaching dynamics in the chlorophyll *a* antenna of native PSI particles using 680 nm pump probe experiments. Section III contains one unpublished work describing hole burning of the reaction center protein from deuterated and protonated *Rb. sphaeroides* and the application of a linear electron phonon coupling theory to the hole profiles. A general introduction is a preface to the dissertation and each section contains a more specific introduction pertinent to the work described in that section. Because of the different subjects discussed in each of the sections the referencing is done to keep each section separate. Within each section references for the papers are found immediately after that paper. The referencing for the introduction of each section is found at the end of that section after the conclusions. References for the general introduction are found at the end of the dissertation following the general conclusions.

## Photosynthesis

All energy used or stored on the earth ultimately comes from sunlight. Photosynthesis is the process by which plants, algae, and bacteria absorb sunlight and store the energy as chemical potential. The aim of much of photosynthesis research is devoted to determining how these organisms capture and store the sun's energy. This work is concerned with how the light energy is captured and the resulting electronic excitation turned into a stable charge separated state.

One reason for studying photosynthesis is the enormous energy that is available from the sun. Of the  $15 \times 10^{23}$  Joules/year of energy that strikes the earth's surface only .2%, or  $3 \times 10^{21}$  Joules/year, is actually stored through photosynthesis in the form of carbohydrates (equation (1)) [1].



Equation (1) shows that carbon dioxide is reduced by  $H_2A$  ( $H_2O$  in the case of plants,  $H_2S$  in the case of purple sulfur bacteria) with light energy to form carbohydrate  $n(CH_2O)$ . If man could learn to capture even the smallest percentage of the energy potential of the sun (man's current energy usage is .02% of the sun's energy that reaches the earth) many of today's energy related problems could be greatly reduced.

Even though photosynthetic organisms have solved the problem of capturing and storing sunlight, they are by no means efficient in doing so. When consideration is given to losses due to unusable photons striking the organism, incomplete absorption of the photons

that are usable, loss due to degradation of the energy after initial capture, and loss due to the reactions which produce carbohydrate, photosynthesis has a net efficiency of approximately 5% [1]. However, the very initial processes of photosynthesis with which this work is concerned are very efficient. Almost 100% of the photons that are absorbed reach the charge separated state [2,3]. The organisms have achieved such high quantum yields by limiting the back reactions of the charge stabilization chain, which is one of the major stumbling blocks of today's attempts at mimicking photosynthesis. By studying the primary events of photosynthesis, an artificial device may one day be constructed which can store energy from the sun with a high enough efficiency to be competitive (in terms of cost) with other forms of energy.

Photosynthesis occurs in green plants inside of the chloroplast. Chloroplasts are membrane bound organelles, saucer-shaped, 4-10  $\mu\text{m}$  in length and approximately 1 $\mu\text{m}$  thick. They are located towards the inside edge of the cell wall and vary in number from one to several hundred per cell depending on the environment, growing conditions, and type of plant. Chloroplasts have an outer and inner membrane to separate themselves from the cytoplasm and to control the flow of ions and small molecules within the chloroplast (see Figure 1) [1,4].

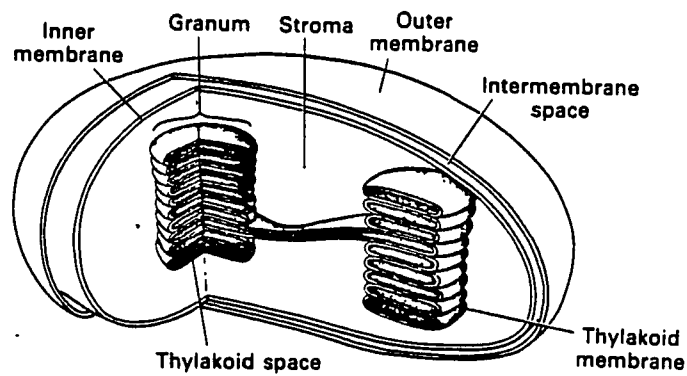


**Figure 1.** Course diagram of a chloroplast showing the membranes and the thylakoid (reprinted with permission from reference 4)

With the use of electron microscopy and freeze fracture techniques, the structure of the chloroplast was determined. The inner membrane surrounds the stroma which contains soluble enzymes and in turn surrounds membranous structures called thylakoids. Stacks of thylakoids are named granum and the granum are connected by unstacked regions of thylakoid called stroma lamellae. The thylakoid membrane holds the photosynthetic apparatus and is where the primary events occur. The membrane is composed of similar amounts of lipids and proteins. Some of the lipid constituents are 40% galactolipids, 10% phospholipid, and 4% sulfolipids. There are two types of proteins, integral membrane and peripheral membrane. Integral membrane proteins span the entire lipid membrane and have hydrophobic and hydrophilic regions. The hydrophobic region is within the membrane where the lipids act to exclude most molecules and ions from crossing the membrane. The hydrophilic regions are outside of the membrane and act to bind the peripheral membrane proteins.

Figure 2 shows a schematic of the thylakoid membrane and the approximate location of the Photosystem I (PSI) and PSII complexes. These complexes are actually composed of many different proteins. The proteins known as the light harvesting antenna complexes bind photoreceptor molecules which absorb light of a particular wavelength [5,6]. There are three major classes-of photoreceptors in photosynthetic proteins. These are chlorophylls, carotenoids, and phycobilins. The carotenoids and phycobilins act as accessory pigments in that they absorb energy in a particular part of the spectrum and transfer the energy to proteins which contain chlorophyll molecules [7]. The chlorophyll then transfer the energy on to the reaction centers. The carotenoids are also believed to function as a photooxidation protector

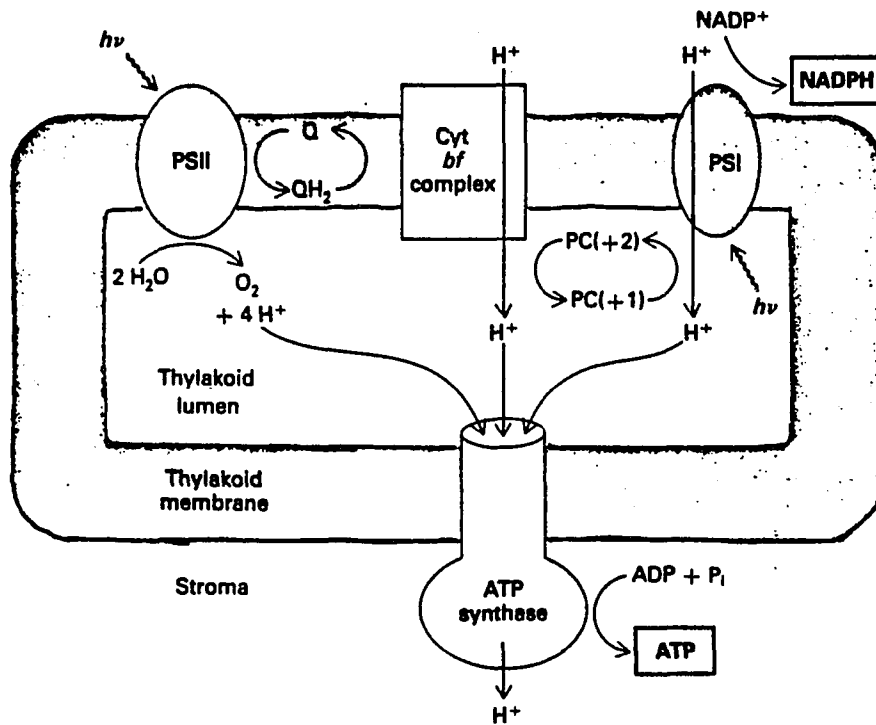


**Figure 2.** Arrangement of PSI and PSII in the thylakoid membrane  
 Note that a net  $\text{H}^+$  gradient is produced in the lumen which is used to synthesize ATP (reprinted with permission from reference 4)

of the chlorophylls in excess light. The absorption characteristics of the pigments are shown in Table I. Depending on the living conditions of the species (land, in shallow water, in deep water etc.) different amounts of the pigments will be involved in the energy trapping. The reaction center is a protein complex that has the special job of trapping the energy from the light harvesting antenna complexes. The reaction center consists of chlorophylls, pheophytins, quinones, iron sulfur centers, and other molecules depending on the organism which are arranged in a specific manner which facilitates efficient charge separation. Typically in plants there are several hundred chlorophyll antenna per reaction center. The reaction centers are named to indicate the position of maximum absorption change upon light illumination. PSI and PSII are labeled P700 and P680 (P for pigment) which indicates that the maximum absorption change occurs near 700 nm and 680 nm respectively. After charge separation in PSI, the electron is passed to another protein located on the stromal side of the thylakoid membrane. Here the electron reduces  $\text{NADP}^+$  to NADPH. A similar set of circumstances occurs for PSII which transfers its electron to the cytochrome  $\text{bf}$  complex. During the electron transport process a net  $\text{H}^+$  excess is built up on the luminal side of the membrane. These protons are the driving force for the synthesis of ATP as the proton gradient is lessened through the ATP synthetase complex. The ATP and NADPH can be seen to be the products of the light reactions of photosynthesis. The dark reactions (also known as the Calvin Cycle) in which  $\text{CO}_2$  is converted to carbohydrate are then ready to proceed.

Bacterial photosynthesis is better characterized than that of plants. There are two reason for the difference. One difference is primarily due to the fact that more unified

**Table I**

Maximum Absorption Wavelengths  
of Several Chromophores

Photoreceptor	Absorption Wavelengths
Chl <i>a</i>	400-500 nm &
Chl <i>b</i>	600-700 nm
Bchl <i>a</i>	800-1100 nm
Bchl <i>b</i>	
Caratenoids	
Carotenes	430 nm
Xanthophylls	450 nm
Phycobilins	
Allophycocyanin	650-680 nm
Phycocyanin	620-635 nm
Phycoerythrocyanin	575 nm
Phycoerythrin	545-565 nm



growing conditions can be obtained for bacteria. The second difference is that there is only one photosystem in most bacteria making isolation of protein complexes simpler. There are three groups of photosynthetic bacteria. Cyanobacteria (formerly blue-green algae) are quite similar to green plants in that they have the same two photosystems. The construction of the two photosystems, however, are not the same. The antenna pigment complex called the light harvesting complex I (LHCI) is absent in the cyanobacteria and LHCII is replaced by an outer membrane structure called a phycobilisome. Phycobilisomes project into the stroma and are connected to the thylakoid membrane with linker proteins. The pigment arrangement in the phycobilisomes is unique because they are arranged from the most blue at the distal end to the most red at the proximal end (from the membrane) [8]. Green and purple bacteria have only one membrane which is highly invaginated (called the intracytoplasmic membrane, ICM) in purple bacteria and have one photosystem. The ICM carries the pigmented protein complexes and is active in photosynthesis. Upon breakage of the membrane by mechanical means the ICM form what are known as chromatophores. Green bacteria do not have ICM but instead have chlorosomes (see the introduction for section I for a description) attached to the inside surface of the cell wall which project into the cytoplasm. The chlorosome is an antenna complex whose role is to funnel the captured energy to the reaction center located in the cell membrane.

The main difference of the characterizations between plants and bacteria has come about because of the X-ray crystal structure obtained for the reaction center protein of *Rhodospseudomonis viridis* [9,10,11] and *Rhodobacter Sphaeroides* [12,13].

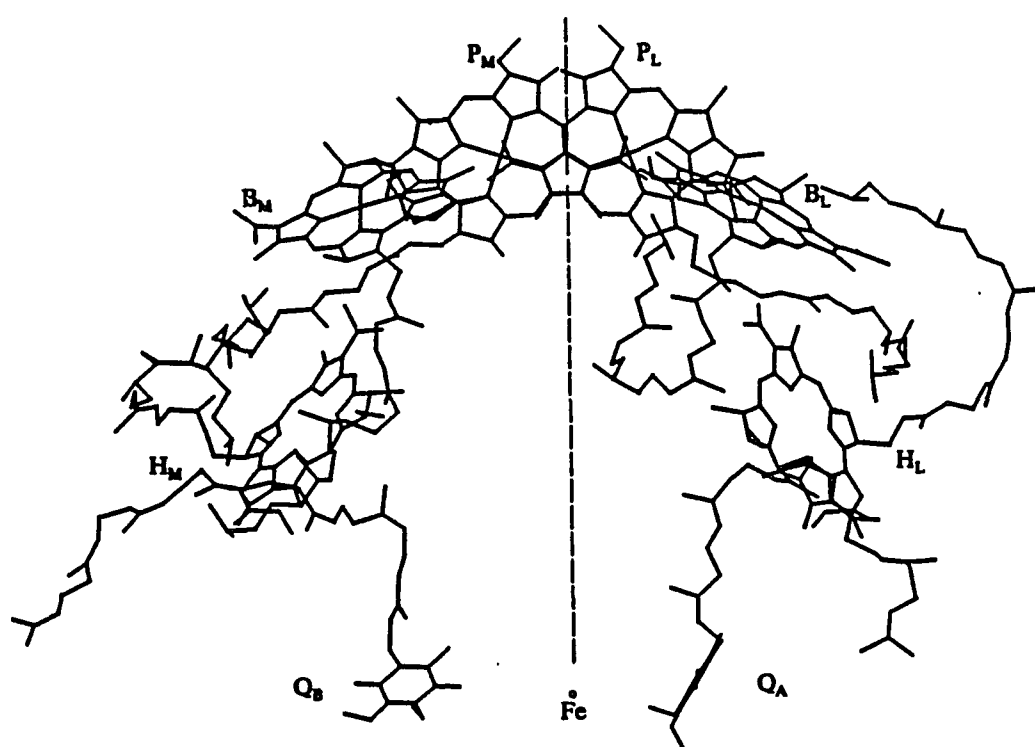


**Figure 3.** Pigment arrangement in the reaction center *Rb. sphaeroides* R-26 within the L and M polypeptides

Figure 3 shows the arrangement of the pigments associated with the reaction center proteins. Missing from the figure are the three polypeptides (H, L, M) that the pigments are associated with. The H polypeptide (28 kd) is unpigmented and is loosely bound to the L (31 kd) and M (36 kd) polypeptides. The L and M polypeptides carry the pigments and the pigments are distinguished by which polypeptide they are associated to by denotation with an L or an M. Some purple bacteria (e.g. *Rp. viridis*) also have a c-type cytochrome with four heme groups. A pair of bacteriochlorophyll molecules are held in close proximity to each other to form a dimer structure called the special pair ( $P_L$ ,  $P_M$ ). Approximately 10 Å away (center to center) from the special pair on both arms of reaction center are two monomer bacteriochlorophyll molecules known as the accessory bacteriochlorophylls ( $B_L$ ,  $B_M$ ). Their role in the electron transfer pathway is of on going controversy. Next in line, approximately 16 Å away from the special pair, are two pheophytin molecules ( $H_L$ ,  $H_M$ ) followed by two quinones ( $Q_A$  on the L side and  $Q_B$  on the M side). A non heme iron molecule is held between the two arms of the reaction center along a pseudo  $C_2$  symmetry axis which includes the special pair. Excitation from the antenna bacteriochlorophyll is directed to the special pair which in turn transfers an electron down one arm of the reaction center within 3 ps to the bacteriopheophytin [14,15,16]. The electron is then transferred to  $Q_A$  in about 200 ps [17,18] and then on to  $Q_B$  in 100-200 μs [19,20,21]. Thus, a photon of light energy is turned in to a charge separated state which is stabilized across a membrane.

### Electron Transfer Theory

Since the discovery of an electron transfer reaction from cytochrome *c* to the electron donor cation  $P^+$  in the reaction center of *Chromatium vinosum*, in which the rate of reaction is independent of temperature below 80K and then becomes temperature dependent between 80K and 300K [22,23], nonadiabatic electron transfer theories have been developed [24,25,26] and used by Hopfield [27], Jortner [28], Kakitani and Kakitani [29], and others to explain *C. vinosum*'s remarkable temperature dependence. To date no single analysis of the experimental data has been able to fully account for the temperature dependence while also giving physically relevant parameters, though all the simulations approximate the data accurately throughout the entire temperature range. The following discussion will outline the development of the theory as applied to *C. vinosum* and try to explain why the theory has not been able to explain *C. vinosum*'s temperature dependence for the past 25 years unambiguously. The discussion will also include examples of the theory as applied to the initial electron transfer process in several different bacterial reaction centers.

R.A. Marcus in the late 1950's developed a classical expression for nonadiabatic electron transfer reactions using a full statistical mechanical treatment [30,31,32] (equation (2)).

$$W = \frac{2\pi}{\hbar} |V|^2 (4\pi\lambda kT)^{-1/2} \exp\left(-\frac{(\lambda - \Delta E)^2}{4\lambda kT}\right) \quad (2)$$

$V$  is the electronic interaction matrix element,  $\hbar$  Planck's constant,  $\lambda$  the reorganization energy,  $\Delta E$  the energy gap between the donor and acceptor molecules, and  $kT$  is the temperature in units of wavenumbers ( $\text{cm}^{-1}$ ). Because Marcus treated the vibrations classically, equation (2) is valid only for the high temperature condition  $kT \gg \hbar\omega$ , where the frequency enters in through the dimensionless quantity  $S = S_0 \coth(\hbar\omega/2kT) = \lambda/\hbar\omega$  which is the vibrational coupling parameter.

To explain the low temperature independent rate of *C. vinosum* Hopfield formulated a semiclassical rate equation [27] (equation (3)).

$$W = \frac{2\pi}{\hbar^2 \omega} |V|^2 (2\pi S)^{-1/2} \exp \left( -\frac{(S_0 - P)^2}{2S} \right) \quad (3)$$

Hopfield's equation is seen to be the same as the classical expression with the substitution of  $[\hbar\omega/2]\coth(\hbar\omega/2kT)$  for  $kT$  in equation (2). At high temperatures  $\coth(\hbar\omega/2kT)$  is approximately  $2kT/\hbar\omega$  which, when multiplied by  $\hbar\omega/2$ , gives the classical temperature  $kT$ . However at low temperatures ( $\hbar\omega \gg kT$ ),  $\coth(\hbar\omega/2kT)$  becomes 1 and the rate is then independent of temperature.

The full quantum mechanical rate equation as derived by Jortner is given in equation (4) [28]:

$$W = \frac{2\pi}{\hbar^2 \omega} |V|^2 \exp(-S_0(2\bar{n}+1)) \times \left( \frac{\bar{n}+1}{\bar{n}} \right)^{p/2} I_p(2S_0[\bar{n}(\bar{n}+1)]^{1/2}) \quad (4)$$

where  $I_p$  is the modified bessel function and  $\bar{n} = [\exp(\hbar\omega/kT)]^{-1}$  is the bose factor which gives the average quantum number of the vibration  $\hbar\omega$ . The effect of tunneling is accounted for in this theory which was neglected in the semiclassical expression (see section II for a detailed formulation of equation (4)). In the high temperature limit the quantum mechanical rate becomes equal to the classical rate equation as expected. But at low temperatures, ( $\bar{n} \rightarrow 0$ ) and the rate becomes independent of temperature (equation (5)).

$$W = \frac{2\pi}{\hbar^2\omega} |V|^2 e^{-S_0} \frac{S_0^P}{P!} \quad (5)$$

Comparison of equations (3) and (5) with  $S=S_0$  substituted into equation (3) shows that the semiclassical and quantum mechanical rates at low temperatures are not equal. They do, however, become equal under certain conditions. If the coupling is strong such that  $S \gg 1$  and the reorganization energy is equal to the energy gap ( $P=S_0$  is called the activationless condition) then the semiclassical equation reduces to:

$$W = \frac{2\pi}{\hbar^2\omega} |V|^2 (2\pi S)^{-1/2} \quad (6)$$

and with the use of Stirling's approximation:

$$P! = P^P e^{-P} \sqrt{2\pi P} \quad (7)$$

in equation (5), which is good for  $P > 5$ , equation (5) reduces to equation (6). Thus, for an activationless process under the strong coupling limit the quantum mechanical and semiclassical rate equations are identical. The equality of the semiclassical and quantum

mechanical equations for the activationless and strong coupling limit can be illustrated with the curves in Figure 4. Under the strong coupling limit and when  $P=S_0$  the two curves have large displacement and the crossing point is at the minimum of the upper curve. In this case all the population is sitting at the curve crossing and tunneling processes are nonexistent. In fact, Jortner extends the applicability of the semiclassical equation by defining a pseudoactivationless rate where the two curves cross near the minimum but below  $\hbar\omega/2$ . Conditions for the range of  $S_0$  and  $P$  can then be formulated by forming an energy of activation term from the absolute value of the operand of the exponential in equation (3) and setting it  $\leq \hbar\omega/2$  in the high temperature limit. Straight forward manipulations and extension to both negative and positive values of  $P-S_0$  lead Jortner to derive the condition [33]:

$$1 - (2/S_0)^{1/2} \leq P/S_0 \leq 1 + (2/S_0)^{1/2} \quad (8)$$

which describes the range of  $P$  and  $S$  for pseudoactivationless electron transfer. The error in this approximation is better than 10% for the entire range. Equation (6) can then be used to simulate data under the pseudoactivationless condition.

Jortner [28] in 1976 argued that Hopfield's [27] description of electron transfer (based on the Förster-Dexter theories [34,35]) should not be as applicable to electron transfer as to energy transfer because Hopfield's theory is based on the acceptor and donor molecules coupling to separate sets of oscillators. Jortner also argues against the use of Hopfield's equation at low temperatures because of the fact that the semiclassical equation does not match his full quantum mechanical approach in this regime. As shown above, the two

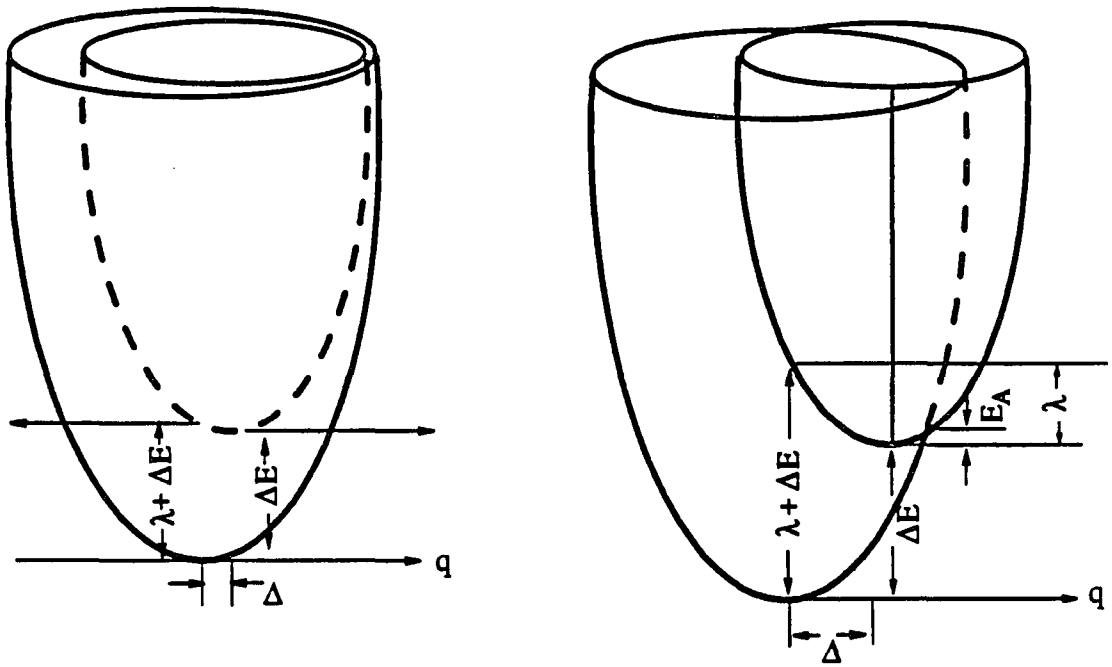


**Figure 4.** Representation of the (a) weak and (b) strong coupling limits  
The strong coupling case holds for  $S \gg 1$  and  $S = P$



equations actually match for the specific case of pseudoactivationless electron transfer. Again, for pseudoactivationless electron transfer tunneling processes have a negligible contribution to the rate due to the region of the crossing point depicted in Figure 4.

Table II shows the parameter values of several simulations attempts of the *C. vinosum* data. As discussed previously, all of these simulations match the data reasonably well over the entire temperature range. However, the range of the parameter values are extremely large. As can be seen in Table II, Hopfield (corrected by Devault [36]) and Jortner's simulations give approximately the same results. Both use a vibrational frequency of near  $400\text{ cm}^{-1}$  which can be attributed to a low frequency intramolecular mode, relatively small energy gaps, and large coupling parameters which leads to large reorganization energies. The latter two values are of concern. Blankenship and Parson (who utilized an energy gap of 0.45 eV estimated from the difference of the midpoint redox potential between  $P^+$  and cytochrome [37]) have argued that these values are too large and Kikuchi and Kikuchi in unpublished molecular orbital calculations for one electron removal in porphyrin molecules, have calculated coupling parameters of 0.5-1.0 [29] as did Warshel and coworkers [1].

To explain the *C. vinosum* data more consistently, Kikuchi and Kikuchi reformulated Jortner's equation to include small changes in vibrational modes upon excitation. Their equation is identical to equation (4) with  $\Delta E$  replaced by  $\Delta G$ . They argue for small values of the reorganization energy based on the hydrophobic nature of proteins. Proteins act to exclude solvent molecules from the area of electron transfer and thus large solvent reorganization should not be possible. Kikuchi and Kikuchi chose an average value for the

18  
Table II

Nonadiabatic Simulation parameters  
From Several Authors

Author	Energy Gap (cm <sup>-1</sup> )	Reorganization Energy (cm <sup>-1</sup> )	Vibrational Frequency (cm <sup>-1</sup> )
Hopfield (1974)	400	8,100	245
Jortner (1976)	800	8000	400
Blankenship and Parson (1979)	3600	17,600	400
Kikatani and Kikatani (1981)	3600 (298K) 7000 (4K)	500	1000
Jortner (1981)	3600	2000 17,500	500 100-300
Jortner (1986)	3480 3480	1125 3480	100 100

intramolecular vibrational frequency of  $1000\text{ cm}^{-1}$  and could then use equation (5) since  $\hbar\omega \gg kT$  for the entire temperature range of the *C. vinosum* data. However, in their theory equation (5) is no longer temperature independent because  $\Delta G$  and, therefore,  $P$  is dependent on the temperature. The simulations calculated with this theory give very reasonable values of the reorganization energy and coupling parameters. Notice that in the Kakitani's theory  $S_0 \ll P$  whereas for Jortner's  $S_0 \gg P$ . Figure 5 shows the consequences of this difference. For small  $S_0$  values, a small change in  $P$  can be seen to quickly change the rate. However, for large  $S_0$  small changes in  $P$  can be seen to have little effect and the temperature dependence must come from broadening the curve of the Frank-Condon factor. One final difference between Kakitani's theory and Jortner's should be addressed. Jortner defines the activationless regime in terms of where his equation gives a very weak temperature dependence. In terms of the parameter values this condition is satisfied when  $S$  is approximately equal to  $P$ . However, in the Kakitani's theory  $\hbar\omega \gg kT$  and a small value of  $\Delta E$  is sufficient to define an activationless regime. Thus, though the equations are the same except for the replacement of  $\Delta E$  by  $\Delta G$ , the theories lead to different conclusions.

In the early part of the 1980's the effects of medium (protein) modes on the electron transfer process started to receive attention. Before this time theorists ignored the medium modes and believed that the intramolecular modes dominated the electron transfer rate. In 1981 Jortner included both a medium mode ( $200\text{ cm}^{-1}$ ) and intramolecular mode ( $500\text{ cm}^{-1}$ ) in his fully quantum mechanical equation [38] (line 5 of Table II shows the result). Jortner again obtains a very large reorganization energy and the effect of the medium mode was to

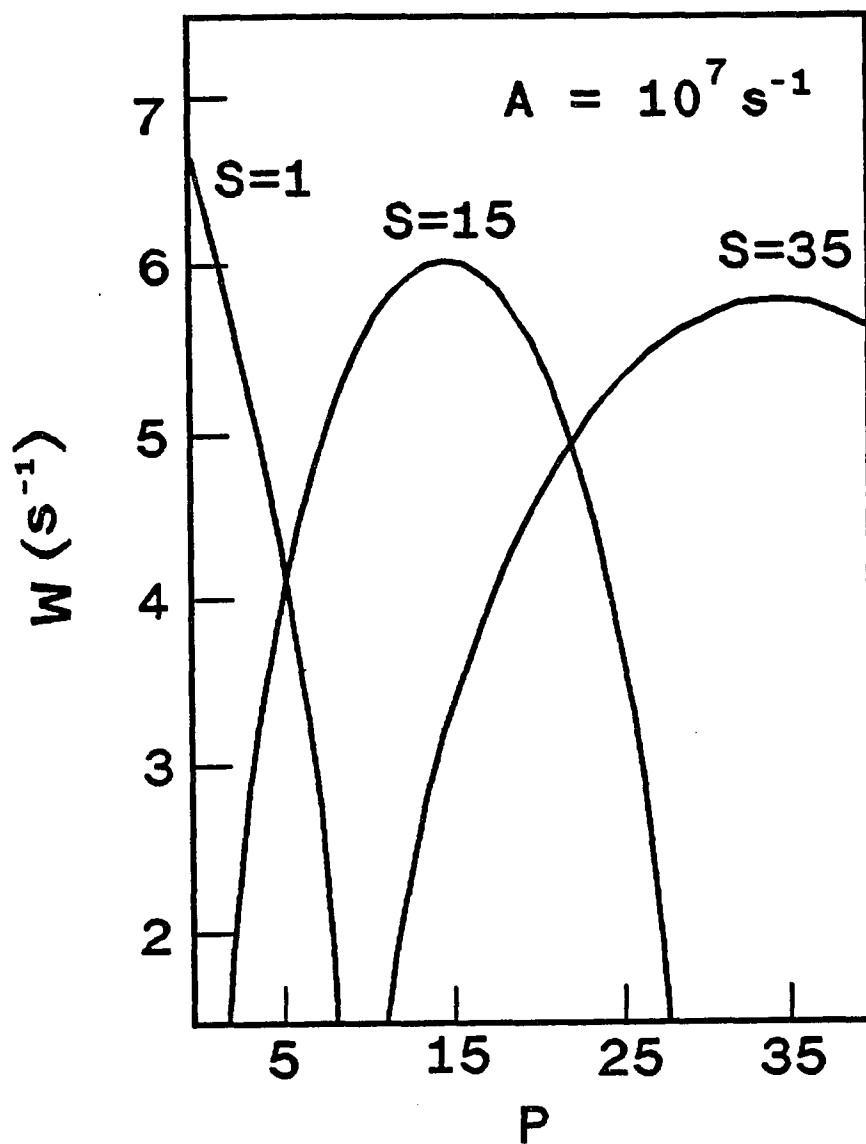


**Figure 5.** Plot of the change in rate ( $W$ ) with  $P$  for three values of  $S$ . Note the change in steepness of the curves for  $S$  changing from small to larger values.

increase the  $V$  matrix to  $90 \text{ cm}^{-1}$ . This value is extremely large for the experimental rates obtained and implies that the donor and acceptor molecules are close together. Calculations with equation (9) using  $V_0 = 10^5 \text{ cm}^{-1}$  and  $\alpha = 1.0 \text{ \AA}^{-1}$ , results in a value of  $7.0 \text{ \AA}$  for the separation.

$$V = V_0 \exp(-\alpha R) \quad (9)$$

Finally, in 1986 when more experimental data had become available, Jortner was able to simulate the *C. vinosum* data with more reasonable parameters [39]. The first of the new data included evidence from other electron transfer processes that low frequencies of  $100 \text{ cm}^{-1}$  could account for essentially activationless temperature dependencies. Second, large values of  $S$  and the use of intramolecular frequencies as the primary modes responsible for the temperature dependence implied, through equation (9), that configurational changes of about  $.7 \text{ \AA}$  for the porphyrin ring are required. Third, the crystallographic data showed that  $V$  should be approximately  $1 \text{ cm}^{-1}$  for the  $23 \text{ \AA}$  distance found between cytochrome *c* and the special pair. To explain the *C. vinosum* data under the new constraints, Jortner needed to invoke two separate electron transfer processes. An activationless process at low temperatures and an activated process for higher temperatures. It is interesting to note that Grigorov and Chernavskii [26] used this assumption to simulate the data in 1972 and DeVault and Chance [22] believed this to be true when the experimental data was first obtained. The crystallographic data also showed that there are two distinct low potential cytochrome *c* molecules in *C. vinsoum* with a separation of  $11 \text{ \AA}$ . Jortner proposed that the more distant

cytochrome was responsible for the low temperature behavior and the closer one was responsible for the activated process. As shown in Table II, the activated process is in the weak coupling limit with a reorganization energy of  $1125 \text{ cm}^{-1}$  and  $V = 0.55 \text{ cm}^{-1}$ . The activationless process ( $P=S_0$ ) gives a much smaller value for  $V$  of  $8 \times 10^{-4} \text{ cm}^{-1}$  and indicates that this process is from the farther removed cytochrome.

Of more relevance to the present work presented in this dissertation is how non-adiabatic electron transfer theories have been used to explain the temperature dependence of the initial electron transfer from the special pair to the pheophytin within the reaction center protein for *Rp. viridis*, *Rb. sphaeroides* and *Rb. capsulatus*. These reactions all speed up from about a factor of one to three times when the temperature is lowered to near 10 K [40,41] (this is often referred to as a negative temperature dependence). Recent papers by Jortner [42], and Fleming et. al. [40] have taken the small temperature dependence of the rate to be an indication of an activationless process. Both use equation (6) to simulate the data of *Rp. viridis* and *Rb. sphaeroides* obtaining  $\hbar\omega = 100 \text{ cm}^{-1}$  and  $\Delta E = \lambda = 2000 \text{ cm}^{-1}$  which gave adequate representations of the data sets. However, the *Rp. viridis* data was not well simulated for temperatures above 200K. This discrepancy was explained by supposing that  $V$  is temperature dependent through unspecified protein contractions. Recent data suggest that protein contractions probably could not be large enough to account for the difference [43,44].

Recently Small et. al. [45] have attempted to explain Fleming et. al.'s data with nonadiabatic electron transfer theory in the strong coupling limit. They used hole burning

data to obtain relevant vibrational frequencies and reorganization energies. A two mode model was used and parameter values of  $S_1 = 7$ ,  $\omega_1 = 30 \text{ cm}^{-1}$ ,  $S_2 = 1.1$ ,  $\omega_2 = 135 \text{ cm}^{-1}$ ,  $\lambda = 360 \text{ cm}^{-1}$ , and  $\Delta E = 300 \text{ cm}^{-1}$  are obtained from the simulation. The strong coupling limit as derived by Englman and Jortner [46] gives essentially equation (6). The conditions under which the strong coupling limit is relevant are  $S \gg 1$  and  $\Delta E \equiv \lambda$ . By averaging the vibrational frequencies and  $S_0$  values used by Small et. al. ( $\omega = 75 \text{ cm}^{-1}$  and  $S_0 = 4.5$ ) and with the use of equation (8), the above conditions of the strong coupling limit are seen to be met with the parameters values used. However, the *Rp. viridis* simulation suffered from the same high temperature mismatch as Jortner and Fleming et. al.'s did. Instead of explaining the mismatch with a protein contraction, Small et. al. used a temperature dependent energy gap sighting the known red shift of approximately  $300 \text{ cm}^{-1}$  upon lowering the temperature from room temperature to 4 K for the P870 and P960 states. The new simulation for *Rp. viridis* becomes acceptable throughout the entire temperature range, and that of *Rb. sphaeroides* is essentially unchanged.

The  $\Delta E$  dependence of temperature is reminiscent of Kakitani and Kakitani's theory based upon frequency changes between the ground and charge separated states for the full quantum mechanical treatment. The Kakitanis also explained an electron transfer reaction of the type  $P^*A \rightarrow P^+A^-$  and the back reaction by a straight forward change in  $\Delta G$ . Theories that do not include a temperature dependent energy gap can not explain both forward and back electron transfer processes without invoking protein contractions with temperature change or the use of soft modes (low vibration protein modes) of vibration.

Very recently Lin et. al. [47] have used a multimode nonadiabatic theory in the strong coupling limit to explain the changes of rate with temperature for several mutants of *Rb. capsulatus*. In their work they use  $S_0$  values for vibrational frequencies obtained from Warshel [48] which includes four intramolecular modes and two medium modes. They contend that in their calculations the negative temperature dependence is not a special condition of the system (no need to invoke an activationless process), but comes naturally from the multi-modes incorporated in the calculations. Lin et. al. go on to show how the different rates can be explained with adjustments in  $\Delta E$  and  $V$  for all the mutants studied.

One note about the applicability of nonadiabatic electron transfer theories to the initial step of electron transfer in reaction centers should be emphasized. The conditions under which the theory is applicable are [49]: 1)  $V$  is small and 2) the vibrational relaxation time must occur on a faster time scale than the electron transfer. A defining line between adiabatic and nonadiabatic is usually drawn about one order of magnitude above the point of maximum rate. The maximum rate is equal to the vibrational frequency of the mode divided by the speed of light, which gives a rate of approximately 3 ps for a  $100\text{ cm}^{-1}$  mode [50].

Recent experiments [51,52] have cast doubt on the applicability of the nonadiabatic theory for the initial electron transfer step. The experiments give evidence for coherence of a 700 fs and a 2 ps oscillation implying that electron transfer occurs during the vibrational relaxation time. The frequency range of these oscillations ( $15\text{-}80\text{ cm}^{-1}$ ) is in the range of proteins modes, but below the frequency ( $\sim 120\text{ cm}^{-1}$ ) of the special pair characterized from hole burning experiments [53]. These experiments also suggest the



possibility that the slow back transfer rate could be due to the loss of coherence through dissipation of vibrational energy in the newly formed state. Theoretical studies have been published that consider whether vibrational coherence and/or electronic coupling could play a role in the primary electron transfer [54,55,56].

As has been shown by the preceeding discussion, there are several reasons why non-adiabatic electron transfer theories have not been able to explain the temperature dependence of the electron transfer reaction from cytochrome to  $P^+$  in *C. vinosum* unambiguously. The foremost problem is that the equations can explain the temperature dependence of *C. vinosum* quite well for a large range of parameter values. Therefore, it is very important to have reliable experimental values for as many of the parameters as possible. One important parameter to obtain is the reorganization energy. In most of the simulations a very large reorganization energy was used. For electron transfer reactions in proteins the reorganization energy is expected to be much smaller. A second reason is the possibility proposed by Jortner that actually two separate electron transfers are proceeding. If the theory has been attempting to fit the curve to a single reaction and there are actually two, then the theory would not give reasonable parameters. A final possibility that was proposed by Kakitani and Kakitani is whether the energy gap should be treated as temperature dependent. Several groups have shown that the energy gap in the initial electron transfer reaction of *Rb. sphaeroides* and *Rp. viridis* is temperature dependent. [57,58] (For an opposing view see [59].)

## EXPERIMENTAL

### Samples

For pump probe experiments, the samples were adjusted to give an optical density of 2-2.5 in a 1 cm path length cell. Two different samples were used for the studies reported in this dissertation. Native photosystem I particles, PSI-200, were kindly provided by Dr. John H. Golbeck. The particles had a chl *a* to P700 ratio of approximately 200 and an overall chl *a* to chl *b* ratio of about 6. PSI-200 was extracted from spinach chloroplasts by the procedure of Mullet et. al. [60] and Golbeck [61]. The particles were suspended in a buffered glycerol/water mixture at PH 8.0 and contained .1% Triton X-100. The water soluble Bchl *a*-protein from *Prosthecochloris aestuarii* was generously provided by Dr. Roger E. Fenna. The samples were dissolved in a mixture of Tris buffer and water and used as received.

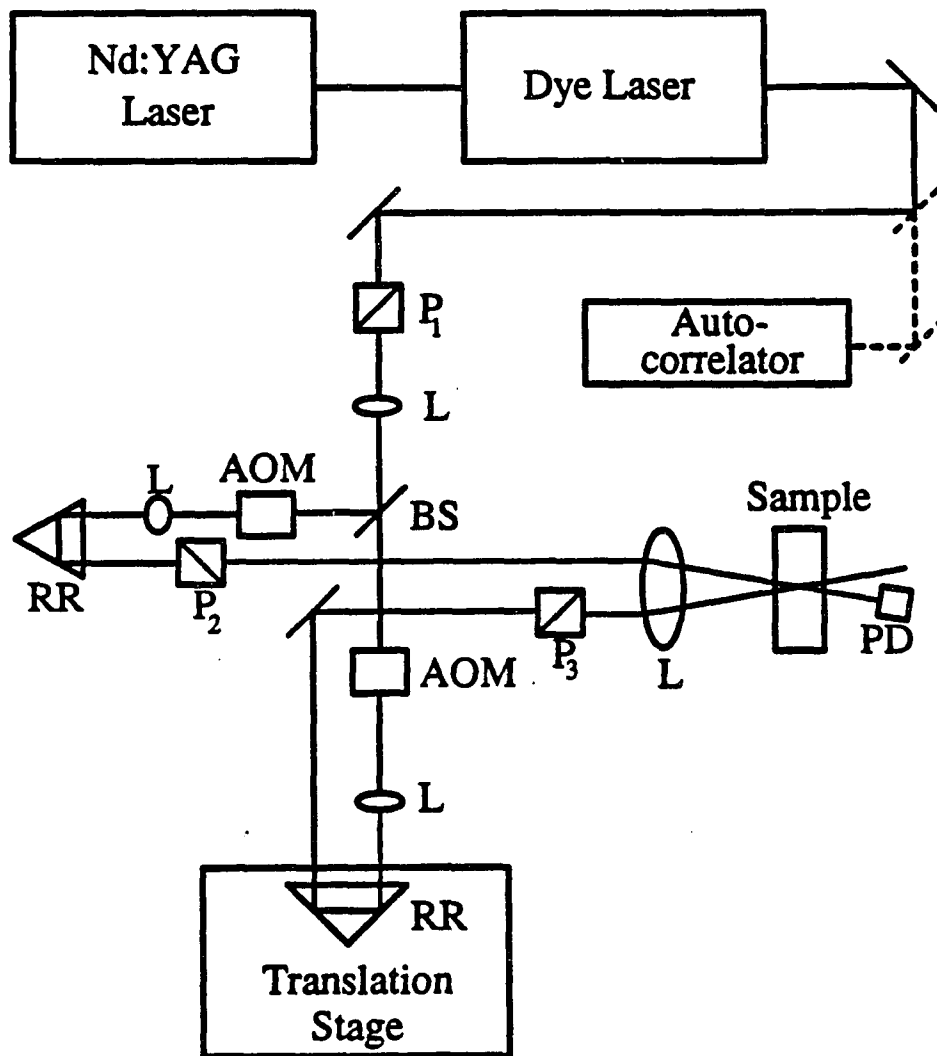
For the hole burning studies, samples were diluted with a glycerol/water solution to approximately .4 optical density units at 4 K. Two different types of samples were studied. Photosystem I particles from *Synechococcus sp. PCC 6301* (*Anacystis nidulans*) were provided by Dr. John H. Golbeck. The particles were isolated using the method of Parrett et. al. [62] except that n-dodecyl- $\beta$ ,D-maltoside was substituted for Triton X-100 in the solubilization step. No chl *b* molecules are present in *Synechococcus* and the chl *a* to P700 ratio is about 100. Reaction center protein samples of deuterated *Rb. sphaeroides* and protonated R-26 were provided by Dr. David M. Tiede.

### Pump Probe

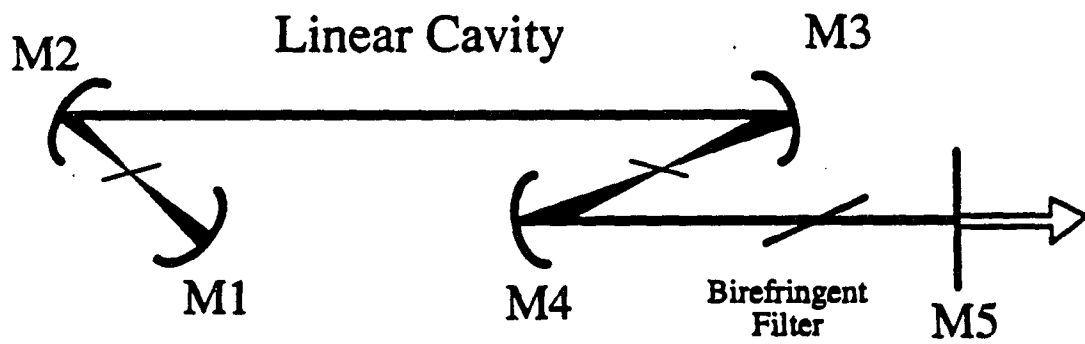
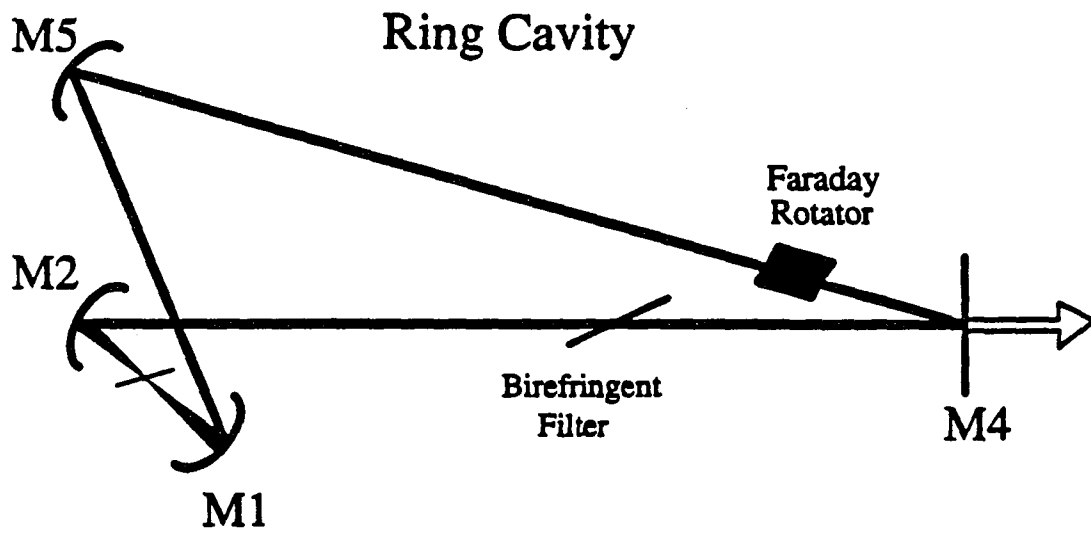
In the pump probe spectroscopic technique, a sample is excited with a short (a few picoseconds or shorter) pump pulse and at a delayed time a second probe pulse interrogates the sample. The change in transmission (photobleaching) of the sample is plotted versus the delay time between the pulses creating a plot which describes the ground state recovery of the sample. The technique does not rely on the speed of any measuring devices, but only on the pulse width used. Recently a very detailed explanation of the laser system, optical arrangement, signal detection, and computer control used in the present experiments has been given [63]. Therefore, only an overview of these topics will be discussed here. Instead, a thorough explanation of the sample preparation and handling will be described for the low temperature experiments developed for the present work.

Figure 6 shows a schematic representation of the experimental setup. One watt of the frequency doubled 532 nm output from a Coherent CW mode-locked Nd:Yag (70 ps pulsed at 76 MHz repetition) was used to synchronously pump an in house built dye laser. The dye laser arrangement is depicted in Figure 7. Two different dye lasers were used with different mirror radii ( $R$ ). The first dye laser had  $R = 10$  cm for M2 and M3 and  $R = 5$  cm for M4 and M5. The output coupler (M1) was typically 95% reflecting. Wavelength tuning was accomplished with a 0.5 mm thick single-plate birefringent filter. The second dye laser was different in that  $R = 15$  cm for M4 and  $R = 7.5$  cm for M5. Also shown in Figure 7 is the saturable absorber jet (between mirrors M4 and M5) which was used to further shorten the pulse width. The combination of saturable absorber (passive mode-locking) and synchronous

**Figure 6.** Optical arrangement for the pump-probe experiments used to study photosynthetic systems See text for a description of the low temperature sample setup



**Figure 7.** A) Optical arrangement of the ring dye laser used for the hole burning studies  
B) Optical arrangement of the linear dye cavity used for obtaining picosecond pulses



pumping is known as hybrid mode-locking [64]. Two different laser dye/saturable absorber combinations were used. For wavelengths between 760 nm and 825 nm Styryl 8/Ir140 was used and for wavelengths between 650 nm and 685 nm DCM/DDCI was used. A cavity dumper was also used in some of the experiments to further reduce the pulse width and to allow for changes in the output repetition rate. The laser power ranged from 30 mw to 120 mw depending on the arrangement used. The dye laser output was routed to a real time auto correlator of local design for pulse width determination (2-3 ps was routinely obtained). By inclusion of a mirror before the correlator the laser beam could be steered into the pump probe optics. The beam was first sent through a clean up polarizer ( $P_1$ ) to ensure vertical polarization then divided by an inconel-coated beam splitter (BS) and the pump and probe beams focused into identical Isomet 1206C acoustooptic modulators (AOM). The probe beam was typically modulated at 6.5 MHz and the pump at 0.5 MHz. The sum of the two modulations was detected with phase locked signal-sideband detection at an EG&G FOD-100 photodiode (PD) by a Drake R-7A radio receiver. The receiver demodulated the 7 MHz incoming signal into a 50 KHz intermediate frequency, which was detected with a Stanford Research Systems SR-510 Lock-in amplifier. Pump probe scans were stored in a Dec Minc-23 computer and later analyzed by a convolute and compare algorithm [] with a Dec Vax 2000 workstation. The polarization of the probe beam ( $P_2$ ) was set at  $45^\circ$  with a calcite Glan-Thompson polarizer while that of the pump beam ( $P_3$ ) was variable from  $-45^\circ$  to  $+45^\circ$  with respect to the probe polarization. Both arms of the optical arrangement include a retro reflector (RR), and collimating lenses (L). The pump beam was changed in time with respect



to the probe using a BK-7 corner cube prism mounted on top of a Micro-Control UT100125PP (.1  $\mu\text{m}$  steps, 12.5 cm range) translational stage. The two beams were overlapped in the sample using a 7.3 cm focal length lens and care was taken to ensure that the overlap was unchanging for the full range of delay times used in the experiments.

Low temperature measurements increased the difficulty in obtaining high signal to noise decay curves in several ways. The main problem with the measurements was the attainment of an optically clear glass. Without a clear, crack free region to steer the laser through, signal would be lost due to scattering. To obtain a good glass three features had to be optimized. First, the sample windows needed to be smooth and free of dirt. Glass cracking will be initiated from any nonuniform area on the surface. Not only should the windows be free of scratches, but the part of the neoprene spacer which comes into contact with the sample must also be as smooth as possible. Replacement of either the windows or the spacer may be necessary to achieve an optically clear glass even if no problem is readily apparent. Next, the ratio of glycerol to water used as the glass forming solvent must be manipulated for each different photosynthetic particle. The thinness of the spacer (.1cm) makes the solvent ratio a critical parameter in forming a clear glass. Typical ranges for the glycerol to water ratio used was from 60/40 to 80/20. Finally, to achieve a clear glass, as much of the sample as possible must fill the neoprene spacer. Any large bubble that may become trapped in the spacer will allow for severe cracking to occur. Therefore, great care should be used in filling the spacer and positioning the windows.

Keeping the sample in the sample holder while cooling was also a problem. The displax first required rough pumping for approximately 10 minutes to evacuate the sample chamber and then took another 20 minutes once the cooling began to freeze the sample. Thus, a sample arrangement was designed that was both airtight and still flexible enough to not strain the sample once it was frozen. Another problem of sample design was to allow for temperature measurement. To be sure of the temperature achieved with the displax, a thermocouple was placed in direct contact with the sample. Again sealing of the sample to the vacuum was a concern as was obtaining a clear glass around the thermocouple. One final problem, not as difficult at room temperature as at low temperatures, was the focusing of the pump and probe beam at the sample. At room temperature the sample could be moved with respect to the focusing lens, but because the displax was bulky, it was firmly attached to the optical table. Since the sample is separated from the outer window of the displax by several inches, overlapping of the pump and probe beams at the sample surface was harder to see and obtainment of the signal somewhat more time consuming.

The displax (an Air Products DE202 closed-cycle He expander module) is composed of two cooling stages (Figure 8). The first stage is capable of cooling the helium gas to 35 K, while the second stage further reduces the temperature to 10 K as measured by a chromel/Au-0.7% Fe thermocouple permanently mounted at the end of the second stage. The sample holder is screwed into the second stage and a 3.8 cm diameter nickel plated copper cylindrical shroud with 2 cm diameter windows is placed over the sample and mounted to

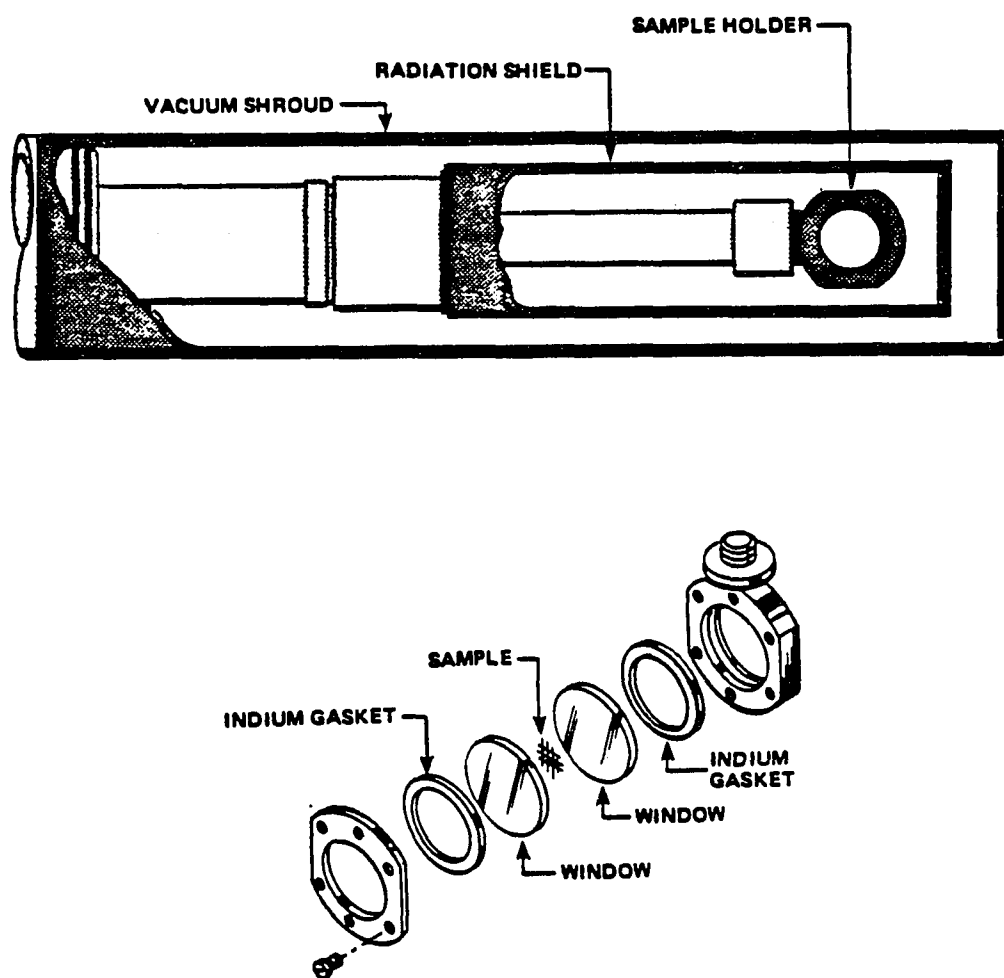


**Figure 8.** Top: Schematic of the helium displacer used for the low temperature pump probe studies  
Bottom: Sample arrangement used with the displacer

the first cooling stage. As mentioned above the displer can cool the sample to below a standard glycerol/water freezing point in about 20 minutes and then takes about another 30 minutes to obtain 10 K at the end of the cold finger. The sample temperature routinely obtained about 35 K to 40 K.

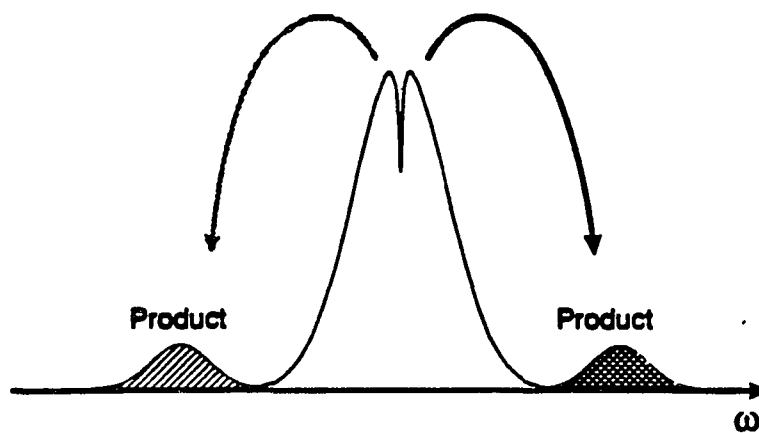
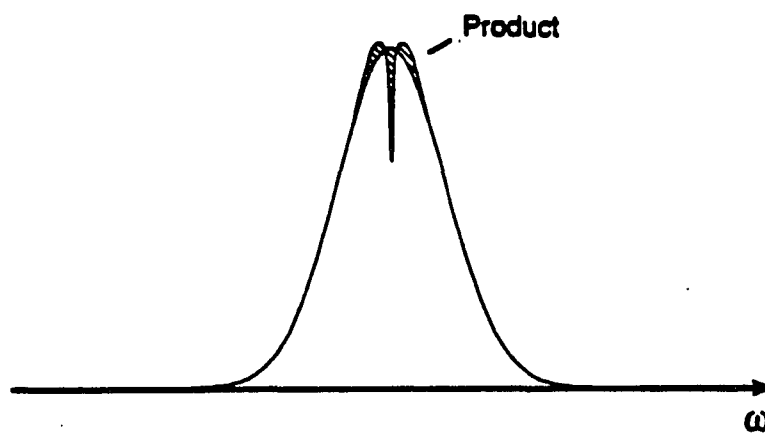
The sample holder was composed of nickel plated copper. The holder separates into two parts to facilitate sample mounting (Figure 8). Indium foil was placed around the inside edge of both halves of the holder to increase the thermal contact between the holder and the glass windows. A 0.1 cm thick neoprene spacer was lightly greased on both sides and placed on one of the glass windows. A small slit was cut into the neoprene to accommodate the copper-constantan (type T) calibrated thermocouple. The thermocouple had to be brought into the displer and heat sunk so that it did not warm the sample. This was accomplished by bringing the thermocouple into the displer through a small hole (which was then sealed) and then wrapping it securely down the entire length of both the first and second stages. The thermocouple was either glued to the neoprene or lightly greased into place. The sample was then loaded into the center of the neoprene spacer and the second window screwed into place sandwiching the sample and spacer. Ideally the sample completely filled the space in the neoprene but a small bubble of air trapped in with the sample proved to be of little consequence for glass formation. The sample optical density was set to between 0.2 and 0.3 absorbance units for the 0.1 cm optical path length.

### Hole Burning

Hole burning is a site selective spectroscopy whereby a narrow band laser beam is used to excite a small number of molecules in an inhomogeneously broadened absorption band. The resulting narrow features exhibited can be examined to determine excited state lifetimes, homogeneous and inhomogeneous contributions to the absorption band, vibronic features, exciton couplings, electron-phonon coupling strengths, and Franck-Condon factors.

In Figure 9 two types of hole burning mechanisms are illustrated. Photochemical hole burning results from excitation of impurity molecules which undergo photochemistry while in the excited state. Typically the products absorb outside the absorption band leaving behind a narrow hole in the band. Nonphotochemical hole burning is a photophysical phenomenon which results when an excited molecule upon return to the ground state experiences a change in the local environment. A net increase in absorption (anti-hole) is seen within approximately  $100\text{ cm}^{-1}$  of the spectral hole which can extend for several hundred  $\text{cm}^{-1}$  more. Hayes and Small [65,66] have proposed that the mechanism for nonphotochemical hole burning is from phonon assisted tunneling between glassy states of two level systems. A third type of hole burning called transient hole burning can be seen when a population bottle neck is produced in the excited state. Transient hole burning has been detected through both a long lived triplet state and a charge separated state ( $P^+Q^-$ ) with a slow charge recombination time [53,67]. As long as the laser continually excites the sample a steady state transient population persists and a hole spectrum can be obtained.

**Figure 9.** Absorption changes seen for photochemical (PHB) and non-photochemical (NPHB) hole burning

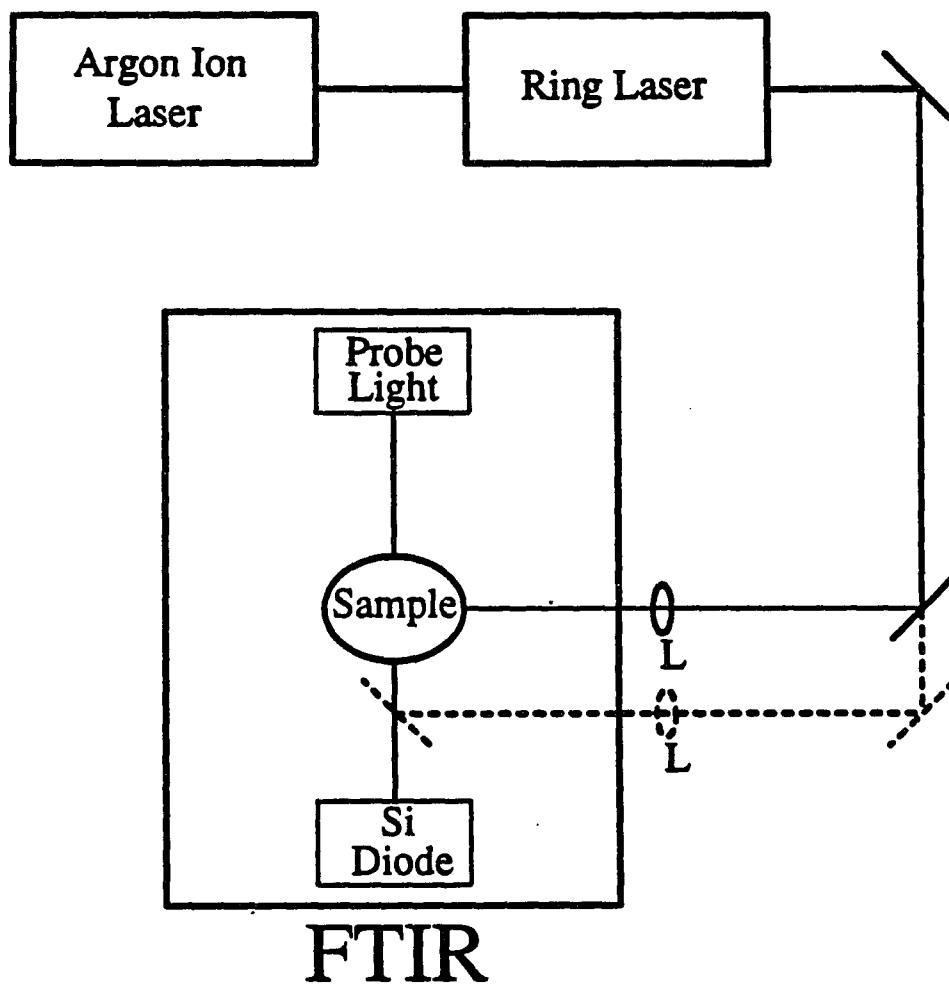
**Photochemical Hole Burning (PHB)****Non-photochemical Hole Burning (NPHB)**

The spectral line width of the aforementioned hole is related to the time domain through the equation  $T_2 = (2\pi c\Gamma_h)^{-1}$  where  $c$  is the speed of light and  $\Gamma_h$  is the homogeneous line width [see 68,69 for reviews of hole burning]. Where  $T_2$  is the total dephasing time given by  $1/T_2 = 1/2T_1 + 1/T_2^*$ .  $T_1$  processes lead to the depopulation of the excited state through such mechanisms as fluorescence, internal conversion, and intersystem crossing. The  $T_2^*$  process is the time that the initial phase coherence of the excited molecules caused by the laser excitation is lost through interactions with low energy lattice vibrations. In the systems studied for the present work  $T_2^*$  processes do not contribute to the overall line width by more than approximately  $0.02 \text{ cm}^{-1}$  [70] (typical line widths measured were  $3\text{-}5 \text{ cm}^{-1}$ ) and have been ignored.

Two separate laser systems were used for the hole burning studies in this work. Both lasers were pumped by a Coherent Innova Argon laser. Figure 10 shows an outline of the optical arrangement. For persistent hole burning an Innova 90 (6 watt output) was used to pump a Coherent 699 ring dye laser. The transient experiments were performed with an Innova 200 (15 watt output) pumped Coherent 899 Ti/Sapphire ring dye laser (see Figure 7). For both sets of experiments a Bruker IFS 120 HR fourier transform infrared spectrometer (FTIR) was used to measure the absorption spectra. The laser beam was copropagated with the FTIR probe beam in the case of persistent holes and for the transient hole burning studies the laser was arranged perpendicular to the probe beam. Calibration of the laser wavelengths was achieved by directing the output of ring lasers directly into the FTIR. A calibration



**Figure 10.** Optical setup for both persistent (dashed extension) and transient hole burning experiments



—— Transient  
----- Persistent

curve could then be constructed and reproducible wavelength selection (within  $1\text{ cm}^{-1}$ ) was obtained for a broad range of wavelengths.

Obtainment of high signal to noise ratios in these experiments was necessary for two reasons. First, low hole burning efficiency was found with photosystem I particles from *Synechococcus*, where hole depths of only 1-2% were typical across most of the absorption band. The other reason was for improvement of the on going assessment of the hole burning theory developed by Hayes et. al. [71] By improving on the previous experiments, a more critical evaluation of the simulations could be carried out (e.g. how good are the parameters obtained and are there more vibrations present) as the parameter values would be more restricted in range than in previous simulations. To obtain the higher signal to noise spectra reported here a trial and error method was invoked. Different sample preparations, sample holders, optical densities, and scanning parameters for the data acquisition were tried. Eventually optimized spectra were taken under the conditions of 0.4 O.D., and settings on the FTIR of 200 scan averages, velocity set to 5, and the resolution set to  $2\text{ cm}^{-1}$ . The scan time was 7 minutes under these conditions. The sample holder design differed from previous ones in that the sample was mounted in the center of four fins designed to block scattered laser light. Though the holder was larger and more cumbersome to use than previous designs, alignment was assured to be as good as possible once the sample was in place due to the fact that the probe beam alignment holes matched the size of the probe beam focus points.

SECTION I.

PUMP PROBE SPECTROSCOPY OF  
*PROSTHECOCHLORIS AESTUARI*

## INTRODUCTION

*Prosthecochloris aestuarii* is a green sulfur bacteria that grows in the lower depths of lakes and ponds. Because little light reaches below the top portion of the water due to absorption by other organisms, *P. aestuarii* has developed extensive light harvesting systems [1]. Electron and freeze fracture micrographs show the size of the chlorosomes (the light harvesting assembly) in *P. aestuarii* cells vary from 100 to 300 nm in length and from 50 to 100 nm in width [2]. A model of the chlorosome is shown in Figure 1 [3]. The chlorosome is shown attached to the inside of the cell wall. The main light harvesting elements are long rods (10 to 30 in each chlorosome) of a Bacteriochlorophyll *c*-protein. The rods are approximately 10 nm in diameter and contain closely packed Bchl *c* molecules; 12 to 14 for every 15 kDa of protein. The Bchl *c*-protein rods are separated from the reaction center protein by a crystalline baseplate. The baseplate contains a Bchl *a*-protein complex and has a periodicity of approximately 6 nm. The reaction center (about 30 per chlorosome) is associated with a noncrystalline Bchl *a*-protein in large 10 to 14 nm diameter particles embedded in the cytoplasmic membrane.

The Bchl *a*-protein from the baseplate of *P. aestuarii* was the first chlorophyll containing protein complex to have its structure determined. The structure was first obtained by X-ray diffraction at 2.8 Å resolution in 1975 by Fenna and Matthews [4]. More recently, the resolution has been increased to 1.9 Å [5] and the complete amino acid sequence determined [6]. The Bchl *a*-protein is unique from other chlorophyll containing proteins

---

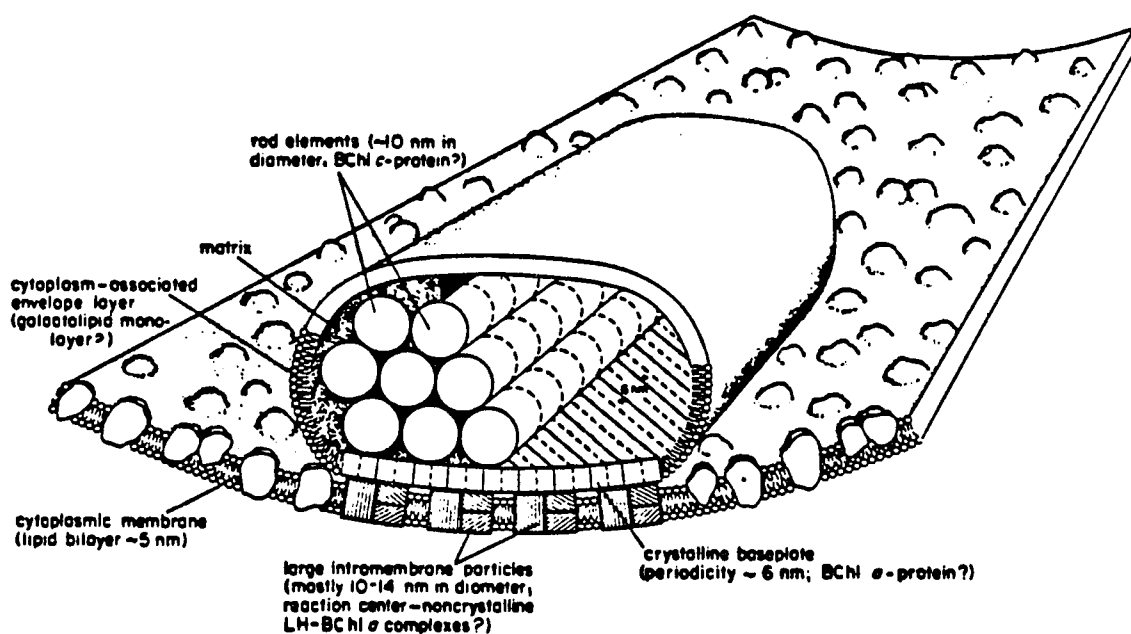


**Figure 1.** Structure of the chlorosome of the green sulfur bacterium *Chlorobium limicola* based on freeze fracture micrographs (from reference 3)

because it is water soluble and can be easily separated and purified [7]. Olson et al. determined the proper criteria for obtaining crystals of the protein [8] and because their crystals were used by Fenna and Mathews for the structural determination, the protein complex is usually referred to as the Fenna, Mathews, Olson (FMO) complex.

The basic structure of the protein was found to be a trimer consisting of identical subunits related through a three-fold symmetry axis (see Figure 2). Each subunit contains seven Bchl *a* molecules surrounded by the protein. The chlorophyll molecules are held in place by hydrogen bonding with the protein and additionally, five of the seven bacteriochlorophylls have a histidine ligand associated with their magnesium atom. Extensive interactions exist between protein chains of the different subunits and is supportive of the observation that the trimer can not be split apart without being denatured [9]. The Bchl *a* molecules within the subunit (Figure 3) have no apparent symmetry, but all lie within 40 degrees of a common plane. Nearest-neighbor magnesium to magnesium separations are 11 to 14 Å and the edge to edge separation of the subunits are 24 to 36 Å.

Because of the close proximity of the Bchl *a* molecules to each other within a subunit, it is expected that spectroscopies should show evidence for strongly interacting exciton states (see reference 10 for a description of excitons). Low temperature absorption spectra of the  $Q_y$  region show four major bands and structure that indicates the existence of sub bands. Whitten et al. [11,12] analyzed the absorption and circular dichroism (CD) spectra using fourth and eighth derivative spectroscopy and succeeded in identifying seven peaks. The

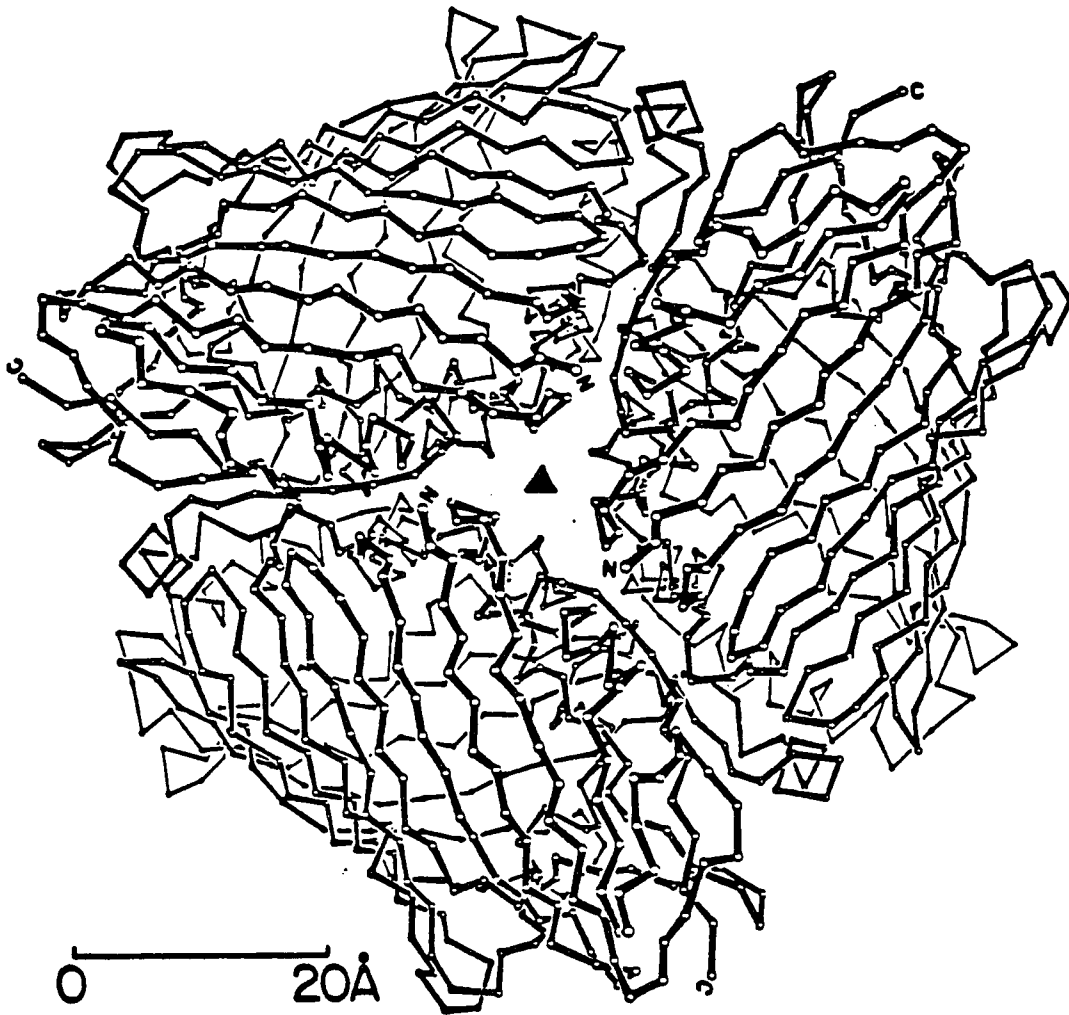


**Figure 2.** Bchl *a*-protein trimer showing the C-3 symmetry. The Bchl *a* moieties have been omitted for clarity



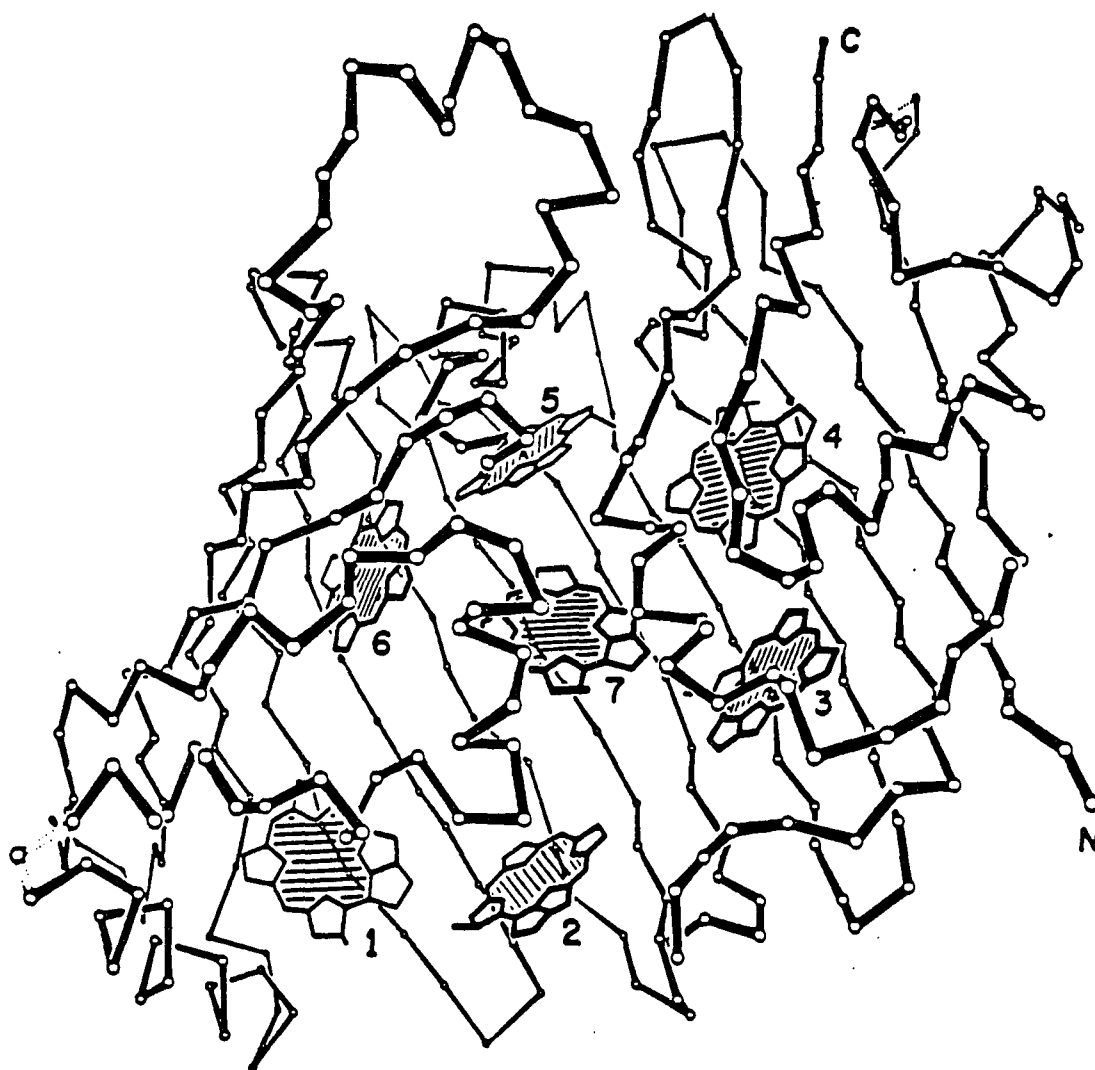


**Figure 3.** One subunit of the trimer shown in Figure 2 showing the seven Bchl *a* chromophores in their protein environment. The phytol chains are not shown

peaks could be assigned to seven states due to exciton splittings of the seven Bchl *a* molecules in one subunit. The CD spectra also showed evidence of exciton states since it sums to zero (i.e. conservative) and is larger in magnitude than CD spectra of monomeric Bchl *a* [13,14]. Theoretical modeling using five to seven components were attempted by several groups [13,14,15,16,17]. Of these groups, Pearlstein and coworkers have done the most in progressing the theoretical treatment of the  $Q_y$  region. Pearlstein and Hemenger [15] used both simple exciton theory in the point monopole approximation and degenerate ground state theory to model the  $Q_y$  absorption and CD spectra with little success. Of major difficulty was the assignment of the environmental shift due to the protein around each Bchl *a* molecule. A better fit was provided when Pearlstein and Hemenger artificially assigned the lowest transition to be  $Q_x$  instead of  $Q_y$ . However, Lutz et al. [18] using Resonance Raman spectroscopy established the lowest transition was indeed the  $Q_y$ .

Pearlstein, using a different approach, allowed for interactions between Bchl *a* molecules in different trimers [16]. The calculations were based on the assumption that at low temperature the protein aggregates producing  $\beta$ -sheet contacts. The contact should then produce strong excitonic interactions between Bchl's in different trimers. Because two subunits were thought to be in contact, the interaction matrix required for the calculation was expanded to 14 by 14 instead of 7 by 7. Pearlstein also used three different diagonal energies for the seven Bchl *a* molecules based on the protein interactions with each. Good fits for either the CD or absorption spectrum were possible, but not for both at the same time.

---

Finally, a reasonable theoretical fit to the experimental absorption and CD spectra has been obtained by Pearlstein based on standard assumptions [19]. All previous attempts either gave poor fits or have been based on unorthodoxed or unreasonable assumptions to obtain good fits. In Pearlstein's most recent attempt, the more reasonable approach of including all 21 Bchl *a* molecules of the same trimer in the calculations was presented. Exciton stick spectra and gaussian synthesis of absorption and circular dichroism (CD) spectra were obtained using standard methods [17]. Pairwise interactions of all the Bchl's were also included and calculated in the point monopole approximation. Fourteen distinct exciton states emerge from the 21 Bchl *a* molecules when the C-3 symmetry is accounted for in the calculation. The largest interaction energy calculated for intersubunit interactions that would introduce effects of the C-3 symmetry was  $16.3 \text{ cm}^{-1}$  for the three Bchl molecules labeled number seven (Fenna-Matthews numbering scheme). The intrasubunit interaction energies, on the other hand, are between 50 and  $200 \text{ cm}^{-1}$ . Therefore, unless the site wavelength (absorption position of a particular molecule) for the intersubunit interactions of the Bchl-7 molecules are very different from the rest, the intrasubunit interactions are expected to dominate [20].

In the calculations, Pearlstein chose 825 nm for the site wavelength of Bchl-7 instead of the 802.6 nm used in previous studies. Other site wavelengths were chosen by first calculating the tendency for other pairs of interactions to shift the absorption of the Bchl-7 molecules. The "shift tendency" was used to reduce the number of calculations required to simulate the CD and absorption spectra. The resulting calculated spectra fit reasonably well.

Comparison of the site wavelengths obtained from the calculations with hole burning experiments of Johnson and Small [21], which detected eight of these states, show good agreement for the long wavelength half of the Q<sub>y</sub> region. For shorter wavelengths, however, the positions and widths of the transitions are poor. With better knowledge of the spectral shapes needed for each band (gaussian, lorentzian, or other), and refinement of the procedure to allow for computer searching of the site wavelengths, Pearlstein believes that better agreement with experiment is possible in the future.

PAPER I. EVIDENCE FOR ULTRAFAST EXCITON  
LOCALIZATION IN THE Q<sub>y</sub> BAND OF  
BACTERIOCHLOROPHYLL *a*-PROTEIN  
FROM *PROSTHECHOCHLORIS AESTUARII*

Evidence for Ultrafast Exciton Localization  
in the Q<sub>y</sub> Band of Bacteriochlorophyll *a*-protein  
from *Prosthecochloris aestuarii*

P. A. Lyle and W. S. Struve

*Journal of Physical Chemistry* 1990, 94, 7338

**ABSTRACT**

Time-dependent linear dichroism was observed for several wavelengths in the  $Q_y$  band of the Bchl  $a$ -protein antenna complex from *Prosthecochloris aestuarii*, and photobleaching spectra were obtained for evidence of exciton localization. The results indicate that excitation transport in this antenna proceeds largely through incoherent hopping between localized states at times longer than 2 ps.

## INTRODUCTION

The bacteriochlorophyll *a*-protein antenna complex from the green sulfur bacterium *Prosthecochloris aestuarii* is one of the very few photosynthetic systems whose three-dimensional structure is well characterized. [1,2] Despite this, the mechanics of its involvement in electronic excitation transport (EET) from the light-harvesting chlorosomes to the reaction center are still largely unknown, and even the interpretation of its 809 nm  $Q_y$  absorption spectrum is unsettled. [3-5] It has long been recognized [6] that the Bchl *a* molecules, which are complexed by trimeric protein subunits into three symmetry equivalent groups of seven chromophores, must be strongly exciton coupled with dipole-dipole interaction energies as large as 200 cm<sup>-1</sup>. [3] The low temperature  $Q_y$  absorption spectrum exhibits at least five nonvibronic components [7] at 825, 814, 805, 800, and 793 nm. While the failure of simple exciton models to account for the absorption and CD band intensities has cast doubt on their excitonic origin, spectral hole-burning studies have unequivocally established that they arise in large part from exciton splittings. [7,8] Excitation of the Bchl *a*-protein with the burn wavelength 800.0 nm at 4.2 K, for example, produces satellite holes whose intensities and positions correlate with those of the major bands in the  $Q_y$  spectrum. These experiments uncovered the existence of at least eight distinct exciton components, indicating that the laser prepared states may be delocalized over more than one subunit containing seven chromophores.



A key mechanistic question is the extent to which the coherence of the laser prepared exciton states is preserved during the course of EET. van Grondelle suggested in 1985 that vibrational motion in the protein environment should randomize the phases in the coherent states within  $10^{-14}$  to  $10^{-15}$  s, leading to decoupling and excitation localization. [9] Johnson and Small observed zero-phonon hole widths at 4.2 K corresponding to 100 fs lifetimes [7] in all but the two lowest energy exciton components and attributed this to downhill relaxation between exciton components. In this work, we examined polarized photobleaching in the  $Q_y$  system of the Bchl *a*-protein from *P. aestuarii* at 805, 809, and 814 nm. In an earlier pump-probe study, [10] photobleaching depolarization occurred with 4.8 ps decay time in the 603 nm  $Q_x$  band and was interpreted in terms of excitation hopping between protein subunits organized in the crystallographic  $p6_3$  hexagonal structure. [1] In addition to extending the pump-probe studies to the more familiar  $Q_y$  system, we have obtained  $Q_y$  photobleaching spectra for spectral evidence of ultrafast energy redistribution.

## EXPERIMENTAL SECTION

The Bchl *a*-protein was dissolved in a mixture of Tris buffer and water, and its optical density at 809 nm was adjusted to 2.0 in a 1 cm path length. Samples were placed between  $\lambda/4$  fused silica flats separated by an 800  $\mu\text{m}$  Teflon spacer for pump-probe experiments and rotated at 12 Hz to avoid laser photooxidation during scans.

A hybrid mode-locked synchronously pumped Styryl 8/IR-140 dye laser was excited by 532 nm, 70 ps pulses at 76 MHz repetition rate from a CW mode-locked Nd:YAG laser. A cavity dumper slewed the repetition rate to 19 MHz, sharpening the autocorrelation function to 2 to 3 ps fwhm (depending on wavelength). The pump and probe beams were modulated at 6.5 and 0.5 MHz, respectively, with Isomet 1206C acoustooptic modulators. The pump beam was variably delayed by a translatable BK-7 corner cube prism driven by a Micro-Controle UT100125PP translational stage (0.1  $\mu\text{m}$  steps, 12.5 cm range). The probe polarization was maintained at  $45^\circ$  from the vertical laser polarization with a calcite Glan-Thompson polarizer, while the pump polarization was alternated among parallel, perpendicular, and  $54.7^\circ$  magic-angle polarizations. The pump-probe optics reduced the average beam powers incident on the sample to  $<5$  mW; the two beams (initially parallel and separated by 8mm) were focused into the sample with an 8 cm focal length lens. An EG&G FOD-100 photodiode detected the transmitted probe beam. The signal-bearing 7.0 MHz sum frequency was detected and converted into a 50 KHz intermediate frequency (IF) signal in a phase-locked single-sideband scheme using a modified Drake R-7A radio receiver. The IF

signal was demodulated with a Stanford Research Systems SR-510 Lock-in amplifier. Pump-probe scans were stored in a DEC MINC-23 computer, and convolute-and-compare analyses were performed on a DEC VAX-2000 workstation.

## RESULTS

A  $Q_y$  photobleaching spectrum was accumulated by normalizing the magic-angle pump-probe signal at 10 ps after excitation to the square of the laser power and to the static absorption spectrum at 17 wavelengths between 792 and 825 nm. The results, indicated by data points in Figure 1, are contrasted with the room temperature  $Q_y$  static absorption spectrum. Some of the signal at wavelengths  $\geq 810$  nm may arise from stimulated emission (SE) as the low temperature Bchl  $a$ -protein fluorescence spectrum peaks at  $\sim 830$  nm. [7] Since the Einstein absorption and SE coefficients are identical for singlet-singlet transitions, the integrated SE spectrum cannot exceed the integrated photobleaching spectrum. Hence, the spectrum in Figure 1 cannot be dominated by SE at wavelengths  $\leq 810$  nm and shows clearly that the static spectrum is no longer uniformly bleached after 10 ps. A similar spectrum (not shown) was obtained at 2 ps. Hence, the laser prepared exciton states have decayed into localized excitations by this time, and the Bchl  $a$ -protein photobleaching has accumulated in the lower energy side of the  $Q_y$  spectrum. The dashed line in Figure 1 is the static absorption spectrum multiplied by the Boltzmann factor  $\exp(-\epsilon/kT)$  for  $T = 300$  K, where the excitation energy  $\epsilon$  is referenced to that of the lowest exciton component at 827.1 nm. [7]

Figure 2 shows polarized photobleaching profiles for *P. aestuarii* at 814 nm, the wavelength of the strongest absorption band in the low temperature  $Q_y$  spectrum. The early ratio of parallel to perpendicular signals is considerably less than 3, which is significant

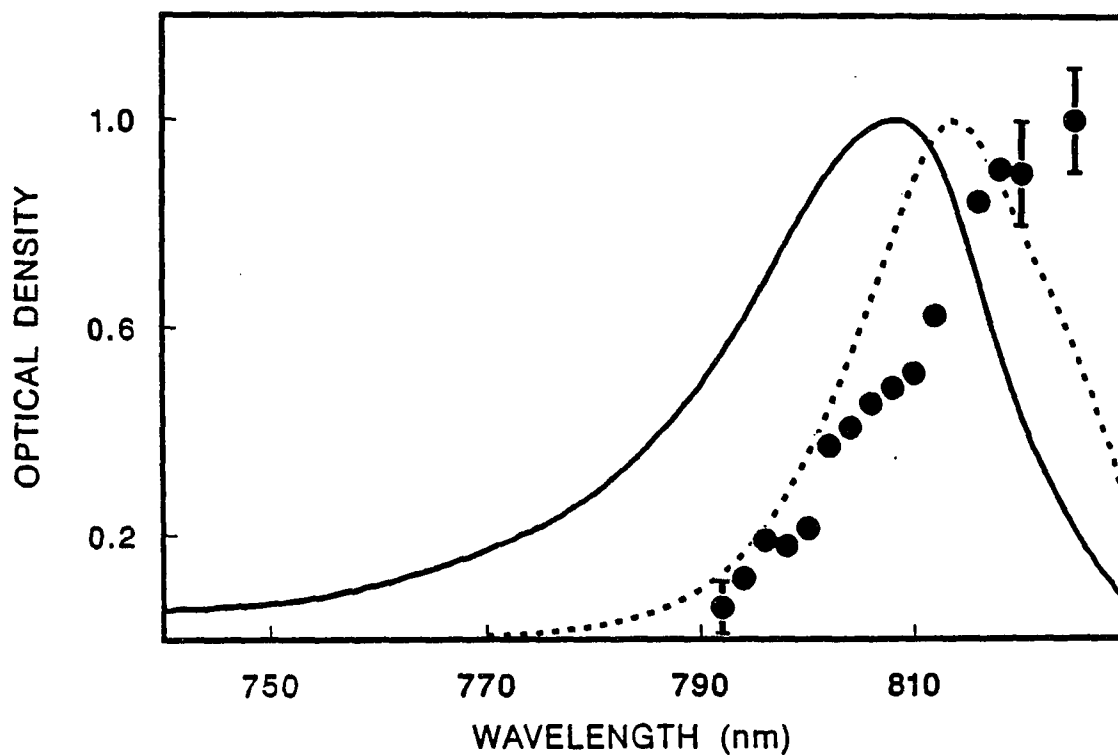


**Figure 1.** Room temperature  $Q_y$  spectra for Bchl  $a$ -protein from *Prosthecochloris aestuarii*: static absorption spectrum weighted by Boltzmann factor  $\exp(-\epsilon/kT)$  relative to the 827.1 nm  $Q_y$  zero point level, dashed curve; and magic-angle photobleaching intensity normalized to the square of the laser power, data points

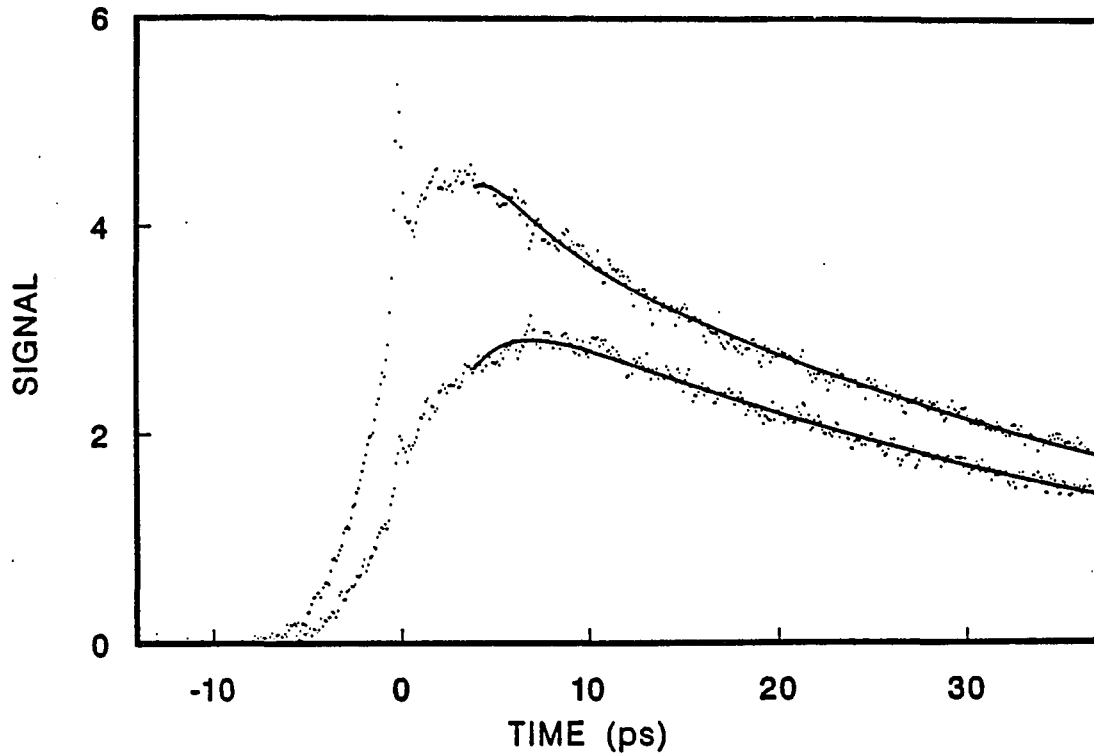


**Figure 2.** Polarized photobleaching transients for Bchl *a*-protein from *P. aestuarii* at 814 nm. Upper and lower curves are for probe pulses polarized parallel and perpendicular to the pump pulse. Continuous curves are optimized convolutions of the laser autocorrelation function with equation 3 using single-exponential decay function  $s(t) = \exp(-t/\tau)$  with  $\tau = 2.3$  ps

because it must initialize to 3 upon excitation in the absence of intrinsic depolarization in any orientationally isotropic chromoprotein solution. [11] The form of the polarized transients in such solutions is necessarily

$$I_{\parallel}(t) = P(t) [1 + 0.8 [(1 - a) s(t) + a]] \quad (1a)$$

$$I_{\perp}(t) = P(t) [1 - 0.4 [(1 - a) s(t) + a]] \quad (1b)$$

where  $P(t)$  is the isotropic decay function evaluated by using magic-angle probe pulses,  $s(t)$  is an anisotropic decay function characterizing depolarization arising from EET, and  $a$  is a residual anisotropy parameter that depends on the (nonrandom) chromophore organization within the protein. [11] Since these expressions imply that  $I_{\parallel}(0)/I_{\perp} = 3$ , we analyzed the profiles with a more general depolarization model. In this scheme, excitation in the laser prepared coherent state A is rapidly transferred to an intermediate state B (e.g., through exciton localization) and is then transferred to a third state C through an EET process whose kinetics are described through the decay function  $s(t)$ . The polarized transients then assume the form

$$I_{\parallel}(t) = P(t) [\langle \mu_{Ax}^2 \mu_{Bx}^2 \rangle s(t) + \langle \mu_{Ax}^2 \mu_{Cx}^2 \rangle [1 - s(t)]] \quad (2a)$$

$$I_{\perp}(t) = P(t) [\langle \mu_{Ax}^2 \mu_{By}^2 \rangle s(t) + \langle \mu_{Ax}^2 \mu_{Cy}^2 \rangle [1 - s(t)]] \quad (2b)$$

where  $\mu_{Ax}$  denotes the laboratory fixed x-component of chromophore A's transition moment, etc., and the brackets  $\langle \rangle$  denote averaging over the protein orientations. Designating the

protein fixed transition moment directions of chromophores A, B, and C as (0,0,1), ( $a_1, b_1, c_1$ ), and ( $a_2, b_2, c_2$ ), respectively, then leads to

$$I_{\parallel}(t) = P(t) [1 + 0.8 [(\rho_1 - \rho_2) s(t) + \rho_2]] \quad (3a)$$

$$I_{\perp}(t) = P(t) [1 - 0.4 [(\rho_1 - \rho_2) s(t) + \rho_2]] \quad (3b)$$

instead of equation 1. Here  $\rho_1$  and  $\rho_2$  are residual anisotropy parameters that are related to the orientations of Chromophores B and C by [11]

$$\rho_1 = 1/2 (3 c_1^2 - 1) \quad (4a)$$

$$\rho_2 = 1/2 (3 c_2^2 - 1) \quad (4b)$$

In this model, the polarization ratio has already decayed to  $(1 + 0.8\rho_1)/(1 - 0.4\rho_1)$  at the earliest observation times; it then approaches  $(1 + 0.8\rho_2)/(1 - 0.4\rho_2)$  at long times, with kinetics determined by  $s(t)$ . Linked convolute and compare analyses of 805, 809, and 825 nm profiles using a single exponential  $s(t)$  with lifetime  $\tau$  converged to  $\rho_1 = 0.95 - 1.05$  (i.e.,  $c_1 \sim 1$ ; cf. equation 4a), indicating that a two step depolarization model is unnecessary for this antenna. Optimized values for the other two parameters were  $0.15 < \rho_2 < 0.35$  and  $2.3 \text{ ps} < \tau, 3.9 \text{ ps}$ . In this analysis, the low initial polarization ratio in Figure 2 occurs because the relatively broad autocorrelation function rounds off the early picosecond decay in  $I_{\parallel}(t)$ . These depolarization lifetimes indicate that the anisotropy decays after the excitation is localized (Figure 1), meaning that much if not all of the depolarization in Figure 2 arises from incoherent EET between localized states. The prior thermalization step (which probably



occurs within one subunit according to the "pebble mosaic" model [6]) does not contribute to the observed depolarization, because single wavelength anisotropy decays are not sensitive to uphill/downhill EET processes. While the laser prepared states may be delocalized over a trimer of subunits [7], the appearance of depolarization in Figure 2 shows that they evolve into less symmetrically excited states before 2 ps. No further depolarization can occur after a trimer has become uniformly excited, unless the 3-fold exciton state symmetry is broken through localization.

We summarize a possible EET scenario for this antenna as follow. Relaxation between exciton components requires  $\sim 100$  fs at 4.2 K [7] and may be somewhat faster at higher temperatures. Incoherent EET hopping to subunits adjacent to the one in which the excitation localizes requires 2 to 4 ps, as manifested by the anisotropy decays. By symmetry, little depolarization accompanies further EET to more remote subunits [10] as the excitation migrates toward the reaction center. The intermediate processes of exciton thermalization and localization are complete before 2 ps.

## ACKNOWLEDGEMENTS

We are indebted to R. E. Fenna for donation of the Bchl  $\alpha$ -protein, to T. P. Causgrove for assistance in the initial stages of this work, and to G. J. Small for helpful discussions. We are grateful to W. E. Catron for supporting one of us (P. A. L.) through a Research Fellowship. The Ames Laboratory is operated for the U. S. Department of Energy by Iowa State University under Contract No. W-7405-Eng-82. This work was supported by the Office of Basic Energy Sciences.

## REFERENCES

1. Fenna, R. E.; Ten Eyck, L. F.; Matthews, B. W. *Biochem. Biophys. Res. Commun.* 1977, 75, 751
2. Tronrud, D. E.; Schmid, L. F.; Matthews, B. W. *J. Mol. Biol.* 1986, 188, 443
3. Pearlstein, R. M.; Hemenger, R. D. *Proc. Natl. Acad. Sci. USA* 1978, 75, 4920
4. Gudowska-Nowak, E.; Newton, M. D.; Fajer, J. *J. Phys. Chem.* 90, 94, 5795
5. Pearlstein, R. M. In *Photosynthetic Light-Harvesting Systems*; Scheer, H., Schneider, S., Eds.; De Gruyter: Berlin, 1988, p. 155
6. Philipson, K. D.; Sauer, K. *Biochemistry* 1972, 11, 1880
7. Johnson, S. G.; Small, G. J. *J. Phys. Chem.* 1991, 95, 471
8. Johnson, S. G.; Small, G. J. *J. Phys. Lett.* 1989, 155, 371
9. van Grondelle, R. *Biochim. Biophys. Acta* 1985, 811, 147
10. Causgrove, T. P.; Yang, S.; Struve, W. S. *J. Phys. Chem.* 1988, 92, 6790
11. Lyle, P. A.; Struve, W. S. *Photochem. Photobiol.* 1991, 53, 359

**PAPER II. DYNAMIC LINEAR DICHROISM  
IN CHROMOPROTEINS**

**Dynamic Linear Dichroism in Chromoproteins**

**Paul A. Lyle and Walter S. Struve**

*Photochemistry and Photobiology*, 1991, 53, 359

**ABSTRACT**

The time-dependent polarized fluorescence and optical density transients arising from electronic excitation transport are derived for solutions of randomly oriented chromoproteins in which the chromophore transition moments have well-defined orientations with respect to the protein. The treatment is extended to oriented monolayers of chromoproteins, in which the molecules are aligned with a particular protein-fixed axis perpendicular to the surface plane and with random azimuthal angles about the surface normal. The initial ratio of parallel to perpendicular transients is invariably 3 : 1, irrespective of system dimensionality and chromophore organization. The residual anisotropy observed at long times is directly related to the relative orientations of the donor and acceptor chromophores. These calculations form a basis for detailed interpretation of ultrafast fluorescence and pump-probe linear dichroism studies in photosynthetic systems, for which 3-dimensional structures are becoming increasingly available.

## INTRODUCTION

Ultrafast polarized fluorescence and pump-probe spectroscopy can be used to obtain dynamic information about electronic excitation transport (EET), electron transfer, and conformational changes in proteins. Examples of studies in the photosynthetic area include EET pump-probe experiments in the Chl *a/b* LHC antenna complex from photosystem II [10] and in the BChl *a*-protein antenna complex from *Prosthecochloris aestuarii* [2,3], and a polarized fluorescence study of chlorosomes from *Chloroflexus aurantiacus* [9]. It is widely recognized that such time-resolved transient absorption and emission profiles carry detailed information about the excitation decay in the probed chromophores (e.g. due to trapping of excitation at photosynthetic reaction centers) and the dynamics of EET between chromophores. They also bear important evidence concerning the transition moment orientations and the coherent (i.e. excitonic) nature of the probed excited states.

Extracting such interpretations from time-dependent linear dichroism experiments requires quantitative understanding of the relationship between the polarized time-dependent observables (fluorescence and optical density transients) and the chromoprotein's structural and dynamic properties. Fundamental differences arise here between the linear dichroism of photobiological systems and that of randomly oriented molecules in solution or of molecules adsorbed on surfaces. The residual polarization observed at long times always vanishes for molecules in solutions in which the EET time scale is fast compared to the excited state lifetime, as was exemplified in the fluorescence depolarization study of Gochanour and Fayer

---

[11]. It is usually nonzero in solutions of chromoproteins, in consequence of their nonrandom chromophore architecture [2,3]. The initial polarization  $r(0)$ , always equal to 0.4, corresponding to an initial ratio of 3:1 for parallel to perpendicular signals, in the absence of intrinsic depolarization in dye solutions is frequently observed to be considerably less than 0.4 in photosynthetic systems [9,10]

In this paper, we outline the theory for linear dichroism decay in chromoproteins in solution and in oriented monolayers. The general forms of the polarized time-dependent profiles are derived, and the features that are specific to chromoproteins are highlighted. Examples of cases studied experimentally are presented from our pump-probe spectroscopy of photosystem I [3] and green photosynthetic bacteria.



## RESULTS AND DISCUSSION

### Dynamic Linear Dichroism of Chromoproteins in Solution

Our simplest prototype system exhibiting time dependent linear dichroism is a homogeneous solution of a protein containing two identical chromophores A and B with contrasting orientations, Figure 1. We assume that chromophore A is electronically excited by a laser pulse at time  $t=0$ , and that the excited state populations of chromophores A and B are given by  $P(t)s(t)$  and  $P(t)[1-s(t)]$ , respectively. Here  $P(t)$  is the isotropic decay function that reflects the total excited state population decay for both chromophores combined. The normalized function  $s(t)$  describes the redistribution of electronic excitation between chromophores A and B due to EET. The chromophores have well-defined orientations in the protein-fixed coordinate system; without loss of generality, we define the protein-fixed direction cosines for the transition moments of chromophores A and B as  $(0,0,1)$  and  $(\alpha,\beta,\gamma)$  respectively. The proteins are randomly oriented, and exhibit negligible rotational diffusion (owing to their large molecular weight) during the chromophore excitation lifetime. The solution is excited with a short laser pulse that is linearly polarized along the x-direction in the laboratory coordinate system. The linear dichroism is subsequently probed by measuring either the fluorescence intensity or the optical density polarized along the laboratory-fixed x- and y-axes. The resulting parallel and perpendicular profiles are then given by

$$I_{\parallel} = P(t) [\mu_{Ax}^4 s(t) + \mu_{Ax}^2 \mu_{Bx}^2 [1-s(t)]] \quad (1a)$$

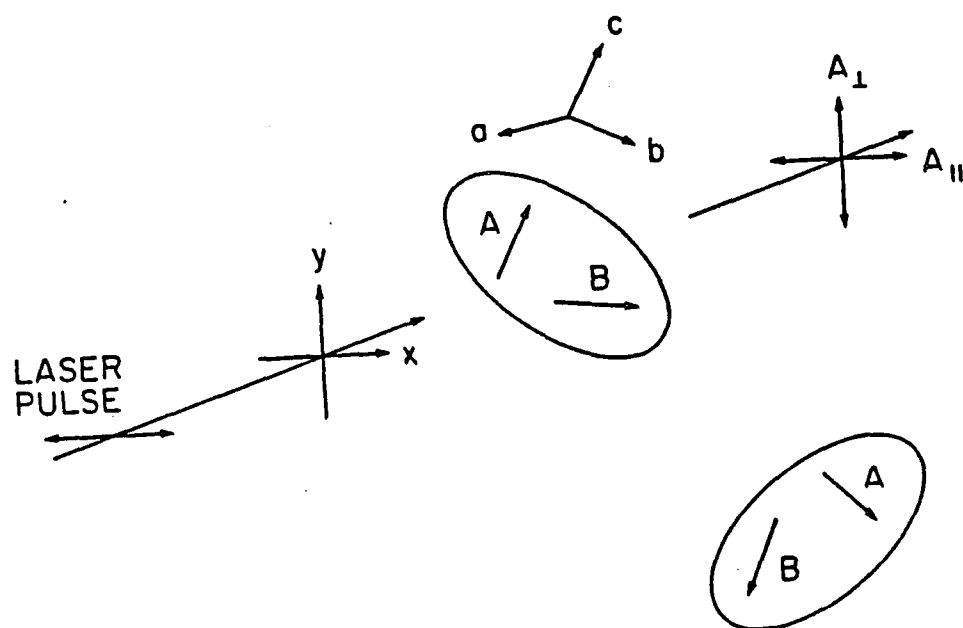


**Figure 1.** Linear dichroism model for isotropic solution of a chromoprotein containing two chromophores A and B. The protein-fixed transition moment directions are given by (0,0,1) and (a,b,c) respectively; the excitation laser pulse is polarized along the laboratory-fixed x-direction

$$I_{\perp} = P(t) [\mu_{Ax}^2 \mu_{Ay}^2 S(t) + \mu_{Ax}^2 \mu_{By}^2 [1 - S(t)]] \quad (1b)$$

where  $\mu_{Ax}$  is the x-component of chromophore A's transition moment, etc. We have ignored the fact that in polarized fluorescence experiments, the fluorescence transition moment of chromophore A may not be parallel to its absorption moment. We discuss this complication (called intrinsic depolarization or monomer anisotropy [17]) at the end of this section. For a protein molecule whose orientation in the solution is described by the Euler angles  $(\phi, \theta, \chi)$ , such laboratory-fixed transition moment components are related by a 3-dimensional rotation matrix [16] to the protein-fixed transition moment components  $\mu_{A\alpha}$ ,  $\mu_{A\beta}$ ,  $\mu_{A\gamma}$  of chromophore A through

$$\begin{pmatrix} \mu_{Ax} \\ \mu_{Ay} \\ \mu_{Az} \end{pmatrix} = \begin{pmatrix} \lambda_{x\alpha} & \lambda_{x\beta} & \lambda_{x\gamma} \\ \lambda_{y\alpha} & \lambda_{y\beta} & \lambda_{y\gamma} \\ \lambda_{z\alpha} & \lambda_{z\beta} & \lambda_{z\gamma} \end{pmatrix} \begin{pmatrix} \mu_{A\alpha} \\ \mu_{A\beta} \\ \mu_{A\gamma} \end{pmatrix} \quad (2)$$

and similarly for chromophore B. Hence, Equations (1) for the polarized transients may be recast in terms of the protein-fixed transition moment components,

$$\mu_{Ax}^4 = |\mu_A|^4 \lambda_{x\gamma}^4 \quad (3a)$$

$$\begin{aligned} \mu_{Ax}^2 \mu_{Bx}^2 = & |\mu_A|^4 [\lambda_{x\gamma}^4 \gamma^2 + \lambda_{x\gamma}^2 \lambda_{x\alpha}^2 \alpha^2 + \lambda_{x\gamma}^2 \lambda_{x\beta}^2 \beta^2 \\ & + 2 \lambda_{x\gamma}^2 (\lambda_{x\beta} \lambda_{x\gamma} \beta \gamma + \lambda_{x\alpha} \lambda_{x\gamma} \alpha \gamma + \lambda_{x\alpha} \lambda_{x\beta} \alpha \beta)] \end{aligned} \quad (3b)$$

$$\mu_{Ax}^2 \mu_{Ay}^2 = |\mu_A|^4 \lambda_{x\gamma}^2 \lambda_{y\gamma}^2 \quad (3c)$$

$$\begin{aligned} \mu_{Ax}^2 \mu_{By}^2 - |\mu_A|^4 [ \lambda_{x\gamma}^2 \lambda_{y\alpha}^2 \alpha^2 + \lambda_{x\gamma}^2 \lambda_{y\beta}^2 \beta^2 + \lambda_{x\gamma}^2 \lambda_{y\gamma}^2 \gamma^2 \\ + 2 \lambda_{x\gamma}^2 ( \lambda_{y\alpha} \lambda_{y\beta} \alpha \beta + \lambda_{y\beta} \lambda_{y\gamma} \beta \gamma + \lambda_{y\alpha} \lambda_{y\gamma} \alpha \gamma ) ] \end{aligned} \quad (3d)$$

where the pertinent rotation matrix elements are given by Marion [16] as

$$\lambda_{x\alpha} = \cos\phi \cos\chi - \sin\chi \cos\theta \sin\phi$$

$$\lambda_{x\beta} = \cos\chi \sin\phi + \sin\chi \cos\theta \cos\phi$$

$$\lambda_{x\gamma} = \sin\chi \sin\theta$$

$$\lambda_{y\alpha} = -\sin\chi \cos\phi - \cos\chi \cos\theta \sin\phi$$

$$\lambda_{y\beta} = -\sin\chi \sin\phi + \cos\chi \cos\theta \cos\phi$$

$$\lambda_{y\gamma} = \cos\chi \sin\theta$$

Equations (1) must be rotationally averaged in order to describe the observed polarized transients in an isotropic solution of chromoprotein. Using the identities

$$\langle \lambda_{x\gamma}^4 \rangle = \frac{1}{5} \quad (4a)$$

$$\langle \lambda_{x\gamma}^2 \lambda_{x\alpha}^2 \rangle = \langle \lambda_{x\gamma}^2 \lambda_{x\beta}^2 \rangle = \langle \lambda_{x\gamma}^2 \lambda_{y\gamma}^2 \rangle = \frac{1}{15} \quad (4b)$$

$$\langle \lambda_{x\gamma}^2 \lambda_{y\alpha} \lambda_{y\beta} \rangle = \langle \lambda_{x\gamma}^2 \lambda_{y\gamma} \lambda_{y\alpha} \rangle = \langle \lambda_{x\gamma}^2 \lambda_{y\gamma} \lambda_{y\beta} \rangle = 0 \quad (4c)$$

$$\langle \lambda_{x\gamma}^2 \lambda_{y\alpha}^2 \rangle = \langle \lambda_{x\gamma}^2 \lambda_{y\beta}^2 \rangle = \frac{2}{15} \quad (4d)$$

$$\langle \lambda_{x\beta} \lambda_{xy}^3 \rangle - \langle \lambda_{x\alpha} \lambda_{xy}^3 \rangle - \langle \lambda_{x\alpha} \lambda_{x\beta} \lambda_{xy}^2 \rangle = 0 \quad (4e)$$

we obtain the expressions for the measurable polarized transients

$$I_{\parallel} = P(t) |\mu_A|^4 \left[ \frac{1}{5} s(t) + \left[ \frac{1}{5} \gamma^2 + \frac{1}{15} (\alpha^2 + \beta^2) \right] [1 - s(t)] \right] \quad (5a)$$

$$I_{\perp} = P(t) |\mu_A|^4 \left[ \frac{1}{15} s(t) + \left[ \frac{1}{15} \gamma^2 + \frac{2}{15} (\alpha^2 + \beta^2) \right] [1 - s(t)] \right] \quad (5b)$$

Since  $\alpha^2 + \beta^2 + \gamma^2 = 1$ , these equations are equivalent to

$$I_{\parallel} = P(t) |\mu_A|^4 [1 + 0.8 [(1-a)s(t) + a]] \quad (6a)$$

$$I_{\perp} = P(t) |\mu_A|^4 [1 - 0.4 [(1-a)s(t) + a]] \quad (6b)$$

where the residual anisotropy parameter  $a$  is given by

$$a = \frac{1}{2} (3\gamma^2 - 1) \quad (7)$$

Equations (6) are the most general form for the polarized transients for a chromoprotein in solution. They differ from those for a solution of randomly oriented, uncomplexed chromophores [11] only through the presence of the residual anisotropy parameter  $a$ , which is a consequence of the well-defined relative orientations of the donor and acceptor chromophores in the protein. Since the anisotropic decay function  $s(t)$  is normalized to unity at zero time, the initial ratio of parallel to perpendicular signals is always 3:1. This corresponds to the initial value  $r(0) = 0.4$  of the conventional anisotropy function, defined as

$$r(t) = \frac{I_{\parallel}(t) - I_{\perp}(t)}{I_{\parallel}(t) + 2I_{\perp}(t)} = 0.4 [(1-a)s(t) + a] \quad (8)$$

and it stems from the fact that the ratio  $\langle \mu_{Ax}^4 \rangle / \langle \mu_{Ax}^2 \mu_{Ay}^2 \rangle$  [cf. Equations (3) and (4)] equals 3 in a rotationally isotropic distribution of absorber chromophores A. The anisotropy function in Equation (8) is equivalent to the one derived by Kim et al. [13] for intramolecular EET between identical chromophores in 9,9' bifluorene in solution. According to Equation (7), the anisotropy parameter is given by the second-order Legendre polynomial in the angle between the initial and final transition moment orientations. When these are parallel, the anisotropy parameter becomes unity, with the result that no depolarization occurs [Equations (6)]. The long time behavior of  $r(t)$  depends on the asymptotic limit of the decay function  $s(t)$ . If the two chromophores experience identical protein environments, the excitation equilibrates between A and B so that  $s(\infty) = 1/2$ . In this case, the limiting ratio of parallel to perpendicular signals becomes  $I_{\parallel}(\infty)/I_{\perp}(\infty) = (1.4 + 0.4a)/(0.8 - 0.2a)$ , which is always greater than one for realizable values of the anisotropy parameter [Equation (7)]. Hence, complete depolarization cannot arise from EET between chromophores in identical environments. An example of this behaviour is given in Figure 2, which shows 675 nm polarized optical density transients obtained by Causgrove et al. [3] from the Chl *a* core antenna system in enriched photosystem I particles from spinach (a PSI-60 preparation described by Golbeck [12] with approximately 60 antenna chlorophylls per P700 reaction

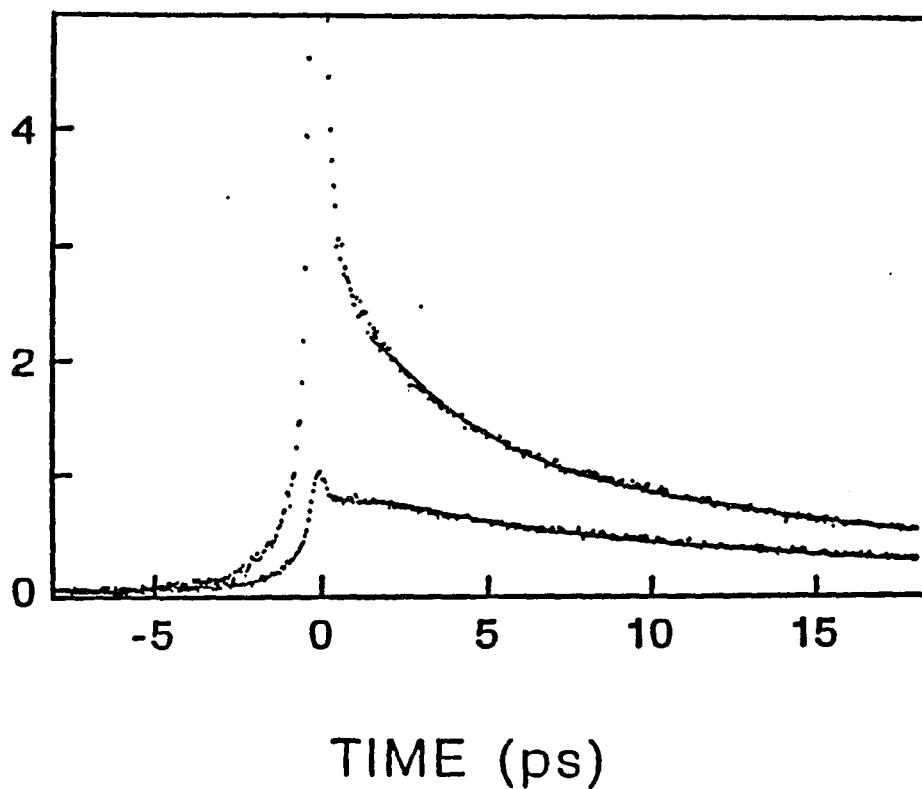


**Figure 2.** Anisotropic photobleaching transients for PSI-60 particles at 675 nm [3]. The upper (lower) transient is the parallel (perpendicular) signal. Continuous curves are convolutions of the laser autocorrelation functions with Equations. (6) using a single-exponential anisotropic decay function  $s(t) = \exp(-t/\tau)$ . The optimized parameters are  $a = 0.46$  and  $\tau = 2.9$  ps at 675 nm. In this figure and in Figure 3, the sharp spikes at zero time arise from the coherent coupling artifact [7]

center). The depolarization occurring during the first 10 ps is a manifestation of ultrafast EET in the PS I antenna. The observed early-time ratio of parallel to perpendicular transients is close to 3; the asymptotic ratio is 1.7, corresponding to an anisotropy parameter of 0.46 in consequence of the nonrandom chromophore architecture in the PSI-60 antenna.

We may also visualize a contrasting case in which chromophores A and B exhibit similar absorption coefficients at the probe wavelength (or similar fluorescence intensities at the monitored wavelengths), but are so situated that strongly downhill EET occurs,  $s(\infty) = 0$ . Complete depolarization ( $I_{\parallel}(\infty)/I_{\perp}(\infty) = 1$ ) than results when the angle between initial and final transition moments is  $54.7^{\circ}$  ( $a = 0$ ). An interesting feature of Equations (6) and (7) in this case is the possibility of inversion between  $I_{\parallel}$  and  $I_{\perp}$ , i.e.  $I_{\parallel}(\infty)/I_{\perp}(\infty) < 1$ . This does not occur for EET in solutions of randomly oriented molecules, or among monomers adsorbed on surfaces with random aximuthal angles about the surface normal; it can arise here owing to the fixed orientations of chromophores A and B in the protein. Such an occurrence requires  $\gamma^2 < 1/3$ , meaning that the donor and acceptor transition moments are nearly perpendicular. We are unaware of reported inversion behavior in any photosynthetic system.

Early-time ratios different from 3 cannot occur in isotropic solutions of protein-complexed chromophores. For example, if our model is trivially extended by assuming that the protein solution contains two different protein conformations with similar isotropic spectra (one in which the acceptor transition moment has a projection  $\gamma_1$  along the donor moment, the second in which the relevant projection is  $\gamma_2$ ), the form of the polarized transients is again given by Equations (6), with the anisotropy parameter



$$a = \frac{1}{2} \left( \frac{3(\gamma_1^2 + \gamma_2^2)}{2} - 1 \right) \quad (9)$$

and the hybrid anisotropic decay function

$$s(t) = \frac{(1 - \gamma_1^2) s_1(t) + (1 - \gamma_2^2) s_2(t)}{2 - \gamma_1^2 - \gamma_2^2} \quad (10)$$

where  $s_1(t)$  and  $s_2(t)$  are contrasting anisotropic decay functions in the two protein conformations. The assumption of spectral inhomogeneity similarly does not alter the basic form of Equations (6), nor do assumptions about the nature of the anisotropic decay functions  $s(t)$  (e.g. concerning the reversibility of EET between the donor and acceptor chromophores). Equations (6) are similarly valid (with appropriately defined anisotropy parameters and decay functions) for arbitrarily large assemblies of chromophores (e.g. in protein aggregates), regardless of the topology of their EET kinetic scheme. For example, the basic structural unit in the BChl *a*-protein complex of *P. aestuarii* was determined by Fenna et al. [8] to be a trimer of identical subunits, each containing 7 BChl *a* chromophores, whose positions are related through a C-3 axis. (This x-ray structure was later refined by Tronrud et al. [21]) In the simplest kinetic scheme for EET depolarization, an exciton state in subunit A is excited by a linearly polarized light pulse. The subsequent excitation populations in subunits A, B, and C in the trimer (aside from the isotropic decay  $P(t)$ ) was modeled by Causgrove et al. [2] via

$$-\frac{dA}{dt} = k(2A - B - C) \quad (11)$$

under the initial conditions  $A(0) = A_0$ ,  $B(0) = C(0) = 0$ . Here  $k$  is a phenomenological rate constant for EET between different subunits in the trimer. By symmetry, the transition moments in subunits A, B, and C are related by a  $120^\circ$  rotation about the trimer C-3 axis. Solution of the kinetic equation (11) yields the time-dependent excitation populations  $A(t) = A_0[1 + 2 \exp(-3kt)]/3$ ,  $B(t) = C(t) = A_0[1 - \exp(-3kt)]/3$ . Substitution of these expressions and the transition moments into Equations (1) then leads to expressions for the polarized transients that are identical in form to Equations (6), with

$$S(t) = e^{-3kt} \quad (12)$$

In this context, the parameter  $a$  is given by  $a = (3\gamma^2 - 1)^2/4$ , where  $\gamma$  is the projection of each subunit's transition moment along the C-3 axis, rather than by Equation (7). This example illustrates the sensitivity of the anisotropy parameter to the chromophore organization. Note that the phenomenological anisotropy decay function  $s(t)$  here is not the excited state population  $A(t)$  of the initially excited chromophore, and that its kinetics do not coincide with the single-step EET kinetics: in this case, it decays with a rate constant three times larger than the single-step rate constant  $k$ . Causgrove et al. [2,3] showed that extension of this kinetic model to *P. aestuarii* aggregates containing 7 or 27 trimers (by allowing EET between subunits in adjacent trimers) and solving the resulting kinetic equations numerically leads to

nonanalytic expressions for the anisotropic decay function  $s(t)$ . However, the physical significance of the  $\gamma$  parameter is unchanged, and the generic form of the polarized transients (6) is preserved.

Hence it is not meaningful to report, without clarification, polarized fluorescence or pump-probe profiles with initial ratios that are significantly less than 3. This can occur when the EET timescale is too rapid to observe under available time resolution; in this case, the ratio of parallel to perpendicular signals has already decayed to  $(1+0.8a) / (1-0.4a)$  at the earliest observable time, and remains constant thereafter according to Equations (6). Such profiles cannot be interpreted by claiming that the lack of depolarization during the measured time window arises because the donor and acceptor transition moments are parallel. Very recently, Lyle and Struve [15] observed photobleaching profiles in the 809 nm  $Q_y$  system of *P. aestuarii* that do not appear to conform to Equations 6, as shown in Figure 3. Here, there is substantial depolarization during the first several ps, but the initial polarization ratio is much lower than 3. These profiles were analyzed using a two-step depolarization model in which the laser-excited state A (with protein-fixed moment orientation  $(0,0,1)$ ) decays rapidly into an intermediate state B with orientation  $(\alpha_1, \beta_1, \gamma_1)$ , which then decays slowly into a third state C with contrasting orientation  $(\alpha_2, \beta_2, \gamma_2)$ . Such a rapid initial depolarization step can occur if the fluorescing or probed state is different than the laser-excited state (i.e. intrinsic depolarization, such as occurs when the  $Q_y$  state is monitored after excitation of the  $Q_x$  state). It may also arise from loss of exciton state coherence with attending localization of excitation on a single chromophore: the initial exciton state polarization (which is determined by the

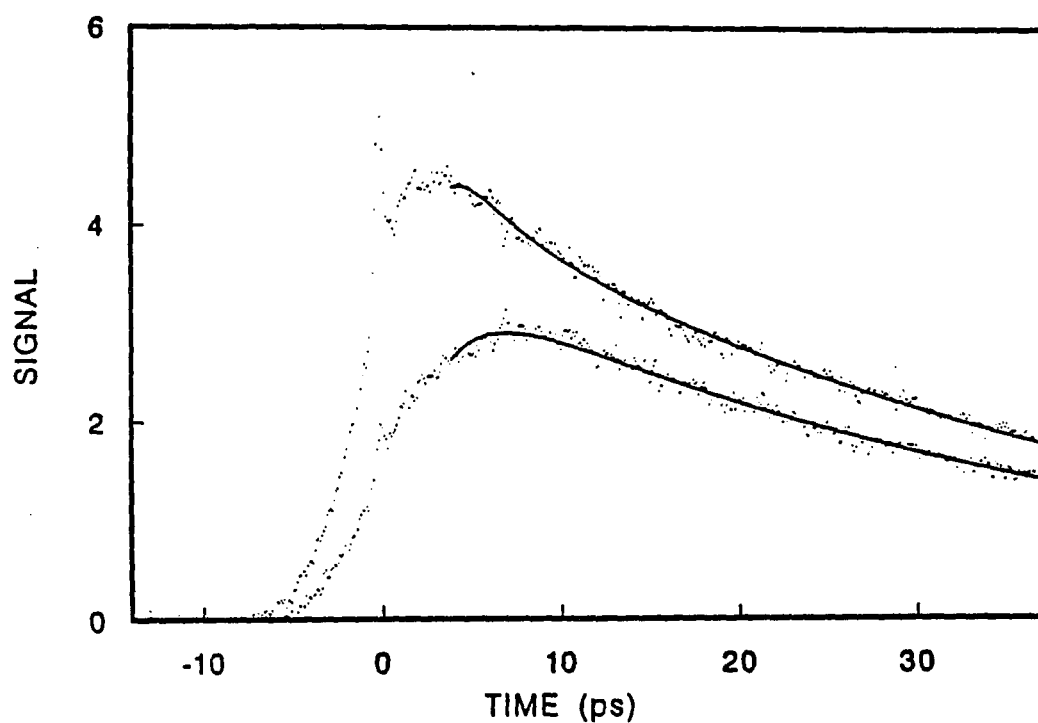


**Figure 3.** Anisotropic photobleaching transients for solution of BChl  $\alpha$ -protein from *Prosthecochloris aestuarii* at 814 nm [15]. Continuous curves are convolutions of the laser autocorrelation function with Eqs. (14) using a single-exponential decay function  $s(t) = \exp(-t/\tau)$ . The optimized parameters are  $a_1 = 0.95$ ,  $a_2 = 0.21$ ,  $\tau = 2.3$  ps

expansion coefficients of the single-chromophore states in the exciton state) is then rotated into the  $Q_y$  direction of the single chromophore that absorbs at the probed wavelength. Representing the  $B \rightarrow C$  state population decay with the function  $s(t)$ , we then have

$$I_{\parallel} = \langle \mu_{Ax}^2 \mu_{Bx}^2 \rangle s(t) + \langle \mu_{Ax}^2 \mu_{Cx}^2 \rangle [1 - s(t)] \quad (13a)$$

$$I_{\perp} = \langle \mu_{Ax}^2 \mu_{By}^2 \rangle s(t) + \langle \mu_{Ax}^2 \mu_{Cy}^2 \rangle [1 - s(t)] \quad (13b)$$

Using the appropriate values (4) for the rotationally averaged matrix elements (3) then leads to the expressions

$$I_{\parallel}(t) = |\mu_A|^2 |\mu_B|^2 P(t) [1 + 0.8 [(a_1 - a_2) s(t) + a_2]] \quad (14a)$$

$$I_{\perp}(t) = |\mu_A|^2 |\mu_B|^2 P(t) [1 - 0.4 [(a_1 - a_2) s(t) + a_2]] \quad (14b)$$

for the observable polarized transients with  $a_1 = (3\gamma_1^2 - 1)/2$  and similarly for  $a_2$ . Since the laser-excited state A has decayed to the intermediate state B at the earliest time monitored, the initial polarization ratio has already decayed from 3 to  $(1+0.8a_1)/(1-0.4a_1)$  in this model. Profiles for the BChl  $\alpha$ -protein at 805, 809, and 814 nm were fitted using Equation (14) with a single-exponential anisotropic decay function  $s(t)$  with lifetime  $\tau$ . These analyses converged to  $0.95 < a_1 < 1.05$  (corresponding to  $\gamma_1 \sim 1$ ), indicating that a two-step depolarization model is unnecessary in this antenna protein. The optimum ranges for the other two parameters were  $0.15 < a_2 < 0.35$  and  $2.3 \text{ ps} < \tau < 3.9 \text{ ps}$ . According to this analysis, the low polarization ratio observed at early times in Figure 3 occurs because the

initial picosecond decay in  $I_1(t)$  is rounded off by the comparatively broad laser autocorrelation function at this wavelength. Since low values are frequently observed for the initial anisotropy in polarized fluorescence and pump-probe experiments, profile analyses based on a two-step depolarization model may help to refine upper limits on the time scales for decay of the laser-prepared state in chromoproteins. The coherent coupling artifact, which frequently obscures early time kinetics in single-wavelength pump-probe experiments (cf. Figures 2 and 3), can be removed using the antisymmetrization technique described by Engh et al. [7].

This two-step depolarization model can also be used to describe the "monomer anisotropy" in fluorescence experiments. In this context, the initial fast depolarization step corresponds to rotation of polarization between the absorption and fluorescence transition moments on chromophore A. Where the anisotropy function  $r(t)$  is given by Equation (8) in the absence of such intrinsic depolarization, it now becomes

$$\begin{aligned} r(t) &= 0.4 [(a_1 - a_2) s(t) + a_2] \\ &= (r_0 - r_\infty) s(t) + r_\infty \end{aligned} \tag{15}$$

In the notation used by Moog et al. [17] to describe their fluorescence depolarization arising from EET in a synthetic chlorophyllide-substituted hemoglobin, the monomer anisotropy  $r_0$  is given by  $r(0) = 0.4a_1$ . Since  $a_1 = (3\gamma_1^2 - 1)/2 \leq 1$ , the monomer anisotropy ( $\sim 0.374$  in the chlorophyllide hemoglobin) is exceeded by 0.4 to an extent that depends on the angle between absorption and transition moments.

### Dynamic Linear Dichroism in Oriented Monolayers

Chromoproteins in photosynthetic membranes frequently exhibit preferred orientations with respect to the membrane plane (see, for example, Swarhoff et al. [18] and Tapie et al. [20]). In addition, proposals for constructing artificial antennae commonly involve embedding chromophores in Langmuir-Blodgett monolayers (Yamazaki et al., [22]). Hence, we treat the depolarization in a two-dimensional monolayer of chromoproteins as shown in Figure 4. Here, the depolarization accompanies EET between an initially excited chromophore A and a spectrally similar chromophore B. The respective transition moment orientations are described without loss of generality using the protein-fixed coordinates  $(\alpha_1, 0, \gamma_1)$  and  $(\alpha_2, \beta_2, \gamma_2)$ . Each of the proteins is oriented with its c-coordinate perpendicular to the monolayer (or membrane) plane; their azimuthal angles of rotation  $\phi$  about the c-axis are random. An incident laser pulse is x-polarized in the monolayer plane, and the fluorescence or probe beam is detected for light propagating normal to the plane with either x- or y-polarization. Since the protein-fixed c-axis is parallel to the laboratory-fixed z-axis in this geometry, the laboratory-fixed transition moment components for chromophore A are given by

$$\begin{pmatrix} \mu_{Ax} \\ \mu_{Ay} \\ \mu_{Az} \end{pmatrix} = \begin{pmatrix} \cos\phi & \sin\phi & 0 \\ -\sin\phi & \cos\phi & 0 \\ 0 & 0 & 1 \end{pmatrix} \begin{pmatrix} \alpha_1 \\ 0 \\ \gamma_1 \end{pmatrix} \quad (16)$$

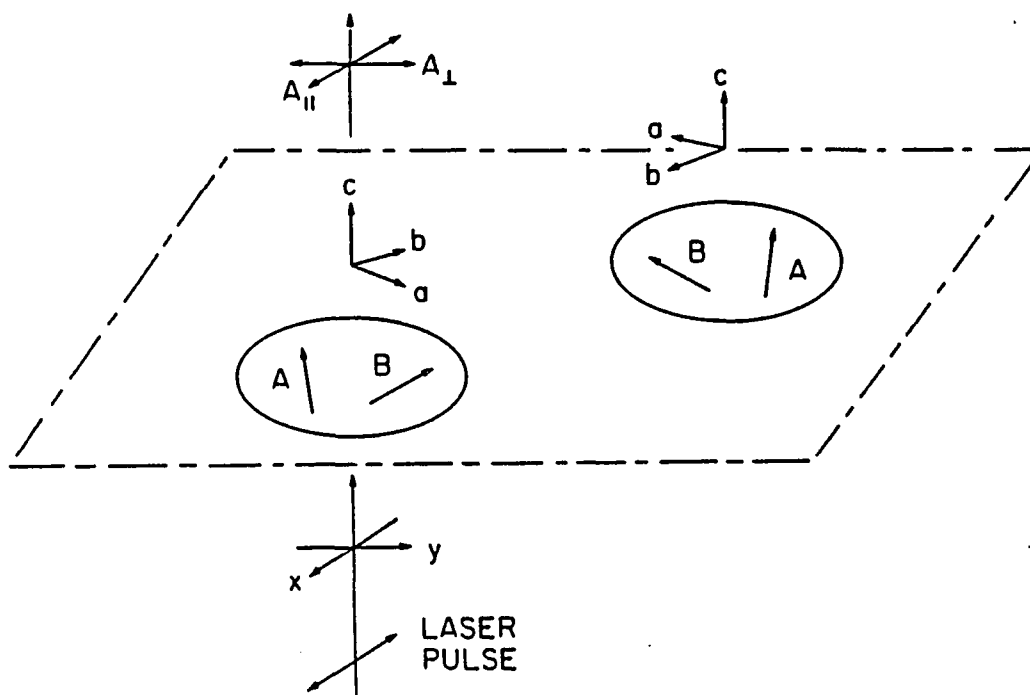


**Figure 4.** Linear dichroism model for an oriented chromoprotein in a membrane or Langmuir-Blodgett film. Proteins are aligned with their c-axes perpendicular to the surface plane, but have random azimuthal angles about the surface normal. Chromoproteins A and B have protein-fixed transition moment orientations  $(a_1, 0, c_1)$  and  $(a_2, b_2, c_2)$  respectively. The excitation laser pulse is polarized along the laboratory-fixed x-axis



and similarly for chromophore B. Rotational averaging of Equations (1) over the single angle  $\phi$  then leads to the polarized transients

$$I_{\parallel}(t) = |\mu_A|^4 P(t) [(1+\Gamma) + s(t) [3\Delta - \Gamma - 1]] \quad (17a)$$

$$I_{\perp}(t) = |\mu_A|^4 P(t) [(1-\Gamma) + s(t) [\Delta + \Gamma - 1]] \quad (17b)$$

where we define the orientation-dependent numbers

$$\Gamma = \frac{\alpha_2^2 - \beta_2^2}{2(\alpha_2^2 + \beta_2^2)} \quad (18)$$

$$\Delta = \frac{\alpha_1^2}{2(\alpha_2^2 + \beta_2^2)} \quad (19)$$

As in the case of 3-dimensionally random chromoprotein solutions, the initial polarization ratio is always 3:1; the parameter  $\Gamma$  in Equation (18) is analogous to the residual anisotropy parameter  $a$  in Equations (6). In the special case where  $\gamma_1 = \gamma_2 = \gamma$  (i.e. the transition moments in both chromophores have the same projection along the interface normal), we obtain the simpler expressions

$$I_{\parallel}(t) = |\mu_A|^4 P(t) [1 + 0.5 [(1-a)s(t) + a]] \quad (20a)$$

$$I_{\perp}(t) = |\mu_A|^4 P(t) [1 - 0.5 [(1-a)s(t) + a]] \quad (20b)$$

which is equivalent to the expressions derived by Craver [6,7] to describe EET depolarization for monomer chromophores adsorbed with their transition moments at a uniform angle from the surface normal. In this case the anisotropy function is given by

$$r(t) = \frac{I_{\parallel}(t) - I_{\perp}(t)}{I_{\parallel}(t) + I_{\perp}(t)} = 0.5 [(1-a)s(t) + a] \quad (21)$$

It is widely appreciated [14] that isolation of the isotropic excited state population decay  $P(t)$  requires observation of the fluorescence or pump-probe signal with the analyzing polarizer aligned at the magic angle  $\omega$  such that the anisotropic terms proportional to  $s(t)$  in the transmitted signal

$$I_{\parallel} \cos^2 \omega + I_{\perp} \sin^2 \omega$$

cancel. For the 3-dimensionally isotropic solutions described by Equations (6), the magic angle is  $\omega = 54.7^\circ$  [19]. For EET among chromophore monomers adsorbed at a uniform angle from the surface normal (Equations (19)),  $\omega$  becomes  $45^\circ$  [1]. For the more general case of chromoproteins in oriented monolayers, the magic angle depends on the protein-fixed chromophore orientations via

$$\tan^2 \omega = \frac{3\Delta - \Gamma - 1}{1 - \Delta - \Gamma} \quad (22)$$

and the anisotropy function is

$$\begin{aligned}
 r(t) &= \frac{I_{\parallel}(t) - I_{\perp}(t)}{I_{\parallel}(t) \cos^2 \omega + I_{\perp}(t) \sin^2 \omega} \\
 &= \frac{2}{1 + \Gamma \cos 2\omega} [(\Delta - \Gamma) s(t) + \Gamma]
 \end{aligned}
 \tag{23}$$

In contrast to the case of protein solutions described by Equations (6), the factors weighting the isotropic and anisotropic parts of the polarized transients in Equations (17) contain information about the protein-fixed transition moment orientations through Equations (18) and (19). Hence, the fact that the transition moments are averaged about only one axis (the surface normal) means that experiments on oriented monolayers can cast the chromophore organization into considerably sharper relief than solution studies. [In the latter case, the anisotropic profiles depend only on the projection  $\gamma$  of the acceptor transition moment along a particular axis, viz. Equations (6) and (7).] When the 3-dimensional structure of the chromoprotein is known (e.g. for BChl *a*-protein from *P. aestuarii* [21], such experiments can then facilitate the assignment of bands to chromophores or exciton components in the chromoprotein absorption spectrum. As the orientations of photosynthetic particles in oriented monolayers are often similar to their orientations with respect to thylakoid membranes [18], the preferred directionalities of EET can be ascertained in principle for naturally occurring systems.

## Note Added in Proof

The arbitrary assumption that chromophore A (and not B) is selectively excited in the chromoprotein does not affect the expressions derived for the protein solutions in the first section of the Results and Discussion. However, allowing both chromophores to be excited at zero time in the oriented monolayers in the last section of the Results and Discussion results in replacing the quantity  $\Delta$  defined in equation 19 with

$$\Delta = \frac{\alpha_1^4 + (\alpha_2^2 + \beta_2^2)^2}{4\alpha_1^2(\alpha_2^2 + \beta_2^2)}$$

We thank Dr. Herbert van Amerongen for bringing this point to our attention.

## ACKNOWLEDGMENTS

The Ames Laboratory is operated for the U. S. Department of Energy by Iowa State University under Contract No. W-7405-Eng-82. This work was supported by the Office of Basic Energy Sciences. We are indebted to W. E. Catron for supporting one of us (P. A. L.) through a research fellowship.

## REFERENCES

1. Anfinrud, P. A.; Hart D. E.; Struve W. S. *J. Phys. Chem.* 1988, 92, 4067
2. Causgrove, T. P.; Yang S.; Struve W. S. *J. Phys. Chem.* 1988, 92, 6790
3. Causgrove, T. P.; Yang S.; Struve W. S. *J. Phys. Chem.* 1988, 92, 6121
4. Chuang, T. J.; Eisinger L. B. *J. Chem. Phys.* 1972, 57, 5094
5. Craver, F. W.; Knox R. S. *Mol. Phys.* 1971, 22, 385
6. Craver, F. W. *Mol. Phys.* 1971, 22, 403
7. Engh, R. A.; Petrich J. W.; G. R. Fleming *J. Phys. Chem.* 1985, 89, 618
8. Fenna, R. E.; Ten Eyck L. F.; Matthews B. W. *Biochem. Biophys. Res. Commun.* 1977, 75, 751
9. Fetisova, Z. G.; Freiberg A. M.; Timpmann K. E. *Nature* 1988, 334, 633
10. Gillbro, T.; Sundström V.; Sandström, Å.; Spangfort M.; Andersson B. 1985 *FEBS Letts.* 193, 267
11. Gochanour, C. R.; Fayer M. D. *J. Phys. Chem.* 1981, 85, 1989
12. Golbeck, J. H. *Methods Enzymol.* 1980, 69, 129
13. Kim, Y. R.; Share, P.; Pereira M.; Sarisky M.; Hochstrasser R. M. *Chem. Phys.* 1989, 91, 7557
14. Lakowicz, J. R. *Principles of fluorescence spectroscopy*; Plenum Press: New York, 1983, p. 131
15. Lyle, P. A.; Struve W. S. *J. Phys. Chem.*, 1990
16. Marion, J. B. *Classical dynamics of particles and systems*; Academic Press: New York, p. 391
17. Moog, R. S.; Kuki, A.; Fayer M. D.; Boxer S. G. *Biochem.* 1984, 23, 1564

18. Swarthoff, T.; de Grooth, B. G.; Meiburg R. F.; Rijgersberg C. P.; Ames J. *Biochim. Biophys. Acta* 1980, 593, 51
19. Tao, T. *Biopolymers* 1969, 8, 609
20. Tapie, P.; Choquet, Y.; Breton, J.; Delepelaire, P.; Wollman, F. -A. *Biochim. Biophys. Acta* 1984, 767, 57
21. Tronrud, D. E.; Schmid, M. F.; Matthews, B. W. *J. Mol. Biol.* 1986, 188, 443
22. Yamazaki, I.; Tamai, N.; Yamazaki, T.; Murakami, A.; Mimuro, M.; Fujita Y. *J. Phys. Chem.* 1988, 92, 5035

## SECTION CONCLUSIONS

A possible EET scenario has been proposed for *P. aestuarii*. Paper I proposes that relaxation between exciton components occurs in approximately 100 fs at 4.2 K and faster at room temperature. Measurements of EET hopping to subunits adjacent to the one in which the excitation localizes takes between 2 and 4 ps. Thermalization and localization is shown to be complete by 2 ps.

Paper II derived general forms of the polarized time dependent profiles for two cases: chromoproteins in solution and in oriented monolayers. The results were compared to experimental results obtained with PSI and *P. aestuarii*. The results show that the initial parallel to perpendicular ratio is always 3:1 regardless of the system even when generalized to two different protein environments, spectral inhomogeneity or different anisotropic decay functions. Complete depolarization can not arise from EET between chromophores in identical environments. An example of this is EET in Chla core antenna system with 60 chls/P700 when the parallel to perpendicular ratio is 1.7 at long times.

Results obtained from paper II also show that unlike for proteins in solution, the isotropic and anisotropic parts of the polarized transients for oriented proteins gives information relating to the protein fixed transition moments. Thus for known 3-dimensional protein structures such as is the case for *P. aestuarii*, such experiments could facilitate assignments of bands to chromophores or exciton components in the absorption spectra.



## SECTION REFERENCES

1. Gregory, R. P. F. in *Photosynthesis*; Chapman and Hall: New York, 1989, Chpt. 2
2. Holt, S. C.; Conti, S. F.; Fuller, R. C. *J. Bacteriol.* 1966, 91, 311
3. Staehlin, L. A.; Golicki, J. R.; Drews, G. *Biochem. Biophys. Acta* 1980, 589, 30
4. Matthews, B. W.; Fenna, R. E. *Acc. Chem. Res.* 1980, 13, 309
5. Tronrud, D. E.; Schmid, M. F.; Matthews, B. W. *J. Mol. Biol.* 1986, 188, 443
6. Daurot-Larroque, S. T.; Brew, K.; Fenna, R. E. *J. Biol. Chem.* 1986, 261, 360
7. Olson, J. M.; Romano, C. A.; *Biochim. Biophys. Acta* 1962, 59, 726
8. Olsen, J. M.; Koenig, D. F.; Ledbetter, M. C. *Arch. Biochem. Biophys.* 1969, 129, 42
9. Olson, J. M.; In *Methods of Enzymology*, Vol. 23, Part A; San Pietro, A., Ed.; Academic Press: New York, 1971; p. 636
10. Davydov, A. S. *Theory of Molecular Excitons*; Plenum Press: New York, 1971
11. Whitten, W. B.; Nairn, J. A.; Pearlstein, R. M. *Biochim. Biophys. Acta* 1978, 503, 251
12. Whitten, W. B.; Olson, J. M.; Pearlstein, R. M. *Biochim. Biophys. Acta* 1980, 591, 203
13. Philipson, K. D.; Sauer, K. *Biochemistry* 1972, 11, 1880
14. Olson, J. M.; Ke, B.; Thompson, K. H. *Biochim. Biophys. Acta* 1976, 430, 524
15. Pearlstein, R. M.; Hemenger, R. P. *Proc. Natl. Acad. Sci. USA* 1978, 75, 4920
16. Pearlstein, R. M. In *Photosynthetic Light-Harvesting Systems*; Scheer, H., Ed.; Walter de Gruyter: Berlin, 1988, p. 555
17. Pearlstein, R. M. In *Chlorophylls*; Scheer, H., Ed.; CRC Press: Boca Raton, 1991, p. 1047

18. Lutz, M.; Hoff, A. J.; Brehamet, L. *Biochim. Biophys. Acta* 1982, 679, 331
19. Pearlstein, R. M. *Photosyn. Res.* 1992, 31, 213
20. Pearlstein, R. M. In *Photosynthesis: Energy Conversion by Plants and Bacteria* Vol. 1; Govindjee, Ed.; Academic Press: New York, 1982, p. 293
21. Johnson, S. G.; Small, G. J. *J. Phys. Chem.* 1991, 95, 47

SECTION II.

PUMP-PROBE AND HOLE BURNING SPECTROSCOPY  
OF PHOTOSYSTEM I PARTICLES

## INTRODUCTION

### Review of PSI

In green plants photosystem I (PSI) and PSII occur in different parts of the thylakoid (see General Introduction). In general, PSII occurs in the granum and PSI occurs in unstacked regions of thylakoid [1]. Because of their differing locations PSI and PSII can be separated with mechanical methods [2]. To obtain different proteins of the PSI complex for study, detergents of increasing strength must be used to isolate smaller protein subsets of the overall structure. Golbeck has defined several terms in order to characterize the different preparations in the literature [3,4]. Figure 1 shows a schematic of the naming system. The native PSI (holocomplex) consists of the PSI core complex and light harvesting complex I (LHCI) polypeptides as well as the intact reaction center (RC) which contains P700 and its associated electron acceptors  $A_0$ ,  $A_1$ ,  $F_x$ ,  $F_A$ , and  $F_B$ . P700 is most likely a dimer of chlorophyll *a*,  $A_0$  a chlorophyll *a* monomer,  $A_1$  a phylloquinone (vitamin K), and  $F_x$ ,  $F_A$ , and  $F_B$  are all [4Fe-4S] iron-sulfur clusters. The PSI core complex can be obtained with the use of nonionic detergents which strip away the LHCI polypeptides from the native complex, but leaves the RC intact. The PSI core protein is obtained by treating the core complex with chaotropic agents to strip the  $F_A/F_B$  polypeptides and other peripheral, low molecular mass polypeptides from the core complex. If sodium dodecyl sulfate is used to strip away all peripheral low molecular mass polypeptides and destroy  $F_x$  leaving behind only P700 and  $A_0$ , then CP1 (P700-Chl *a* core protein) is obtained. Optical spectra of the  $Q_y$  region of the PSI

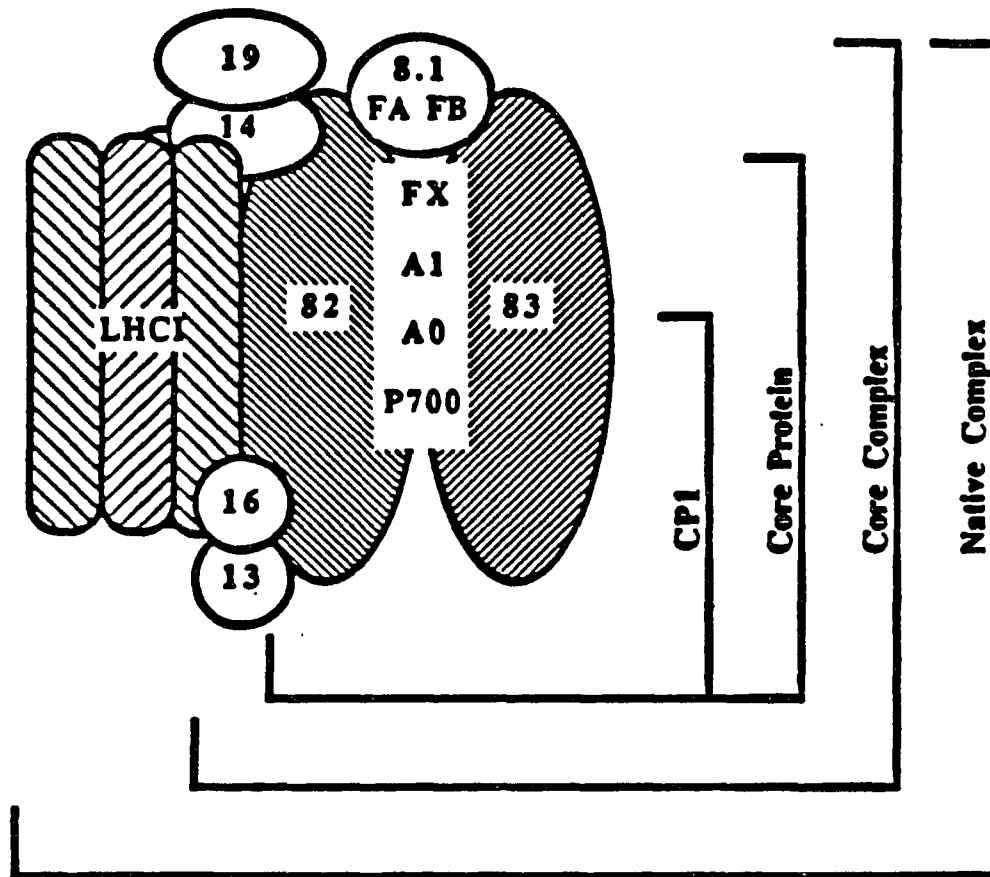


**Figure 1.** Naming system for the Photosystem I protein complex showing the polypeptide composition of the isolatable particles (reprinted from reference 3)

native complex as well as several smaller (in regards to the Chl/P700 ratio) particles show little structure at room temperature and sharpens only slightly upon cooling to cryogenic temperatures. Since the majority of the absorption is due to the antenna chlorophyll molecules, specific site energies can not be assigned to a particular chlorophyll arrangement. However, by use of fluorescence and derivative spectroscopy, several bands have been reported [5,6,7]. The finding of an inhomogeneous distribution of chlorophyll energies in the antenna is consistent with the role of the antenna to absorb as much of the solar spectrum as possible. The protein acts to change the energies of the chlorophyll molecules to achieve this goal by surrounding the chlorophylls with slightly different environments [8].

Unlike *P. aestuarii* [9], the light-harvesting Chl *a/b*-protein complex of PSII [10], and the light-harvesting C-phyocyanin biliprotein from the blue green alga *Mastigocladus laminosus* [11], whose three dimensional structures are known, little is known about the PSI antenna structure. Much experimental evidence has been obtained, though, which indicates that the antenna is organized in a manner to help achieve efficient energy transfer to the RC. Causgrove et al. using polarized pump probe spectroscopy found nonvanishing residual anisotropies which indicates that local ordering exists in PSI antenna systems [12,13]. Also, based on the lifetimes they observed (which were one order of magnitude slower than the single step hopping time calculated by Owens et al. using fluorescence techniques and a regular lattice model [14]) Causgrove et al. suggested that the antenna chlorophylls are grouped into subunits. Further, in accordance with Sauer's pebble mosaic model [15], after rapid delocalization of the energy within a subunit, the lifetimes they

were detecting were proposed to be due to migration of the energy between subunits. Owens et al. further showed that for varying antenna sizes the fluorescence decay times did not change and the emitting chlorophylls were not limited to long wavelength forms. Their data supports the subunit model and argues against a funnel model where excitation is guided to the reaction center from short to long wavelength chlorophylls.

In a recent study by Fleming and coworkers [16,17] modeling of temperature dependent fluorescence decay times revealed the need for long wavelength chlorophylls in close proximity to the RC in order to simulate the experimental data. They simulated the data by using a regular lattice model consisting of 49 sites for antenna molecules and 1 site for the RC. Förster energy transfer theory was used to obtain the transfer times by first calculating the temperature dependent absorption spectra for each antenna pigment and then calculating the overlaps of the donor fluorescence and acceptors absorption spectrum. The absorption spectrum for each pigment was generated quantum mechanically using 40 vibrational modes and their Franck-Condon factors as given in the hole burning experiments of Gillie and Small [18]. The following equation was used to calculate the absorption spectra:

$$I(\omega) = \frac{\mu_{01}^2}{2\pi} \int_{-\infty}^{\infty} dt e^{-i\omega t} \langle e^{i\omega H_1 t} e^{-iH_0 t} \rangle e^{-\Gamma t} e^{-\gamma t^2} \quad (1)$$

where  $\mu_{01}$  is the transition dipole matrix element,  $H$  the hamiltonians for the system,  $\Gamma$  the width of each vibronic transition, and  $\gamma$  the inhomogeneous broadening. Though it is not clear from their work, the temperature dependence was incorporated into the equation through the bracketed term in equation 1. Page and Chan [19] give an expression for the bracketed term in what is known as the time correlator method. It turns out that the term is essentially equation 13 derived in the following section. Fleming and coworkers' method differs from the one to be presented in the next section in the way the vibrations are included into the rate calculation. They incorporate all modes required to obtain the absorption spectra and used multiphonon theory to generate the temperature dependence before using Förster theory to obtain the rates. In the following theory the rate is calculated directly from multiphonon theory, but only a few modes (supposedly only those that are active in the energy transfer process) are incorporated into the calculations. A second difference is that in Fleming and coworkers' calculations experimental Franck-Condon factors are used, whereas in the multiphonon theory the coupling parameters are obtained and then compared to those obtained from hole burning experiments. Finally, with the transfer times calculated they use a master equation approach [20] to generate the energy transfer rates for several different proposed structural models of the antenna system and compared them to the experimental values. One of their findings was that a funnel model is not consistent with their experimental decay times with or without the inclusion of low energy pigments near to the RC. With a randomly arranged inhomogeneous antenna model incorporating two long wavelength chlorophylls close to the RC, the data at all temperatures was well approximated.



The idea of low energy pigments existing near the RC was first proposed by van Grondelle [21,22]. He rationalized that enhancement of energy trapping at the RC should be facilitated by having a few low energy chlorophylls in close spatial proximity, because the time the excitation spends near the RC would increase and, therefore, the probability of trapping.

Besides indirect experimentation as to the structure of PSI antenna and RC complexes, X-ray diffraction studies and electron microscopy have been performed [23,24,25]. Crystals of varying sizes and quality (some diffracting to 4 Å) have now been grown in several groups [23,26,27]. Both monomer and trimer arrangements have been seen. Possibly within the next few years a detailed structure for the core complex of PSI will be available and as much will be known about PSI as for bacterial reaction centers.

Recent concerns over the integrity and stability of PSI preparations from green plants has led some researchers to concentrate on PSI from cyanobacteria [4,28]. PSI is well conserved in green plants, algae, and cyanobacteria [4] but preparations from cyanobacteria can be grown and extracted more easily than from green plants and are more stable. PSI from cyanobacteria differs from green plants in that LHCI is absent (see General Introduction). Thus, PSI from cyanobacteria is essentially the core complex described earlier with approximately 100 chl *a* for every RC.

In the past much has been said about the differences between PSI and the bacterial RC's. Now, however, it is becoming increasingly apparent that more similarities than differences exist [4]. Figure 2 shows the proposed structure of the PSI RC. Like in bacterial RC's and PSII, PSI binds all of the electron transport components into two polypeptides

---

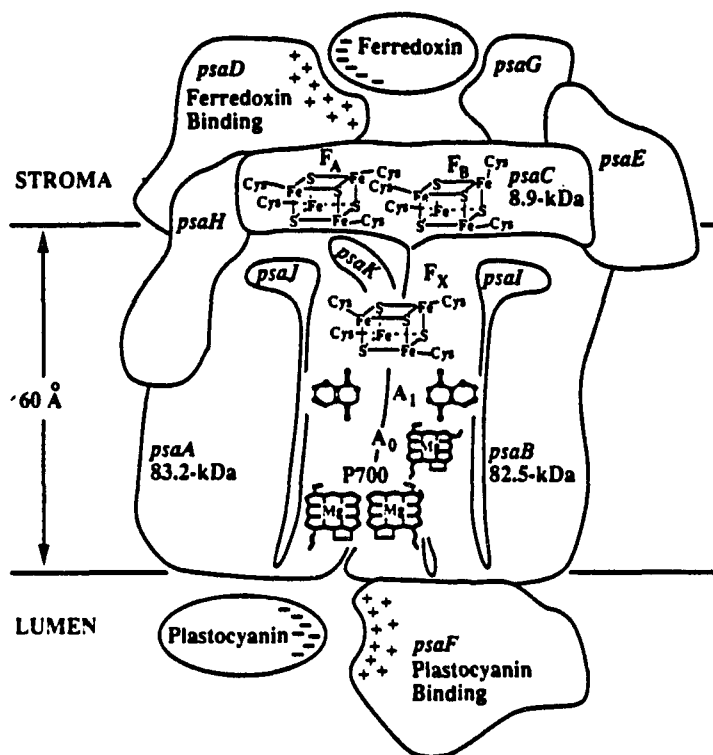


**Figure 2.** Proposed model of PSI complex generalized to show similarity of higher plants, algae, and cyanobacteria (reprinted from reference 4)

(named psA and psB). The components in all reaction centers include a special pair of a chlorophyll species, a chlorophyll or pheophytin electron acceptor, and two quinone species. Also, as in PSII and bacterial RC's the  $F_x$  iron sulfur complex may join the heterodimer along the pseudo- $C_2$  symmetry axis on the stromal surface of the thylakoid.

### Electron Transfer Theory

The rate of a transition from an initial state  $a$  to a final state  $b$  is written as (Fermi's Golden Rule [29]):

$$W = \frac{2\pi}{\hbar} |V|^2 (FC) \quad (2)$$

where  $\hbar$  is Plank's constant,  $V$  is the electronic Hamiltonian matrix element connecting states  $a$  and  $b$ , and  $FC$  is an expression relating the density of states  $b$  to the Franck-Condon condition. The condition is well represented by a vertical transition from curve  $V_R$  to curve  $V_P$  in Figure 3 because the Franck-Condon principle states that an electronic transition from a given initial state to a final state occurs on a time scale much faster than the motion of the nuclei. Figure 3 is shown under the harmonic condition and the wave functions (not shown) are those of the harmonic oscillator with the vibrational energy in state  $a$  and  $b$  written as  $E_n = (n+1/2)\hbar\omega$  [30].

Before treating the coupling of the vibrational states to a change in the electronic state quantum mechanically, it is useful to define the quantities shown in Figure 3 from a classical

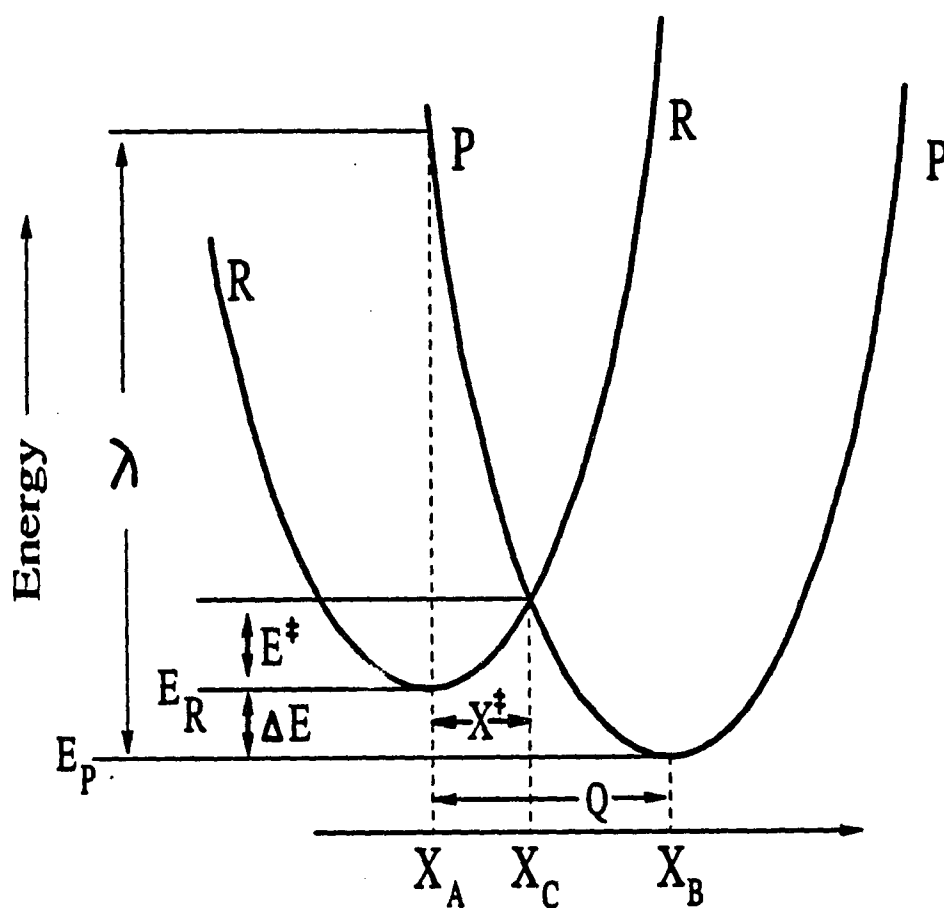


**Figure 3.** Diagram illustrating the Franck-Condon principle. The quantities used are defined in the text

description [31,32]. If curves  $V_R$  and  $V_P$  are parabolas of equal frequency, equations for the curves can be written:

$$V_R = \frac{k_H(X-X_A)^2}{2} + E_R \quad (3)$$

$$V_P = \frac{k_H(X-X_B)^2}{2} + E_P \quad (4)$$

where  $k_H$  equals the Hook's law force constant,  $V_R$  the nuclear potential energy of the Donor and  $V_P$  that of the acceptor, and the angular frequency  $\omega=(k_H/M)^{1/2}$  where  $M$  is the reduced mass of the oscillator.

The reorganization energy,  $\lambda$ , is the amount of energy required to displace the system an amount,  $Q=(X_B-X_A)$ , and is a measure of the coupling of the nuclear vibrations to the electronic transfer.  $\lambda$  is equal to  $V_P(X_A) - V_R(X_A) + \Delta E = (k_H/2)Q^2 = M\omega^2 Q^2/2$  (Recall from the General Introduction that  $S=\lambda/\hbar\omega$ ). The activation energy can be written in terms of either  $V_R$  or  $V_P$  as  $E^\ddagger = V_R(X_C) - E_R = V_P(X_C) - E_R$ . With  $X^\ddagger = X_C - X_A$  the activation energy is  $k_H(X^\ddagger)^2/2$  for  $V_R$  and for  $V_P$  is  $k_H(Q-X^\ddagger)^2/2 - \Delta E$ . By expanding the latter equation and substituting in the energy of activation expression for  $V_R$  and the expression for  $\lambda$ , collecting terms, and finally dividing through by  $4\lambda$  the following equation is derived:

$$E^\ddagger = \frac{(\lambda - \Delta E)^2}{4\lambda} \quad (5)$$

The activation energy can then be put into the form of an arrhenius equation ( $W \propto \exp(-E^\ddagger/kT)$ ). Marcus used a statistical mechanical treatment to obtain the proportionality constant (see equation 2 of the General Introduction). Concentrating on the exponential term a few points can be stressed. If  $\Delta E$  equals the reorganization energy then the maximum rate is obtained since the activation energy becomes zero and by equation 2 of the General Introduction the rate becomes weakly temperature dependent through  $T^{-1/2}$ . Also note that there are two separate regions of interest: the first for  $\Delta E < \lambda$  which is the normal region, the second is called the inverted region and occurs for  $\Delta E > \lambda$  [33].

At all temperatures where the lowest vibrational states have significant population, tunneling processes can have a large contribution to the rate. The probability of the tunneling is written as:

$$C^2(n, n') = \left[ \int \chi_n \chi_{n'} dx \right]^2 \quad (6)$$

where  $C(n, n')$  is the mathematical representation of the Franck-Condon principle. In equation (6)  $\chi_{n(n')}$  is the vibrational wave function for the state  $n(n')$ . Remembering that the wave functions of an harmonic oscillator do not go to zero at the boundaries, there will still be some probability below the crossing point of the two curves in Figure 3 (ie. tunneling can occur). Tunneling processes are not included in the arrhenius equation above. Two problems arise from this neglect. One is that at low temperatures the equation fails to approximate the experimental results as expected since tunneling processes dominate the rate. The second problem has to do with the inverted region. From equation (5) it can be seen that the rate

in the inverted region should mirror that in the normal region. However in the inverted region the overlapping wave functions can lead to large Franck-Condon factors and thus, increase the rate over what is predicted from the classical prediction. Many workers have attempted to find experimental confirmation of the inverted region [33]. The first evidence for the existence in real systems was found in a reaction studied by Beitz and Miller [34]. The first reliable observation of the inverted region came later in charge-shift reactions between the biphenyl radical anion and several acceptors in low temperature glasses and in an electron transfer reaction between the biphenyl radical anion to various acceptors separated by hydrocarbon linkages [35,36]. Since then several others have found experimental evidence for the inverted region [37,38,39].

From the previous discussion, a formula for the rate of transition from state  $a$  to  $b$  can be constructed. To get the rate of reaction, the overlap integrals between states  $a$  and  $b$  are multiplied by the number of systems in state  $a$  at some temperature  $T$ , and then summed over all  $n, n'$  and multiplied by the probability for electron tunneling to give:

$$W = A \sum_{n=0}^{\infty} \sum_{n'=0}^{\infty} C^2(n, n') B(n, T) \quad (7)$$

where

$$B(n, T) = e^{-\hbar\omega n/kT} (1 - e^{-\hbar\omega/kT}) \quad (8)$$

gives the fraction of oscillators in state  $n$  at temperature  $T$  and  $A = (2\pi V^2/\hbar^2\omega)$  is the part of the rate dependent on the electron tunneling probability. Comparing to equation (2) the FC is seen to equal:

$$FC = \sum_{n=0}^{\infty} \sum_{n'=0}^{\infty} C^2(n, n') B(n, T) / \hbar\omega \quad (9)$$

By substituting in for  $C^2(n, n')$  the FC can be written as :

$$FC = \sum_{n=0}^{\infty} \sum_{n'=0}^{\infty} \int \chi_n \chi_{n'} dx \int \chi_n \chi_{n'} dx \quad (10)$$

$$\times B(n, T) \delta(n - n' - p) / \hbar\omega$$

where the delta function is included to ensure energy conservation.

Further mathematical manipulations for FC in deriving the generating formalism are involved. For a complete description the reader is referred to Devault [31]. A very brief description of the steps required follows. The delta function can be written in integral form as:

$$\delta(n - n' - p) = \frac{\omega}{2\pi} \int e^{i(n - n' - p)\omega t} dt \quad (11)$$

Each summation can be handled by applying Mehler's formula (12). In Mehler's formula the functions  $H_n()$  are the Hermite polynomials of the wavefunctions  $\chi_{n(n)}$



$$\sum_{r=0}^{\infty} \frac{(Z/2)^r}{r!} H_r(\xi) H_r(\eta) = \frac{1}{(1-Z^2)^{1/2}} \exp\left[\frac{2\xi\eta Z - (\xi^2 + \eta^2)Z^2}{1-Z^2}\right] \quad (12)$$

At this point the integration is carried out through a change of variables and terms are collected through the use of several trigonometric definitions to finally obtain:

$$FC = \frac{1}{2\pi\hbar} \int dt \exp[-S(2\bar{n}+1) - \bar{n}e^{i\omega t} - \bar{n}e^{-i\omega t}] \times \exp[-pi\omega t] \quad (13)$$

where:

$$\bar{n} = [\exp(\hbar\omega/k_b T) - 1]^{-1} \quad (14)$$

and  $p = \Delta E/\hbar\omega$  and  $2\bar{n}+1 = \coth(\hbar\omega/2kT)$ .

The overall rate with the inclusion of multiple frequencies is:

$$W = \frac{2\pi}{\hbar} |V|^2 \frac{1}{2\pi\hbar} \int dt f(t) e^{-i\Delta Et/\hbar} \quad (15)$$

where:

$$f(t) = \exp[-G + G_+(t) + G_-(t)] \quad (16)$$

$$G_+(t) = \sum_k S_k (\bar{n}_k + 1) e^{i\omega_k t} \quad (17)$$

$$G_{-}(t) = \sum_k S_k(\bar{n}_k) e^{-i\omega_k t} \quad (18)$$

$$G = G_{+}(0) + G_{-}(0) = \sum_k (2\bar{n}_k + 1) \quad (19)$$

Devault then goes on to show how the  $\exp[G_{+}+G_{-}]$  can be written in the form of a Bessel function to give the formulas:

$$W = A e^{-G} \prod_k \sum_{m_k=-\infty}^{\infty} \left( \frac{\bar{n}_k + 1}{\bar{n}_k} \right)^{m_k/2} \times I_{m_k}(2S_k[\bar{n}_k(\bar{n}_k + 1)]^{1/2}) e^{m_k i\omega_k t} \quad (20)$$

Though mathematically convenient, this transformation does not give a physical picture of how the vibrations contribute to the rate. Therefore, a more physical derivation will be given as hinted by Jortner [40]. The generating function can be expanded in a Taylor series in the  $G_{+}$  and  $G_{-}$  terms giving:

$$\exp[G_{+} + G_{-}] = \sum_{R=0}^{\infty} \frac{[G_{+} + G_{-}]^R}{R!} \quad (21)$$

The power of R can be expanded with the binomial theorem

$$[X+Y]^R = \sum_{T=0}^R \frac{X^{R-T} Y^T R!}{(R-T)! T!} \quad (22)$$

which when substituted into equation (21) gives:

$$\exp[G_+ + G_-] = \sum_{R=0}^{\infty} \sum_{T=0}^{\infty} \frac{[G_+]^{R-T} [G_-]^T}{(R-T)! T!} \quad (23)$$

Substituting equation (23) into the rate equation (15) and expanding out the G terms:

$$W = A \int dt e^{[-\sum_k S_k (2\bar{n}_k + 1)]} \prod_{k=1}^N \sum_{R=0}^{\infty} \sum_{T=0}^R \frac{[S_k (\bar{n}_k + 1)]^{R-T} (S_k \bar{n}_k)^T}{(R-T)! T!} \quad (24)$$

$$\times \exp[-i\Delta E t / \hbar + i\omega_k (R-T)t - i\omega_k Tt]$$

and finally integrating over t:

$$W = A e^{[-\sum_k S_k (2\bar{n}_k + 1)]} \prod_{k=1}^N \sum_{R=0}^{\infty} \sum_{T=0}^R \frac{[S(\bar{n}+1)]^{R-T} [S\bar{n}]^T}{(R-T)! T!} \quad (25)$$

$$\times \delta\left(\frac{-\Delta E}{\hbar} + \sum_k \omega_k [R-2T]\right)$$

As previously discussed, the  $\bar{n}+1$  is the weight associated with the one phonon absorption process and the  $\bar{n}$  is the weight associated with the one phonon emission process. Since the bose factor approaches zero as the temperature goes to zero, the summation over T becomes unnecessary. Therefore, at low temperatures the sum over R becomes:  $[S^R/R!]$   $\delta_k(p_k + R)$  where  $p_k = \Delta E/(\hbar \sum \omega_k)$ . Thus, the R sum can be seen to enumerate the phonons with a weight  $e^{-S} S^R/R!$  (i.e.  $R=0,1,2,\dots$  are the  $0,1,2,\dots$  phonon processes) At high

temperatures the T sum becomes important and enumerates all possible combinations of 0,1,2,... phonon processes.

In Figure 4 the first few terms of the R and T sum are pictured. The negative values are emission processes and the positive values absorption processes. At low temperatures only the boxed terms are important, but as the temperature increases phonon emission becomes possible. Thus for a one phonon process either two phonons can be absorbed or emitted or one phonon can be absorbed and one phonon emitted. Thus, the T sum shows that all multiple phonon terms are actually built up from one phonon processes (see section III). In addition the effective coupling (weighting factor) of the phonon processes changes at higher temperatures. For example, a one phonon process (emission or absorption) is weighted simply by S, but a two phonon process has an additional weight associated with it. The emission and absorption are both weighted by  $S^2/2$  as at 0 K for absorption, but the one phonon emission and one phonon absorption, two phonon process is weighted by  $S^2$ . Hence, the weighting factor for the phonon processes becomes  $e^{-S} S^R$  at temperatures above 0 K whereas at 0 K it is  $e^{-S} S^R/R!$ .

The delta function indicates that only when the condition  $R=P_k+2T$  is met, is energy conserved and any contribution given to the rate. Substituting into equation (25) gives:

$$W = A \prod_{k=1}^N \sum_{P_k=-\infty}^{\infty} \sum_{T=0}^{\infty} \frac{[S(\bar{n}+1)]^{P_k+2T} [S\bar{n}]^T}{P_k+2T!} \quad (26)$$

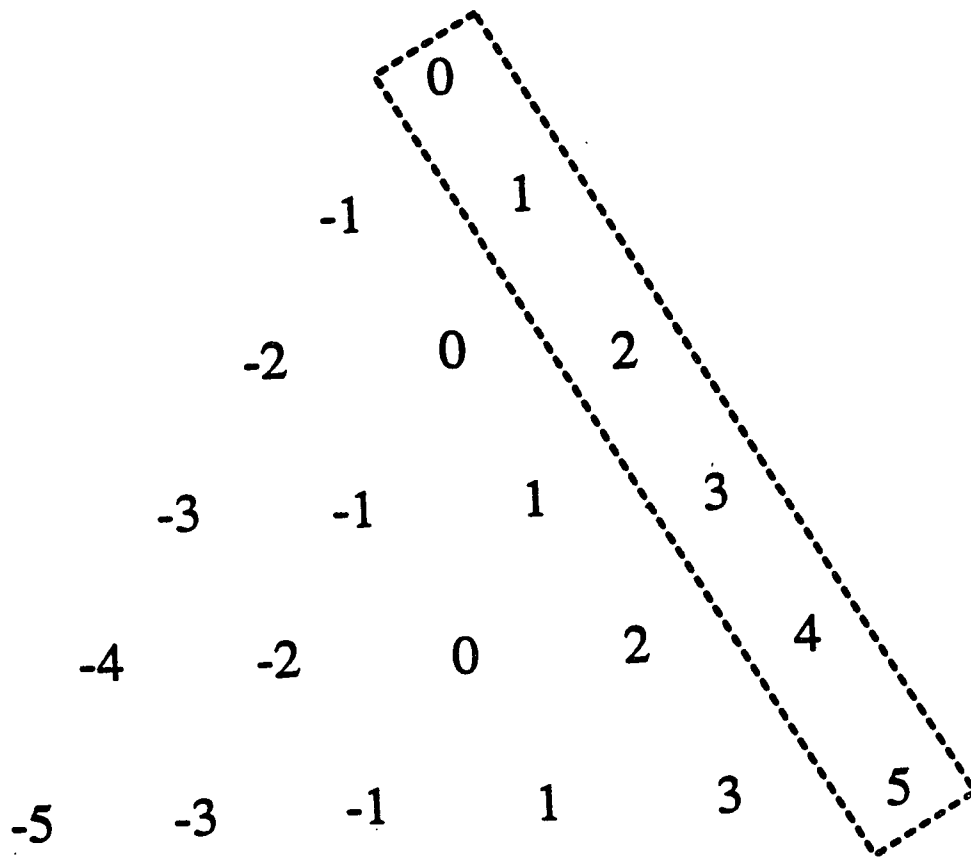


**Figure 4.** Diagram illustrating the effect of the R and T sums from equation 25. Negative values are emission processes and positive absorption

the change in variable requires a change in variables of the summations. The new ranges can be rationalized by noticing that since  $R$  runs from 0 to  $\infty$ , and  $T$  follows  $R$  the new range for  $T$  is from 0 to infinity. The  $P_k$  sum must run over  $-\infty$  to  $\infty$  since  $P_k$  is calculated from the energy gap and a system can have any possible range of energy gaps. The modified Bessel function is defined by [41]

$$I_{P_k}(Z) = \sum_{k=0}^{\infty} \frac{(Z/2)^{P_k+2T}}{T!(P_k+T)!} \quad (27)$$

The  $T$  sum can be written in this form by combining the  $\bar{n}+1$  and  $\bar{n}$  terms together by multiplying the equations by

$$\left[ \frac{\bar{n}_k + 1}{\bar{n}_k} \right]^{P_k/2} \times \left[ \frac{\bar{n}_k}{\bar{n}_k + 1} \right]^{P_k/2} \quad (28)$$

to give:

$$\left[ \frac{\bar{n}_k + 1}{\bar{n}_k} \right]^{P_k/2} I_{P_k}(2S_k[(\bar{n}_k + 1)\bar{n}_k]^{1/2}) \quad (29)$$

Because of the change in variables the  $P_k$  sum no longer enumerates the individual phonon processes. Since  $P_k$  now is summed over all possible phonons each  $P_k$  is determined by the columns instead of the rows in Figure 4. Thus for  $P_k=1$  any combination of phonon processes which leads to a one phonon absorption is accounted for. (i.e., 2 phonon absorptions plus one phonon emission or 8 phonon absorption plus 7 phonon emissions are

both equal  $P_k=1$ ) Thus the physical distinction of the phonon processes is lost.

Substituting equation 28 into equation (26) the rate equation becomes:

$$\begin{aligned}
 W = A \exp \left[ \sum_k S_k (2\bar{n}_k + 1) \right] \prod_{k=1}^N \sum_{P=-\infty}^{\infty} \left[ \frac{\bar{n}_k + 1}{\bar{n}_k} \right]^{P/2} \\
 \times I_P \left\{ 2S_k [(\bar{n}_k + 1)\bar{n}_k]^{1/2} \right\}
 \end{aligned} \tag{30}$$

which can be seen to match equation 19 derived in a mathematically more direct method.

**PAPER I.    TEMPERATURE    DEPENDENCE    OF  
ANTENNA    EXCITATION    TRANSPORT    IN  
NATIVE    PHOTOSYSTEM    I    PARTICLES**



**Temperature Dependence of Antenna Excitation Transport  
in Native Photosystem I Particles**

**Paul A. Lyle and Walter S. Struve**  
*Journal of Physical Chemistry* 1991, 95, 4152

**ABSTRACT**

The temperature dependence of polarized photobleaching dynamics was investigated through 680 nm pump-probe experiments in the Chl *a* antenna of native photosystem I particles (Chl/P700 ~ 200) from spinach. The anisotropic decay time is lengthened by an order of magnitude (from ~ 7 to ~ 62 ps) when the temperature is reduced from 290 to 38 K; most of this increase occurs between 65 and 38 K. The occurrence of this transition temperature in the tens of kelvin reflects the participation of protein phonons in antenna EET. The isotropic decay kinetics are considerably less temperature sensitive, indicating that the anisotropic and isotropic decays stem from different energy-transfer processes with contrasting temperature dependence. The 38 K photobleaching spectrum at 5 ps exhibits considerably more weighting in the lower energy Chl *a* spectral forms than the room-temperature spectrum, suggesting that rapid spectral equilibration occurs in the photosystem I antenna. In light of the phonon frequency and electron-phonon coupling parameters determined in independent PSI-200 spectral hole burning experiments, the quantitative temperature dependence in the anisotropic decay times is consistent with a theory for phonon-assisted EET in which the pertinent phonons are independent modes localized about the donor and acceptor chromophores.

## INTRODUCTION

The ultrafast electronic excitation transport (EET) dynamics in the Chl *a* antenna complex of native photosystem I particles [1] have been studied in several time resolved fluorescence [2-7] and pump-probe [8] experiments. With the exception of the fluorescence studies by Searle et al. [2] and by Mukerji and Sauer [4], these time-domain studies have been largely confined to room temperature antenna kinetics. Few time resolved experiments have directly observed the single step antenna EET dynamics, because the excited state population decays observed in emission studies are composite properties that encompass many EET steps in several different PS I antennae and the P700 reaction center [2-7]. Gillie et al. investigated the early time EET steps in the native PS I antenna through spectral hole-burning studies at 1.6 K [9]. While the overall PS I antenna fluorescence dynamics reported by different groups are substantially in agreement, large discrepancies have emerged among the single step EET kinetics measured in the room temperature polarized pump-probe experiments [8], the dynamics observed in the low temperature hole-burning experiments [9], and the hopping times indirectly inferred from room temperature fluorescence studies [10]. The isotropic fluorescence decay kinetics observed in Chl *a* core antennae of PS I from *Chlamydomonas reinhardtii* [10] were analyzed in terms of a regular lattice model [11] to yield a calculated chromophore-to-chromophore single-step transfer time of ~200 fs. The depolarization lifetime observed in Chl *a* antenna photobleaching transients between 660 and 681 nm in native PS I particles from spinach ranges from ~5 to ~13 ps, depending on the

---

probed wavelength [8]. The fact that this depolarization timescale (which arises from EET between chromophores with contrasting transition moment orientations [12]) is considerably slower than the single step hopping time inferred by Owens et al. for *Chlamydomonas reinhardtii* [10] suggested that the depolarization arises from EET between clusters of chromophores rather than between individual chromophores [13]. In contrast, the zero-phonon hole widths observed in the native PS I Chl *a* antenna correspond to hopping times as long as 300 ps [9]. Hence, the time and frequency domain experiments may have monitored different early time events. Alternatively, a strong temperature dependence in the transport rates may decelerate EET processes that proceed in the femtosecond to picosecond timescale at room temperature to the hundreds of picoseconds at 1.6 K. At temperatures higher than 2-3 K, additional processes such as spectral diffusion and pure dephasing begin to contribute to zero-phonon hole widths. Hence, extension of the room temperature time domain studies to low temperatures is necessary in order to reconcile them with the frequency domain experiments.

Quantum mechanical theories have been formulated for the temperature dependence of donor acceptor processes (such as electron transfer and EET) in which the pertinent coupling does not depend explicitly on the intramolecular vibrational or medium phonon coordinates [14,15]. In such cases, temperature sensitivity in the kinetics stems from the thermally averaged Franck-Condon overlap between the initial and final vibrational and/or phonon states, which are modeled as displaced harmonic oscillators. For EET across a donor acceptor electronic energy gap  $\Delta E$  (which must be compensated by an appropriate

combination of  $m$  vibrational quanta  $\hbar\omega$  and  $p$  phonon quanta  $\hbar\omega_s$ ), the donor→acceptor transition rate varies with temperature as [15]

$$W = \frac{2\pi|V|^2}{\hbar^2\omega_s} e^{[-S_s(2\bar{n}_s+1)-S(2\bar{n}+1)]} \sum_{m=-\infty}^{\infty} \left( \frac{\bar{n}_s+1}{\bar{n}_s} \right)^{p/2} \times I_{|p|}[2S_s[\bar{n}_s(\bar{n}_s+1)]^{1/2}] \left( \frac{\bar{n}+1}{\bar{n}} \right)^{m/2} I_{|m|}[2S[\bar{n}(\bar{n}+1)]^{1/2}] \quad (1)$$

where  $S$  and  $S_s$  are the Huang-Rhys factors for the chromophore and protein reorganizations associated with the donor-acceptor EET process,  $p = (\Delta E - m\hbar\omega)/\hbar\omega_s$  is the number of phonons required to make up the donor acceptor electronic plus vibrational energy difference, and  $I_{|p|}$  is the modified Bessel function of integer order  $p$  [16].  $V$  is the matrix element for electronic (frequently assumed to be dipole-dipole [17]) coupling responsible for EET, while  $\bar{n}(\bar{n}_s)$  is the mean vibrational (phonon) occupation number, given by  $1/[\exp(-\hbar\omega(\omega_s)/kT) - 1]$ , at temperature  $T$ . Gillie et al. reasoned that since the lowest frequency antenna Chl  $a$  vibrational mode with appreciable Franck-Condon intensity occurs at  $262 \text{ cm}^{-1}$  and since electronic energy gaps this large are unlikely in PS I core antenna EET [9], chromophore vibrational mode participation is likely to be minimal. They therefore used limiting forms of Equation 1 for  $\hbar\omega/kT \ll 1$  and  $\gg 1$  in the special case where  $m = 0$  and  $S = 0$  (which is tantamount to assuming that the donor and acceptor chromophores interact with the same phonon modes, viz. the “delocalized phonon” model discussed in the DISCUSSION section below) to account for the differences in EET timescales observed in the time- and frequency-

domain experiments. Using plausible values for the phonon frequency  $\omega_s$  (obtained from phonon sideband shapes in hole burning spectra [9]) and  $S_s$  as well as a reasonable dipole-dipole coupling strength ( $V \sim 5 \text{ cm}^{-1}$ ), they were able to simulate the apparent disparity between the room temperature and low temperature kinetics measured in the time- and frequency-domain studies.

In this paper, we report an extension of our room-temperature polarized pump-probe study of antenna EET in PSI-200 [8] to a sequence of temperatures between 38 K and 292 K. The temperature dependence of EET single step kinetics is therefore monitored directly for the first time in the PS I antenna. The anisotropy decay at 38 K is  $\sim$  one order of magnitude slower than at room temperature. The isotropic photobleaching decay has been characterized for the same temperatures; its sensitivity to temperature is far less marked than that of the anisotropic decay. While the anisotropic decay's temperature variation can be modeled approximately with Equation 1 using suitable choices of parameters, an extrapolation of the depolarization lifetime to 1.6 K yields a lifetime considerably longer than the  $\sim 300 \text{ ps}$  inferred from the hole burning experiments. These results suggest that while the anisotropy decay is strongly temperature dependent for  $T < 60 \text{ K}$ , it is unrelated to the zero-phonon linewidths seen in the hole burning experiments. This and the fact that the isotropic and anisotropic decays exhibit distinctly different temperature behavior can be rationalized using a PS I antenna model in which the Chl *a* pigments are grouped into similar clusters of energetically inequivalent spectral forms.

---

## EXPERIMENTAL METHOD AND DATA ANALYSIS

The native photosystem I particles (PSI-200, with antenna Chl/P700 ratio ~200 [1]) were extracted from spinach chloroplasts using the method described by Mullet et al. [19]. The Chl *a*/Chl *b* ratio in the light-harvesting antenna, which contains ~100 chromophores, is ~3.5. The overall Chl *a*/Chl *b* ratio in the core and peripheral antennae combined is ~6. PSI-200 particles also contain the P700 reaction center and associated electron acceptors, and manifest the functions of PS I in intact thylakoids [1]. Particles were stored at 77 K in a buffered glycerol-water mixture with 0.1% Triton X-100. They exhibited static Chl *a* antenna and P700 absorption spectra (660 - 720 nm) identical to those shown by the PSI-200 particles used earlier.

The pump-probe apparatus was similar to one described previously [8]. A CW frequency doubled mode-locked Nd:YAG laser furnished 532 nm pulses (~70 ps fwhm) at 1W average power and 76 MHz repetition rate. It pumped a dual-jet dye laser (DCM lasing dye, DDCI saturable dye) whose vertically polarized output pulses were wavelength tunable from 645 to 685 nm using a single plate birefringence filter. Autocorrelation traces at 680 nm, the wavelength used in this study (see below), were typically 3 ps fwhm. The cavity dumper used in the room temperature study was omitted, as the larger single pulse energies so obtained incurred exciton annihilation artifacts [8] in PSI-200. The pump and probe laser beams, derived from the dye laser output with an inconel coated beamsplitter, were modulated at 6.5 and 0.5 MHz respectively with Isomet 1206C acoustooptic modulators. The probe

beam polarization was fixed using a Glan-Thompson calcite polarizer aligned at 45 degrees from the vertical laser polarization; the pump polarization was selectable among parallel, perpendicular, and magic-angle polarizations (the latter at 9.7 degrees from the vertical). A Micro-Controle UT100125PP translation stage swept the pump pulse delay. The pump and probe beams, initially parallel and separated by ~6 mm, were focussed into the sample with a 7.3 cm focal length lens. An EG&G FOD-100 photodiode monitored the transmitted probe beam. The photobleaching signal at the 7.0 MHz sum frequency was detected in the phase locked single-sideband mode using a modified Drake R-7A radio receiver [20]. Pump-probe data were transmitted during scans to a DEC MINC-23 computer, and subsequently analyzed in a DEC VAXstation 2000.

PSI-200 samples (~0.2 optical density at 680 nm) were housed between  $\lambda/4$  quartz flats separated by a 1 mm thick neoprene spacer. This window assembly was in thermal contact (through indium foil) with the end of a 2.25 cm diameter Cu cold finger in an Air Products DE202 closed-cycle He expander module. The cold-finger temperature (monitored through a chromel/Au-0.7%Fe thermocouple embedded ~5 mm from its end) was controllable from 12 to 300 K. The sample temperature, measured directly with a calibrated Cu-constantan (Type T) thermocouple immersed between the cell windows and threaded through a sealed aperture in the neoprene spacer, could be cooled to 34 K. The window assembly was partially shielded from the room temperature outside walls of the Displex with a 3.8 cm diameter Ni-plated Cu cylindrical shroud with open 2 cm diameter windows for incoming and exit beams. Without the shroud, the lowest attainable temperature was ~55 K. Sample



heating by the laser beams typically raised the sample temperature by 2 K at the lowest temperatures (larger temperature increments were observed with magic-angle than with parallel or perpendicular pump pulses, since the relative beam intensities were  $\cos^2(9.7^\circ) : \cos^2(45^\circ) = 1 : 0.52$  in our polarization scheme). Temperature measurements were influenced somewhat by the proximity of the thermocouple to the laser beam intersection; the temperature reading error was estimated to be  $\sim 2$  K.

The dynamic linear dichroism for a homogeneous solution of a chromoprotein containing two identical chromophores A and B with contrasting protein fixed transition moment orientations  $(0,0,1)$  and  $(\alpha,\beta,\gamma)$  has been treated by several authors [12,21,22]. If chromophore A is excited by a laser pulse at time  $t=0$  and if the subsequent excited state populations of chromophores A and B are given by  $P(t)s(t)$  and  $P(t)[1-s(t)]$  respectively, the most general form of the resulting polarized transients  $A_{\parallel}(t)$ ,  $A_{\perp}(t)$  is given by

$$A_{\parallel}(t) = P(t)[1+0.8[(1-a)s(t)+a]] \quad (2a)$$

$$A_{\perp}(t) = P(t)[1-0.4[(1-a)s(t)+a]] \quad (2b)$$

where  $P(t)$  is the isotropic decay measured using magic-angle pump pulses. The residual anisotropy parameter  $a$  is related to the projection  $\gamma$  of chromophore B's transition moment along that of chromophore A through  $a = P_2(\gamma) = (3\gamma^2-1)/2$  [11]. Equations 2 imply that the initial ratio  $A_{\parallel}(0)/A_{\perp}(0)$  of polarized transients equals 3 in the absence of unresolvably rapid depolarization (e.g. "monomer anisotropy" [21]). This condition is approximately met in all of the polarized transients observed for the PS I Chl  $a$  antenna in the present work and in the

room temperature study [8]. Evidently, little subpicosecond depolarization arises in single wavelength pump-probe experiments in this antenna, in contrast to our experience with the BChl *a*-protein complex from the green sulfur bacterium *Prosthecochloris aestuarii* [23]. Earlier analyses of polarized transients for photosynthetic systems first fitted the empirical isotropic decay function  $P(t)$  with a multiexponential decay law, and then held the optimized isotropic decay parameters fixed in a linked deconvolution of the polarized transients  $A_{\parallel}(t)$ ,  $A_{\perp}(t)$  using Eqs. 2 [24]. In this work, the anisotropic parameters in the decay function  $s(t)$  (which describes the equilibration of excitation between chromophores A and B in the simple chromoprotein model) were instead extracted by first computing the anisotropy function point by point,

$$r(t) = \frac{I_{\parallel}(t) - I_{\perp}(t)}{I_{\parallel}(t) + 2I_{\perp}(t)} \quad (3)$$

This function was then deconvoluted from the laser autocorrelation function using the decay law

$$r(t) = 0.4[(1-a)s(t) + a] \quad (4)$$

in which  $s(t)$  is phenomenologically modeled with the single exponential function  $\exp(-t/\tau)$ . This approach obviates the combined use of the magic-angle profile  $P(t)$  and the polarized profiles  $A_{\parallel}$ ,  $A_{\perp}$  in evaluating the anisotropy decay, and is advantageous at the lower temperatures where magic-angle probe pulses incur more sample heating than parallel or perpendicular probe pulses (vide supra).

## RESULTS

We preface the discussion of our time resolved photobleaching results by showing photobleaching spectra for the PSI-200 particles at two contrasting temperatures in Figure 1. For comparison, we also include the room temperature PSI-200 static absorption spectrum in Figure 1. The Chl *a* absorption region (660-690 nm) in the static absorption spectrum is several times broader than the absorption spectrum of Chl *a* monomers in solution. The Chl *a* antenna thus contains several spectral Chl *a* forms, which may arise from site inhomogeneities and/or exciton splittings [5,25]. The photobleaching spectra, obtained at 10 ps after excitation and normalized to the square of the laser power at each wavelength, clearly indicate that the 660-680 nm Chl *a* antenna spectrum is not uniformly bleached at this time. The PS I core antenna fluorescence band maximum is located at 690 nm [4], so that some of the signal at the long wavelength edge of the photobleaching spectra at both temperatures is likely due to stimulated emission. Since the Einstein coefficients for absorption and stimulated emission are equal in singlet-singlet electronic transitions, the integrated stimulated emission spectrum cannot be larger than that for photobleaching. Hence, the spectra for wavelengths shorter than ~680 nm in Figure 1 accurately reflect the relative excited state populations of the Chl *a* spectral forms in the PS I antenna. The long wavelength band maximum of the 38 K photobleaching spectrum is shifted several nm to the blue of the room temperature photobleaching spectrum; this mirrors a similar blue shift observed in the corresponding static absorption spectra [26]. The 38 K photobleaching spectrum falls off

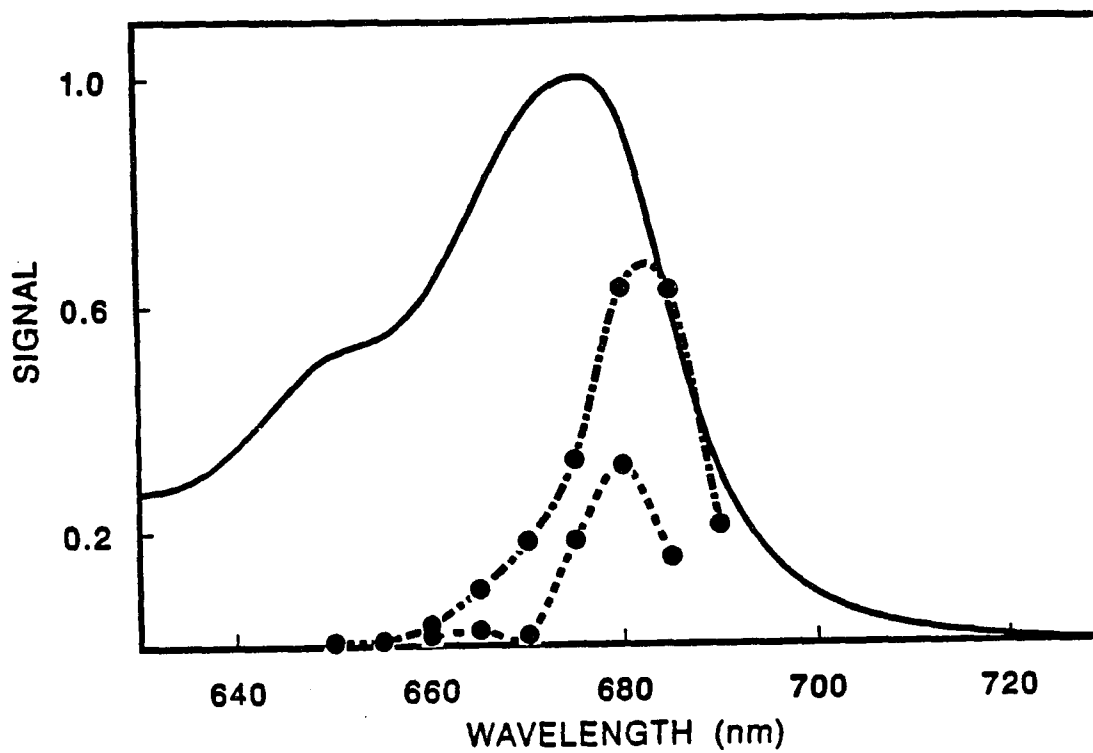


**Figure 1.** Photobleaching spectra of PSI-200 at 38 K (dashed) and at room temperature (dot-dashed; T. P. Causgrove, S. Yang, and W. S. Struve, unpublished data), normalized to the square of the average laser power. Static room-temperature absorption spectrum is given by the solid curve

more sharply to the blue than the room temperature spectrum, suggesting that the antenna excitation thermally equilibrates among the spectral forms. This precluded studying the low temperature PSI-200 anisotropy decays at all of the wavelengths investigated in the room temperature work [8], since the photobleaching signal/noise was too low for quantitative anisotropy measurements at wavelengths shorter than  $\sim 675$  nm for temperatures near 38 K. The time scale for the uphill/downhill thermalization implied in Figure 1 is considerably faster than those of our anisotropy decays, particularly at the lowest temperatures (see below). This reinforces the impression that the anisotropic decays, measured in the present and earlier [8] polarized pump-probe studies, view EET events that are different from those monitored in the isotropic fluorescence and pump-probe decays. The magic-angle pump-probe profiles were obtained at 680 nm at each of the temperatures studied; the optimized parameters for triexponential fits to these profiles are typified in Table I. The somewhat random variations (100 to 161 ps) in the medium and long component lifetimes  $\tau_2$  and  $\tau_3$  between 38 and 167 K arise partly from covariance between the triexponential parameters. Very similar fits to the magic-angle decays could be achieved by freezing  $\tau_3$  at values ranging from  $\sim 100$  to  $\sim 250$  ps, and the experimental magic-angle profiles exhibited little temperature variation in this regime. A minor source of error in the measurement of component lifetimes longer than 100 ps arose from using translation stage sweeps over intervals shorter than 100 ps at the higher temperatures, where the depolarization of interest (see below) was considerably more rapid. In Figure 2, we show typical 680 nm polarized pump-probe profiles for PSI-200 at 167 K. The corresponding anisotropy function, defined in Equation 3, is shown in Figure 3, along

**Table I**      Triexponential Parameters for Magic-Angle  
Photobleaching Profiles in PSI-200 at 680 nm

---


$$P(t) = A_1 \exp(-t/\tau_1) + A_2 \exp(-t/\tau_2) + A_3 \exp(-t/\tau_3)$$


---

Temp, K	$\tau_1$ ( $A_1$ ), ps	$\tau_2$ ( $A_2$ ), ps	$\tau_3$ ( $A_3$ ), ps
38	3 (0.54)	23 (0.30)	130 (0.16)
49	3 (0.54)	20 (0.30)	130 (0.16)
65	5 (0.54)	33 (0.32)	110 (0.14)
77	6 (0.57)	35 (0.33)	161 (0.10)
167	5 (0.54)	38 (0.30)	100 (0.16)
292	3 (0.50)	30 (0.19)	220 (0.13)

---

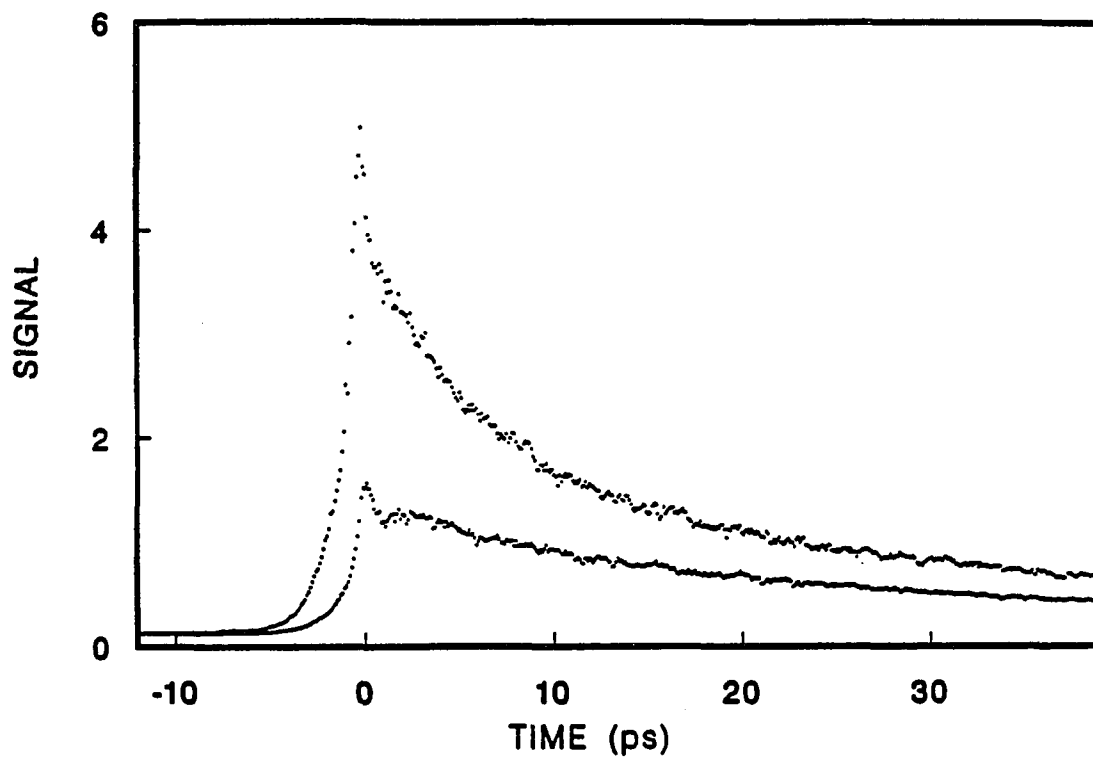


**Figure 2.** Polarized photobleaching profiles for PSI-200 at 167 K. The upper (lower) curve gives the parallel (perpendicular) photobleaching signal

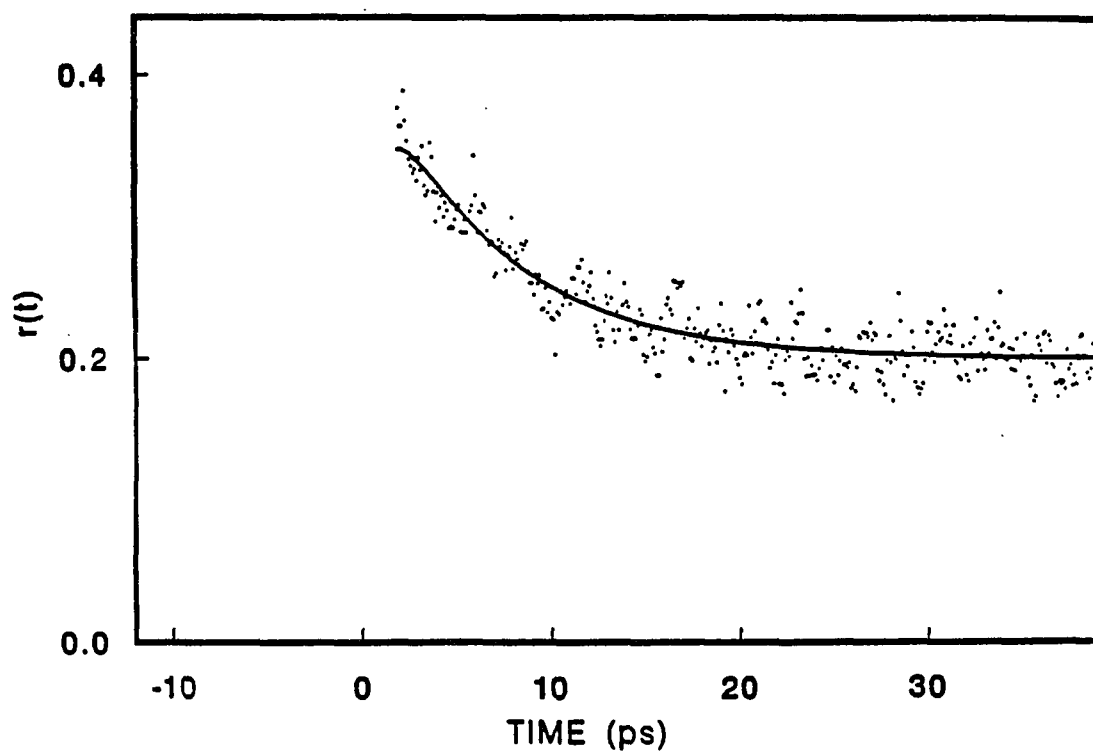


**Figure 3.** Anisotropy function  $r(t)$  for PSI-200 at 167 K, computed from the profiles in Figure 2 using equation 3



with the optimized convolution of the laser autocorrelation function with the model function in Equation 4. In all cases, the anisotropy functions extrapolated to  $r(0) = 0.4 \pm 0.05$  at zero time, so that subpicosecond depolarization is absent in this antenna. The optimized anisotropy decay times  $\tau$  and residual anisotropy parameters  $a$  from nonlinear least-squares fits of Equation 4 to the anisotropy functions at this and several other temperatures are listed in Table II. The nonzero residual anisotropy parameter (which must arise from local ordering in the Chl  $a$  antenna chromophore architecture [12]) is relatively insensitive to temperature and exhibits values similar to those measured at 681 nm at room temperature [8]. (This suggests that cooling the Chl  $a$  antenna to 38 K does not effect gross changes in the chromophore organization, since  $a$  depends on the relative orientations of donor and acceptor transition moments.) The anisotropy decay time  $\tau$  varies little for temperatures between 77 and 292 K, as shown in Figure 4 and Table II. It increases by nearly an order of magnitude (from  $\sim 9$  to  $\sim 62$  ps) as the temperature is lowered from 77 to 38 K. The occurrence of this transition temperature in the tens (rather than hundreds) of K arises from participation in EET by low frequency protein phonons (rather than intramolecular chromophore vibrations) as promoting modes for photosystem I antenna EET. This is in agreement with the conclusion independently reached by Gillie et al. [9] on the basis of their 1.6 K spectral hole-burning study.

**Table II**      Anisotropic Parameters for Polarized Photobleaching Profiles From PSI-200 at 680 nm

$r(t) = 0.4[(1 - a) \exp(-t/\tau) + a]$		
Temp, K	$\tau$ , ps	$a$
38	$62 \pm 5$	0.61
49	$31 \pm 4$	0.55
65	$13 \pm 2$	0.60
77	$9 \pm 2$	0.50
167	$5 \pm 2$	0.52
292	$7 \pm 2$	0.60

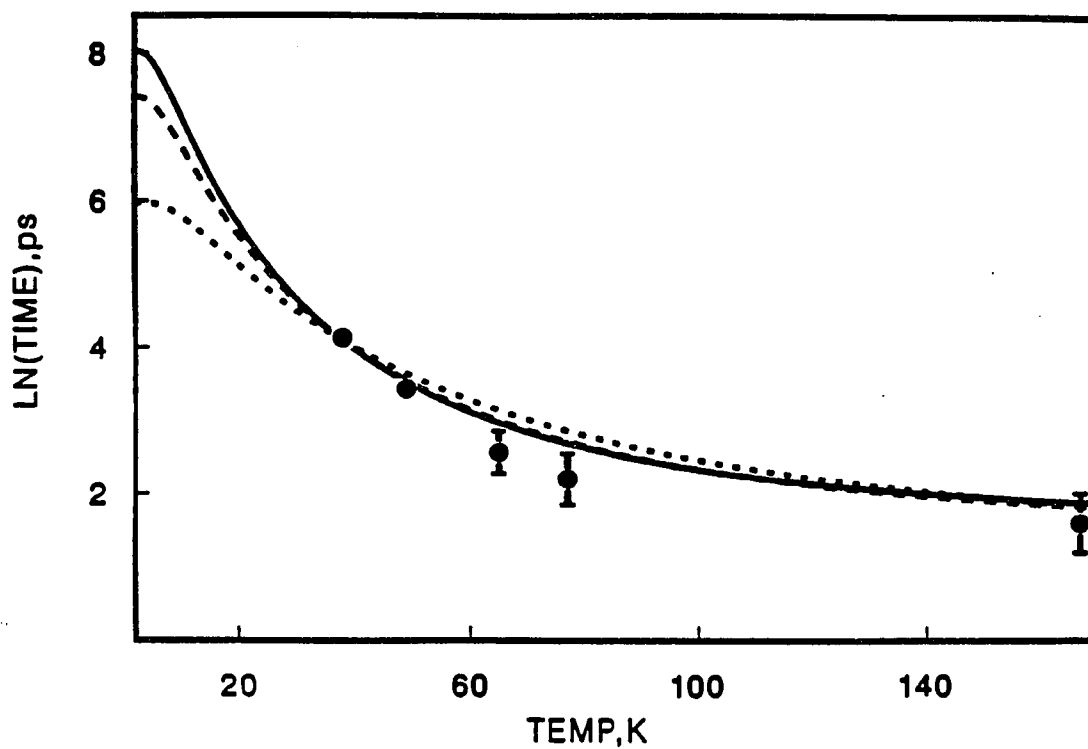


**Figure 4.** Anisotropy decay times versus temperature, data points; theoretical EET times computed using Equation 1 with  $m = 0$ ,  $S = 0$ , and  $p = 4$  (continuous curve),  $p = 5$  (dashed curve), and  $p = 6$  (dotted curve). Fitting ranges for the other parameters are discussed in text. This case ( $m = 0$ ,  $S = 0$ ) corresponds to the “delocalized phonon” model

## DISCUSSION

### Delocalized Phonon Model

The generic behavior predicted by Equation 1 over a broad temperature range for the single step EET kinetics with  $m=0$  and  $S=0$  (i.e. in the absence of a promoting vibrational mode) is typified by Figure 5. This is tantamount to assuming that EET is assisted by a single phonon mode with frequency  $\omega_s$ , whose spatial extent is comparable to or greater than the donor-acceptor separation  $R$ . (This corresponds to the “delocalized phonon” case described by Gillie et al. [9]. It is applicable to processes in which the two chromophores are so close together (e.g. electron transfer in reaction centers) that both pigments interact physically with the same protein phonon modes. Its pertinence to long range EET processes between chromophores complexed to different protein subunits is less certain.) Figure 5 illustrates the calculated single step hopping times for a system in which the phonon mode frequency, the EET Huang Rhys factor, and the dimensionless energy gap are  $\omega_s = 13 \text{ cm}^{-1}$ ,  $S_s = 0.5$ , and  $p = \Delta E/\hbar\omega_s = 5$  respectively. At very low temperatures ( $T < 5 \text{ K}$  in this example), the hopping time approaches the constant [15]

$$\tau^{-1} = \left( \frac{2\pi|V|^2}{\hbar^2\omega_s} \right) \exp(-S_s) S_s^p / p! \quad (5)$$

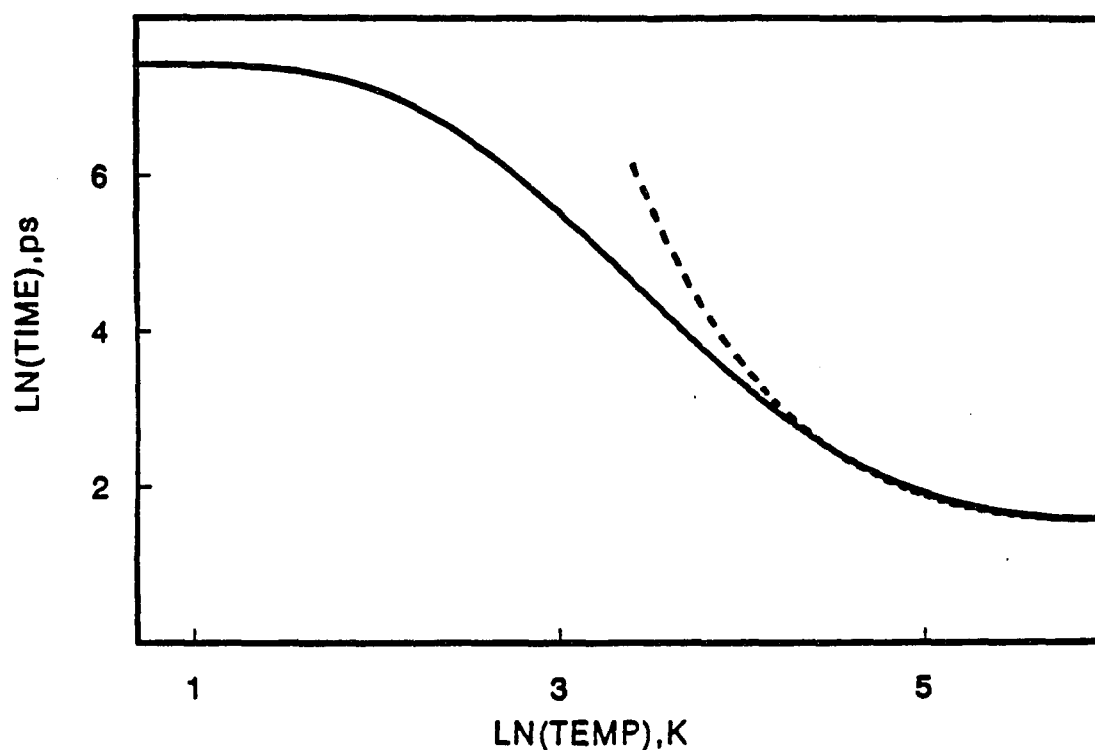


**Figure 5.** Generic temperature dependence of the EET transition rate between 0 and 400 K for  $m = 0$ ,  $p = 5$ ,  $S_s = 0.5$ , and  $\omega_s = 13 \text{ cm}^{-1}$ . Solid curve is computed from Equation 1; dashed curve is computed using the high-temperature asymptotic form, Equation 6. The low-temperature limit (Equation 5) is given by the horizontal portion of solid curve at left

In the limit of high temperatures  $kT \gg \hbar\omega_s$ , the hopping rate behaves as

$$\tau^{-1} = \left( \frac{\pi}{\hbar^3 \omega_s S_s kT} \right)^{1/2} |V|^2 \quad (6)$$

$$\exp[-(\Delta E - S_s \hbar \omega_s)^2 / 4 S_s \hbar \omega_s kT]$$

Equation 6 results from the twofold approximation of representing the modified Bessel function in Equation 1 with the large- $z$  asymptotic expansion [16]

$$I_{|p|}(z) \sim \frac{e^z}{\sqrt{2\pi z}} \left[ 1 - \frac{\mu-1}{8z} + \frac{(\mu-1)(\mu-9)}{2!(8z)^2} - \frac{(\mu-1)(\mu-9)(\mu-25)}{3!(8z)^3} + \dots \right] \quad (7)$$

where  $\mu = 4p^2$ , and then ignoring the integers in the numerator of each term. The latter approximation is compared with the exact expression (Equation 1) in Figure 5, where it is seen that the high temperature version begins to fail for  $T < 80$  K with these choices of parameters. The transition temperature  $T_s$  between the low and high temperature regimes is sensitive to the phonon frequency  $\omega_s$  through  $kT_s \sim \hbar\omega_s$ ; the pertinent value of  $\omega_s$  was deduced to be  $\sim 20$   $\text{cm}^{-1}$  in the hole-burning experiments [9]. The Huang Rhys factor observed for phonon sidebands of holes burned into the PSI-200 antenna Chl *a* absorption spectrum, which corresponds to protein-pigment reorganization attending the  $Q_y$  electronic transition, is  $\sim 0.8$ . The value of the Huang Rhys factor pertinent to the donor acceptor

excitation transfer process, which is not directly measured in the hole burning experiments, is uncertain; it cannot be appreciably larger than the 0.8 value observed for the  $Q_y$  electronic transition in a single chromophore. (This contrasts with the large values of  $S$  observed in the cytochrome  $\rightarrow$  chlorophyll electron transfer in the strongly coupled *Chromatium* system [15].) The energy gap  $\Delta E$  for the nearly isoergic EET processes monitored in our single wavelength depolarization experiments cannot exceed the  $Q_y$  absorption bandwidth of single Chl *a* spectral forms in the antenna, i.e.  $\Delta E \sim 300 \text{ cm}^{-1}$  at most. This feature distinguishes our situation from the electron transfer steps in *Chromatium* ( $\Delta E = 400 \text{ cm}^{-1}$ ) and in the bacterial reaction center ( $\Delta E \sim 4000 \text{ cm}^{-1}$  [27]); it physically limits realistic values of the reduced energy gap to  $p < 15$  when  $\omega_s = 20 \text{ cm}^{-1}$ . In strongly exoergic (or activationless) processes like the bacterial reaction center electron transfer, the reduced energy gap is essentially the same as the Huang-Rhys factor, i.e.  $S = \frac{1}{2}\Delta^2 \sim p$ , where  $\Delta$  is the equilibrium displacement in the phonon (or vibrational) mode [18]. The latter restriction does not apply to the far less exoergic EET processes viewed in this work, and these parameters were varied independently. Extensive covariance among the parameters  $V$ ,  $\omega_s$ ,  $p$ , and  $S_s$  prevents unique convergence in Marquardt least-squares fits of Equation 1, and so these parameters were varied manually in an interactive procedure. Typical data fits with  $p = 4, 5$ , and  $6$ , adjusted to pass through the points at  $38$  and  $167 \text{ K}$ , are in Figure 4. The ranges for the remaining parameters that produce these and similar fits are  $0.3 < S_s < 0.4$  and  $10 \text{ cm}^{-1} < \omega_s < 20 \text{ cm}^{-1}$  (for  $p = 4$ ),  $0.4 < S_s < 0.6$  and  $10 \text{ cm}^{-1} < \omega_s < 17 \text{ cm}^{-1}$  (for  $p = 5$ ), and  $0.6 < S_s < 0.8$  and  $10 \text{ cm}^{-1} < \omega_s < 15 \text{ cm}^{-1}$  (for  $p = 6$ ). For these values of  $p$ , the plots of calculated lifetimes exhibit insufficient

insufficient curvature (cf. Figure 4) to pass through the data points for temperatures intermediate between 38 and 167 K. These discrepancies are somewhat larger than the lifetime error bars in Figure 4. The value of the EET coupling matrix element  $V$  in these fits is typically  $\sim 7 \text{ cm}^{-1}$ . The energy gap  $\Delta E$  for  $p = 5$ ,  $\omega_s = 15 \text{ cm}^{-1}$  is  $75 \text{ cm}^{-1}$ , which is in a physically acceptable regime. The low temperature extrapolation of these fits (cf. Figure 5) yields asymptotic anisotropic lifetimes  $1.5 \text{ ns} < \tau < 2.0 \text{ ns}$ , which are several times larger than the 300 ps single step hopping time deduced from the PSI-200 hole burning experiments at 1.6 K [9]. Poorer fits are obtained with smaller reduced energy gaps  $p$ . Considerably enhanced curvature (and hence improved fits) can be forced by manipulating  $p$  to values as high as 10. This in turn requires Huang Rhys parameters  $S_s$  that appear unphysically large ( $\sim 1.1$ ) for antenna EET between similar Chl *a* chromophores. The low temperature limit for the depolarization lifetime is then pushed (unrealistically) into the tens of ns (cf Equation 5). Increasing the reduced energy gap  $p$  also requires reduction of the phonon frequency  $\omega_s$ ; for  $p = 10$ , the phonon frequency that yields an optimum fit is  $\sim 5 \text{ cm}^{-1}$ . Such low values are inconsistent with the phonon sideband contours observed in Chl *a* antenna hole burning [9], which are dominated by a mean phonon frequency of  $\sim 20 \text{ cm}^{-1}$ .

### Localized Phonon Model

We therefore consider a model for phonon assisted EET in which the donor and acceptor chromophores interact with physically independent phonon modes. Such a situation could arise if the two pigments are complexed with different protein subunits (e.g. as in the



case of BChl *a* chromophores belonging to different clusters of seven pigments in the BChl *a*-protein from *Prosthecochloris aestuarii* [28]). If the two phonon modes exhibit the same frequency, this is equivalent to using Equation 1 with  $S = S_s$ ,  $\omega = \omega_s$ , and  $\bar{n} = \bar{n}_s$ ; the electronic energy gap  $\Delta E$  is matched here by appropriate combinations  $(m + p)\hbar\omega_s$  of phonon quanta. (The separation of nuclear motions into intramolecular and medium modes in Equation 1 is arbitrary [15]; the convolution of vibrational and phonon lineshape functions leading to Equation 1 can be applied equally well to two independent phonon modes. This case was termed the “localized phonon” model by Gillie et al. [9].) In this model, the low- and high-temperature limits of the EET rate, Equations 5 and 6, are replaced by

$$\tau^{-1} = \frac{2\pi|V|^2}{\hbar^2\omega_s} \exp(-2S_s) \sum_{m=0}^{\infty} \frac{S_s^p S_s^m}{p!m!} \quad (8)$$

and

$$\tau^{-1} = \left( \frac{\pi}{2\hbar^3\omega_s S_s kT} \right)^{\frac{1}{2}} |V|^2 \exp[-(\Delta E - 2S_s\hbar\omega_s)^2 / 8S_s\hbar\omega_s] \quad (9)$$

Since the phonons interacting with donor and acceptor chromophores are essentially independent in this model, the respective protein displacements in single wavelength pump-probe experiments are equal (but opposite); they are also equal to the protein displacement accompanying an electronic transition in a single Chl *a* chromophore. Hence, the Huang Rhys factor in the “localized phonon” model should be identical to that observed in the PS

I Chl *a* antenna hole burning experiments,  $S \sim 0.8$  [9]. We show in Figure 6 a representative data fit using Equation 1 specialized to two identical phonon modes. For  $S_s = 0.8$  and  $\hbar\omega_s = 20 \text{ cm}^{-1}$ , the fit is optimized with  $p = 9$  and  $V = 16.6 \text{ cm}^{-1}$ ; it is better than any of the fits obtained using the “delocalized phonon” model, particularly for physical values of  $S_s$  and  $\hbar\omega_s$ . The low temperature limit of the transition rate  $\tau^{-1}$  (Equation 8) for these parameters is ca. 1.6 ns. The ranges of parameters yielding similar fits were  $0.7 < S_s < 0.9$ ,  $15 \text{ cm}^{-1} < \omega_s < 22 \text{ cm}^{-1}$ , and  $p = 8$  to 9. The corresponding ranges of the interaction matrix element  $V$  and the low-temperature transition rate were 9.4 to 16.6  $\text{cm}^{-1}$  and 0.9 to 3.6 ns. It is thus clear that the temperature dependence in our depolarization lifetimes is more consistent with the “localized phonon” description, in view of the constraints placed on the values of  $S_s$  and the phonon frequency by the hole burning experiments.

Another issue is the question of why even the “localized phonon” fits predict low temperature depolarization lifetimes several times longer than the 1.6 K Chl *a* antenna hole-burning lifetime of  $\sim 300$  ps. Since processes extraneous to excited state decay (e.g. pure dephasing) contribute to zero-phonon hole widths, such lifetime measurements actually give lower limits to the true lifetime particularly for the extremely sharp holes that accompany decays requiring several hundred picoseconds. Secondly, non-Förster (e.g. coherent) EET mechanisms which may be overshadowed at higher temperatures, but may become important at lower temperatures by virtue of a weaker temperature dependence can render a lifetime shorter than predicted by Equation 5 or 8. Finally, we have observed earlier that the anisotropic decay dynamics are unrelated to the magic-angle decays in native PSI-200

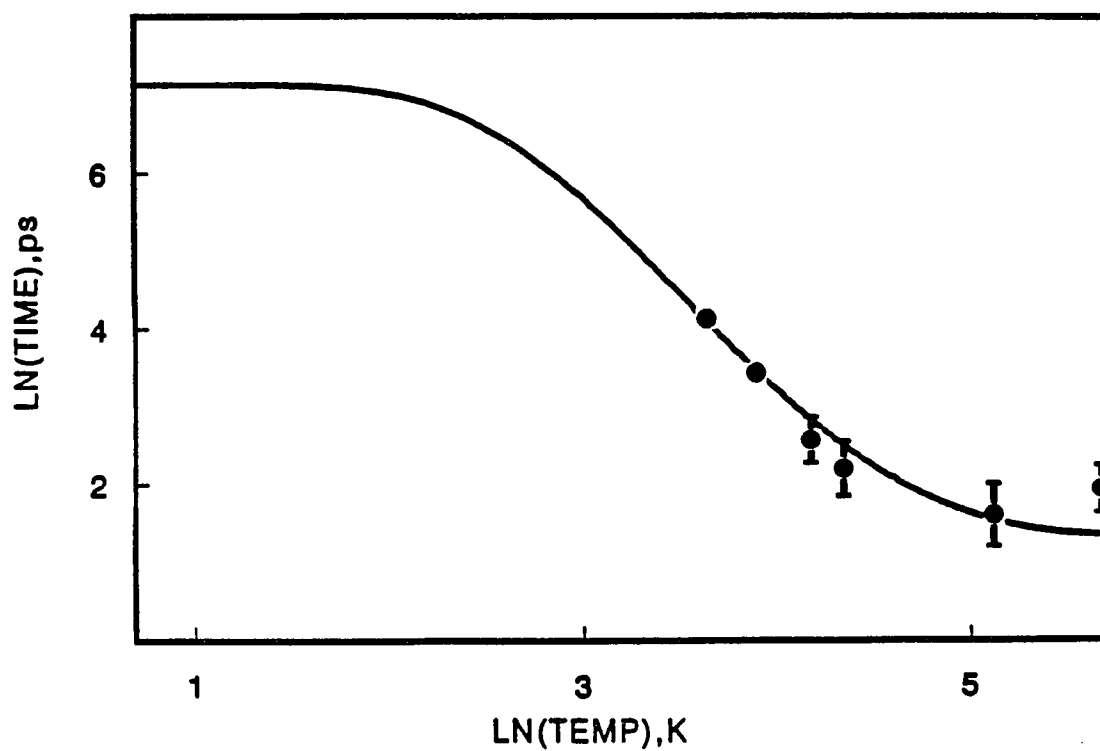


**Figure 6.** Anisotropic decay times versus temperature, data points; theoretical EET times calculated from "localized phonon" model with  $(m+p)=9$ ,  $S_s=0.8$ , and  $\omega_s=20 \text{ cm}^{-1}$ , continuous curve

particles [8], in P700-enriched PSI-60 particles [13], and in the BChl *a*-protein complex from *Prosthecochloris aestuarii* [23a]. The photobleaching spectra imply *a fortiori*, in the cases of PSI-200 (Section III) and the BChl *a*-protein, that the uphill/downhill EET steps in spectral equilibration occur on a faster timescale ( $< 1$  ps) than the anisotropic decay times observed in these systems. Similarly, Eads et al. detected subpicosecond Chl *b*  $\rightarrow$  Chl *a* PS I antenna EET in fluorescence upconversion experiments [29]; an analysis of PS I fluorescence decays using a regular lattice model for the core antenna estimated single step times of  $\sim 200$  fs [10]. It thus appears that single wavelength pump-probe experiments selectively project out the slower dynamics of specialized EET steps, which involve nearly isoenergetic pairs of chromophores which are more weakly coupled than the chromophores involved in uphill/downhill EET. Since the initial anisotropies  $r(0)$  are 0.4 within error in our PS I antennae, we see no evidence of subpicosecond depolarization. These observations are consistent with (but by no means prove) a scenario in which the antenna Chl *a* spectral forms are grouped into similar clusters, each containing a spectrally inhomogeneous set of chromophores [8]. In this “pebble mosaic” model [30], equilibration inside clusters proceeds more rapidly than EET between clusters. The zero-phonon linewidths in low temperature hole burning experiments are necessarily dominated by the fastest decay process(es) in the laser excited chromophore. It is therefore unclear whether the 300 ps decay dynamics observed at 1.6 K should correlate with the femtosecond room temperature kinetics for nonisoergic EET, or with our picosecond depolarization lifetimes.

The contrasting temperature sensitivity in the isotropic and anisotropic decay times

(Tables I and II) is striking; it reaccentuates the fact that they are caused by physically distinct processes. There are few previous reports of PS I antenna kinetics at temperatures below 77 K (and none in native PS I particles); temperatures lower than this (Table II) are required in order to reveal the strong temperature dependence in the anisotropic decay. Searle et al. [2] investigated fluorescence decays of enriched PS I particles with antenna Chl *a*/P700 ~ 40 at several temperatures between 270 and 10 K. Their decays were multiexponential at all temperatures, and they reported only the lifetimes of the principal decay component. At the fluorescence wavelengths corresponding to the core antenna pigments probed in our present 680 nm work, the temperature dependence of the (isotropic) fluorescence decay is considerably weaker than that exhibited by our anisotropic lifetimes. For example, the lifetime of their principal 690 nm decay component, 30 ps at 270 K, becomes only 57 ps at 10 K. This comparatively sluggish temperature dependence (which was evaluated with a photon counting instrument function ~ 300-400 ps wide [2]) is consistent with that of the intermediate isotropic lifetime component in Table I. The isotropic photosystem I antenna fluorescence decay is controlled by excitation trapping at the P700 reaction center as well as by EET among the core, peripheral, and internal antennae [4]. Its kinetics are therefore a composite property of the primary charge separation as well as antenna EET dynamics. In a study of persistent hole-burning in the P700 primary donor state, Gillie et al. [31] observed an extremely broad hole profile (~310 cm<sup>-1</sup> fwhm). Their spectra were consistent with large electron-phonon coupling (Huang Rhys factor ~ 4-6) in the special pair through a phonon mode with frequency ~ 35-50 cm<sup>-1</sup>. This implies that the absorption profile of the primary

donor state exhibits a homogeneous width  $S\omega$  on the order of at least  $\sim 200 \text{ cm}^{-1}$ . (This contrasts with the homogeneous width of the antenna Chl *a* spectrum,  $S_s\omega_s \sim 16 \text{ cm}^{-1}$ , vide supra.) Hence, Förster energy transfer from a donor antenna to the P700 reaction center (which controls the isotropic antenna excitation decay) is not expected to be strongly temperature dependent below 300 K on theoretical grounds. Another precedent for this situation recently arose in two hole burning studies of  $B800 \rightarrow B850$  energy transfer within the antenna complex of the purple photosynthetic bacterium *Rhodobacter sphaeroides*. Van der Laan et al. [32] observed little spectral evidence of temperature dependence in these EET dynamics between 1.2 and 30 K. In a newer hole burning experiment, Reddy and Small [33] established that the homogeneous broadening in the B850 absorption spectrum at 1.6 K is comparable to the value of  $kT$  at 300 K, so that the temperature dependence of Förster EET between the B800 and B850 chromophores in *R. sphaeroides* is predicted to be weak *a priori*.

#### Note Added in Proof

We have recently recognized that the presence of exciton coupling in the antenna can give rise to excited state absorption at wavelengths close to the static  $Q_y$  spectrum [34]. This can affect absorption difference spectra such as those reported in Figure 1. However, no satellite structure arising from exciton coupling appears in the hole burning spectra of this antenna [9].

**ACKNOWLEDGMENTS**

We are indebted to Gerald Small for many stimulating discussions and to John Golbeck for providing the PSI-200 preparation. P. A. L. was generously supported through a William E. Catron Fellowship. The Ames Laboratory is operated for the U. S. Department of Energy by Iowa State University under Contract No. W-7405-Eng-82. This work was supported by the Office of Basic Energy Sciences.

## REFERENCES

1. Golbeck, J. H. *Meth. Enzymol.* 1980, 69,129.
2. Searle, G. F. W.; Tamkivi, R.; van Hoek, A.; Schaafsma, T. J. *J. Chem. Soc. Faraday Trans. 2* 1988, 84, 315.
3. Wittmershaus, B. P.; Berns, D. S.; Huang, C. *Biophys. J.* 1987, 52, 829.
4. Mukerji, I.; Sauer, K. *Proc. C. S. French Symposium on Photosynthesis* (Palo Alto, CA, July 1988) Alan R. Liss Publishers: New York
5. Owens, T. G.; Webb, S. P.; Alberte, R. S.; Mets, L.; Fleming, G. R. *Biophys. J.* 1988, 53, 733.
6. Owens, T. G.; Webb, S. P.; Mets, L.; Alberte, R. S.; Fleming, G. R. *Biophys. J.* 1989, 56, 95.
7. Holzwarth, A. R.; Haehnel, W.; Ratajczak, R.; Bittersman, E.; Schatz, G. H. *Current Research in Photosynthesis Vol II* (Proc. VIII International Conference on Photosynthesis, Stockholm, Sweden, Aug. 6-11, 1989), Baltscheffsky, M., Ed.; p. 611.
8. Causgrove, T. P.; Yang, S.; Struve, W. S. *J. Phys. Chem.* 1989, 93, 6844.
9. Gillie, J. K.; Small, G. J.; Golbeck, J. H. *J. Phys. Chem.* 1989, 93, 1620.
10. Owens, T. G.; Webb, S. P.; Mets, L.; Alberte, R. S.; Fleming, G. R. *Proc. Natl. Acad. Sci. USA* 1987, 84,1532.
11. Pearlstein, R. M. *Photochem. Photobiol.* 1982, 35, 835.
12. Lyle, P. A.; Struve, W. S. *Photochem. Photobiol.* 1991, 53, 359
13. Causgrove, T. P.; Yang, S.; Struve, W. S. *J. Phys. Chem.* 1988, 92, 6121.
14. Sarai, A.; Yomosa, S. *Photochem. Photobiol.* 1980, 31, 579.
15. Jortner, J. *J. Chem. Phys.* 1976, 64, 4860.



16. Abramowitz, M.; Stegun, I. *Handbook of Mathematical Functions*, Dover Publications, Inc., New York, NY, 1965.
  17. Förster, Th. *Discuss. Faraday Soc.* 1959, 27, 7.
  18. Hayes, J. M.; Gillie, J. K.; Tang, D.; Small, G. J. *Biochim. Biophys. Acta* 1988, 932, 287.
  19. Mullet, J. E.; Burke, J. J.; Arntzen, C. J. *Plant Physiol.* (Bethesda) 1980, 65, 814.
  20. Anfinrud, P.; Struve, W. S. *Rev. Sci. Instrum.* 1986, 57, 380.
  21. Moog, R. S.; Kuki, A.; Fayer, M. D.; Boxer, S. G. *Biochem.* 1984, 23, 1564.
  22. Kim, Y. R.; Share, P.; Pereira, M.; Sarisky, M.; Hochstrasser, R. M. *J. Chem. Phys.* 1989, 91, 7557.
  23. (a) Causgrove, T. P.; Yang, S.; Struve, W. S. *J. Phys. Chem.* 1988, 92, 6790; (b) Lyle, P. A.; Struve, W. S. *J. Phys. Chem.* 1990, 94, 7338.
  24. Anfinrud, P. M.; Hart, D. E.; Hedstrom, J. F.; Struve, W. S. *J. Phys. Chem.* 1986, 90, 2374.
  25. Ikegami, I.; Itoh, S. *Biochim. Biophys. Acta* 1988, 934, 39.
  26. Lyle, P. A., unpublished work.
  27. Bixon, M.; Jortner, J. *J. Phys. Chem.* 1986, 90, 3795.
  28. (a) Matthews, B. W.; Fenna, R. E. *Accts. Chem. Res.* 1980, 13, 309; (b) Tronrud, D. E.; Schmid, M. E.; Matthews, B. W. *J. Mol. Biol.* 1986, 188, 443.
  29. Eads, D. D.; Todd, D.; Ruggiero, A.; Fleming, G. R. *Abstr. 198th Am. Chem. Soc. Natl. Meeting, Miami Beach, FL, September 1989* (American Chemical Society, Washington, DC 1989), Paper PHYS-19.
  30. Philipson, K. D.; Sauer, K. *Biochemistry* 1972, 11, 1880.
  31. Gillie, J. K.; Lyle, P. A.; Small, G. J.; Golbeck, J. H. *Photosynth. Res.* 1989, 22, 233.
-

32. van der Laan, H.; Schmidt, Th.; Visschers, R. W.; Visscher, K. J.; van Grondelle, R.; Völker, S. *Chem. Phys. Lett.* 1990, 170, 231.
33. Reddy, N. R. S.; Small, G. J. *Chem. Phys. Lett.* submitted.
34. Lin, S.; Amerongen, H.; Struve, W. S. *Biochim. Biophys. Acta.* submitted for publication

## SECTION CONCLUSIONS

Temperature dependent isotropic and anisotropic decays were obtained for PSI and fit with the results of Section I. The fits show that the isotropic and anisotropic decays have different temperature sensitivities and it is proposed that the difference is because they represent physically distinct processes. Hole burning results of the same system were used to guide the fitting of the temperature dependence. A localized phonon model is consistent with the time resolved and hole burning data. The results indicate that the EET is phonon assisted with a frequency of  $20\text{ cm}^{-1}$  and a coupling strength of 0.8.

The lack of temperature dependence for the isotropic decays is consistent with the fact that uphill/downhill EET occurs faster than the anisotropic decays in many systems studied and is consistent with the hole burning data from reaction centers which gives an  $S_0$  of  $200\text{ cm}^{-1}$ . The hole burning results indicate that Förster energy transfer should not be temperature sensitive. A scenario for the structure of PSI was proposed such that Chla molecules are grouped into similar clusters, each containing a full set of inhomogeneous chromophores.

## SECTION REFERENCES

1. Stryer, L. *Biochemistry*, 3rd ed.; W. H. Freeman and Co.: New York, 1987, p.530
2. Huang, C.; Berns, D. S. *Arch. Biochim. Biophys.* 1983, 220, 145
3. Golbeck, J. H. *Biochim. Biophys. Acta* 1987, 895, 167
4. Golbeck, J. H.; Bryant, D. A. In *Current Topics in Bioenergetics*, Vol. 16; Lee, C. P. Ed.; Academic Press: New York, 1991, p. 83
5. Rijgerberg, C. P.; Amesz, J.; Thielen, A. P. G. M.; Swager, J. A. *Biochim. Biophys. Acta* 1979, 545, 473
6. Wittmershaus, B. P. In *Progress in Photosynthesis Research*, Vol. I; Biggins, J., Ed.; Martinus Nijhoff: The Hague, 1987, p. 75
7. Maggiora, L. L.; Maggiora, G. M. *Photochem. Photobiol.* 1984, 39, 847
8. Gregory, R. P. F. In *Photosynthesis*; Chapman and Hall: New York, Chpt. 2
9. Matthews, B. W.; Fenna, R. E. *Acc. Chem. Res.* 1980, 13, 309
10. Lyon, M. K.; Unwin, P. N. T. *Photochem. Photobiol.* 1988, 47, 30S (Abstracts of the 16th Annual Meeting for the American Society for Photobiology, March 13-17, 1988)
11. Schirmer, T.; Bode, W.; Huber, R.; Sidler, W.; Zuber, H. *J. Mol. Biol.* 1985, 184, 257
12. Causgrove, T. P.; Yang, S.; Struve, W. S. *J. Phys. Chem.* 1988, 92, 6121
13. Causgrove, T. P.; Yang, S.; Struve, W. S. *J. Phys. Chem.* 1989, 93, 6844
14. Owens, T. G.; Webb, S. P.; Mets, L.; Alberty, R. S.; Fleming, G. R. *Proc. Natl. Acad. Sci. USA* 1987, 84, 1532
15. Sauer, K. In *Bioenergetics of Photosynthesis*; Govindjee, Ed.; Academic Press: New York, 1975
16. Werst, M.; Jia, Y.; Mets, L.; Fleming, G. R. *Biophys. J.* 1992, in press

17. Jia, Y.; Jean, J. M.; Werst, M. M.; Chan, C. -K.; Fleming, G. R. submitted for publication
18. Gillie, J. K.; Small, G. J. *J. Phys. Chem.* 1989, 93, 1620
19. Page, J. B.; Chan, C. K. *J. Chem. Phys.* 1983, 75, 5234
20. Jean, J.; Chan, C. -K.; Fleming, G. R.; Owens, T. G. *Biophys. J.* 1989, 56, 1203
21. Hunter, C. N.; Bergström, H.; van Grandelle, R.; Sundström, V. *Biochem.* 1990, 29, 3203
22. van Grondelle, R.; Bergström, H.; Sundström, V.; van Dorssen, J.; Vos, M.; Hunter, C. N. In *Photosynthetic Light-Harvesting Systems*; Scheer, H., Schneider, S. Eds.; Walter de Gruyter: New York, p. 519
23. Ford, R. C.; Picot, D.; Garavito, P. M. *EMBO J.* 1987, 6, 1581
24. Witt, I.; Witt, H. T.; Di Fiore, D.; Rögner, M.; Hinrichs, W.; Saeger, W.; Granzin, J.; Betzel, Ch.; Dauter, Z. *Ber. Bunes. Phys. Chem.* 1988, 92, 1503
25. Bottcher, B.; Graber, P.; Boekema, E. J. *Biochimica. Biophysica. Acta* 1992, 1100, 125
26. Witt, I.; Witt, H. T.; Gerken, S.; Sängner, W.; Dekkar, J. P.; Rögner, M. *FEBS Lett.* 1987, 221, 260
27. Shoham, G.; Michaeli, D.; Nechushtai, R. *Physiol. Plant.* 1989, 76, A82
28. Lin, S.; van Amerongen, H.; Struve, W. S. submitted 1992
29. Atkins, P. W. *Molecular Quantum Mechanics*, 2nd Edn.; Oxford University Press: New York, 1984, p.198
30. Herzberg, G. *Molecular Spectra and Molecular Structure I. Spectra of Diatomic Molecules*; Van Nostrand Reinhold Company: New York, p. 73
31. DeVault, D. *Quantum-Mechanical Tunneling in Biological Systems*, 2nd Edn.; Cambridge University Press: New York, 1984
32. The derivation from this point to equation 19 closely follows that given by Devault (reference 31).

33. Bolton, J. R.; Archer, M. D. In *Electron Transfer in Inorganic, Organic, and Biological Systems*; Bolton, J. R., Mataga, N., McLendon, G. Eds.; American Chemical Society: Washington, 1991, p. 267
34. Beitz, J. V.; Miller, J. R. *J. Chem. Phys.* 1979, 71, 4579
35. Miller, J. R.; Beitz, J. V.; Huddleston, R. K. *J. Am. Chem. Soc.* 1984, 106, 5057
36. Miller, J. R.; Calcaterra, L. T.; Closs, G. L. *J. Am. Chem. Soc.* 1984, 106, 3047
37. Gould, I. R.; Ege, D.; Mattes, S. L.; Farid, S. *J. Am. Chem. Soc.* 1987, 109, 3794
38. Levin, P. P.; Pluzhnikov, P. F.; Kuzmin, V. A. *Chem. Phys. Lett.* 1988, 110, 1991
39. Vauthey, E.; Suppan, P.; Haselbach, E. *Helv. Chim. Acta* 1988, 71, 93
40. Jortner, J. *J. Chem. Phys.* 1976, 64, 4860
41. Abramowitz, M; Stegun, I. *Handbook of Mathematical Functions*; Dover Publications: New York, 1965

SECTION III.

HOLE BURNING STUDIES OF REACTION  
CENTER COMPLEXES FROM PURPLE BACTERIA

---

## INTRODUCTION

### Bacterial Reaction Centers

Knowledge of the electron transfer process in bacterial reaction centers has increased significantly since the structural determination of the reaction center complex for *Rp. viridis* [1,2,3] and *Rb. sphaeroides* [4,5,6]. Information about the spatial arrangement of the cofactors involved in the electron transfer process has enabled detailed theoretical investigations of the energy interactions of the chromophores as well as calculations of the transfer rate. However, even with all the activity directed towards the problem a number of questions still remain. Why does the electron only travel down one side of the reaction center? How does the accessory bacteriochlorophyll molecule interact with the electron transfer process? What causes the unique temperature dependence of the initial electron transfer step?

One puzzle of the electron separation process is the occurrence of electron transfer down only one arm of the reaction center [7]. Numerous amino acid differences occur in the proteins around the two arms which causes significant deviations from C-2 symmetry [8,9]. Thompson and Zerner have reported INDO/S calculations for *Rp. viridis* with and without the inclusion of the protein [10]. For both calculations they found that electron transfer down the L branch was favored over the M branch based on energetic differences between the two branches. The energetic differences are caused by small structural deviations

---



around the chromophores which breaks the C-2 symmetry. With the development of a new technique called site-specific mutagenesis, it has become possible to explore and try to determine which structural differences are important in determining the electron transfer pathway and rate [11,12]. Site-specific mutagenesis is used to alter specific amino acid residues of the reaction center protein that are in close proximity to any of the chromophores. After each change the charge transfer kinetics can be measured and evidence for electron transfer down the opposite arm sought. Table I shows some of the amino acid changes and the experimental kinetic results. To date no specific change has allowed for electron transfer down the M branch though the electron transfer has been slowed considerably in some cases and possibly even increased slightly in one case.

Another problem that is attracting a lot of attention is how the accessory bacteriochlorophyll molecule interacts in the electron transfer [13]. Two models have been proposed, the two step sequential [14,15] and the super-exchange models [16,17]. The two step sequential model supposes that the accessory bacteriochlorophyll molecule is a real intermediate and that the rate limiting step is electron transfer to the bacteriochlorophyll, whereas electron transfer from the bacteriochlorophyll to the bacteriopheophytin is ultrafast. Experimentally it would be difficult to find any noticeable bleaching of the accessory bacteriochlorophyll band as the electron would not reside on the bacteriochlorophyll long enough to build up population. The super-exchange model supposes that the accessory bacteriochlorophyll is not a real intermediate but couples to the special pair and bacteriopheophytin molecules to expedite the electron transfer. Since the super-exchange

**Table I**  
**Stimulated Emission Decay Time Constants**  
**For Several *Rb. capsulatus* Mutants**

	T (K)	%A1	$t_1$ (ps)	%A2	$t_2$
YL	296	100	$2.1 \pm 0.3$		
	140	100	$1.6 \pm 0.2$		
	17	100	$1.3 \pm 0.2$		
YF	298	65	$3.5 \pm 0.3$	35	$11 \pm 2$
	200	74	$2.9 \pm 0.3$	26	$14 \pm 4$
	77	56	$2.1 \pm 0.3$	44	$9 \pm 2$
	17	70	$2.4 \pm 0.3$	30	$13 \pm 3$
FM	296	80	$9.2 \pm 1.5$	20	$126 \pm 50$
	17	58	$6.4 \pm 1.0$	42	$72 \pm 30$
HM	298	100	$3.7 \pm 0.4$		
	200	100	$3.0 \pm 0.3$		
	140	100	$3.1 \pm 0.3$		
	77	100	$2.6 \pm 0.4$		
	17	100	$2.6 \pm 0.4$		
TM	296	100	$15 \pm 3$		
	200	83	$27 \pm 4$	17	$2.6 \pm 2$
	77	100	$26 \pm 4$		
	17	100	$26 \pm 5$		

model does not allow for the electron to reside on the accessory bacteriochlorophyll molecule for any length of time unambiguous evidence for the bleaching of the bacteriochlorophyll band could rule this mechanism out. Many theoretical attempts have also been made to explain which of these two mechanisms could be operable [18,19,20]. Bixon et. al. [21] proposed that at room temperature the two step mechanism dominates while at low temperature super-exchange prevails. This possibility could then help to explain why Holzapfel et al.'s [22,15] experiments at room temperature indicated the two-step mechanism while Fleming et. al.'s experiments [23,24] at low temperature indicated the super-exchange mechanism. Recently Alden et. al. [25] has presented calculations for several mutants of *Rhodobacter capsulatus* that indicate a switch between these two mechanisms can occur when the energy of the accessory bacteriochlorophyll molecule changes upon mutation.

The last aspect of the electron transfer in bacterial reaction centers is their temperature dependence. Most of the electron transfer processes of bacterial reaction centers (both forward and backward) are temperature independent or slightly temperature sensitive over a broad range of temperatures [24,26,27]. Thus, no apparent activation energy is required for these processes. Non-adiabatic electron transfer theory has been used under the condition that the energy gap and the reorganization energy are equal to explain the small dependence of rate on temperature. The activationless condition results in a slight inverse temperature dependence and therefore matches the experimental trend. However, in its simplest form (i.e. one mode) the activationless condition cannot explain all of the observed temperature

dependencies. In *Rp. viridis*, for example, the rate changes far more with temperature than expected between 200 K and room temperature. As discussed in the General Introduction, protein contractions, temperature dependence of the energy gap, and the inclusion of multimodes have all been invoked to explain *Rp. viridis*' temperature dependence. Another possibility that was not addressed is the possibility that the inhomogeneous distribution of reaction centers could play a role. Kirmaier and Holten [28] have proposed that as the temperature is lowered the electron transfer becomes favored in those reaction centers which have the fastest rates. Experimentally, there proposal was formulated from the observation that a distribution of rates from 1 to 4 ps was found for different excitation wavelengths. Upon cooling, the reaction center distribution would shift towards the wavelengths of faster electron transfer, causing a slight negative temperature dependence.

In the present work, hole burning was used to explore the vibrational coupling, reaction rates at low temperature, and homogeneous and inhomogeneous contributions to the absorption spectra for the special pair band of the  $Q_y$  absorption band. Earlier studies [29,30,31,32] have shown that a broad hole is produced indicating strong vibrational coupling, that a large homogeneous contribution to the band exists, that the electron transfer time at low temperatures agrees well with the transfer times found in picosecond transient absorption experiments, and that there exists a vibrational "marker mode" near  $120\text{ cm}^{-1}$  associated with the special pair. For the most part these findings come out of a linear electron-phonon coupling theory developed by Hayes and Small [33] used to simulate the experimental hole profiles obtained. In the next part of this introduction a slightly modified

derivation of their single-site absorption profile equation will be given that more closely follows the derivation used for the multi-phonon theory in section II.

### Hole Burning Theory

The derivation starts with equation 24 of the introduction to section II.

$$W = A \int dt e^{\left[ -\sum_k S_k (2\bar{n}_k + 1) \right]} \prod_{k=1}^N \sum_{R=0}^{\infty} \sum_{T=0}^R \frac{[S_k(\bar{n}_k + 1)]^{R-T} (S_k \bar{n}_k)^T}{(R-T)! T!} \times \exp[-i\Delta Et/\hbar + i\omega_k(R-T)t - i\omega_k Tt] \quad (1)$$

The only change required to derive the hole burning single-site absorption line shape is that the energy gap is now for an optical transition. In this case the energy gap is equal to  $\hbar\nu$  and equation (1) can be rewritten as:

$$W = A \int dt e^{\left[ -\sum_k S_k (2\bar{n}_k + 1) \right]} \prod_{k=1}^N \sum_{R=0}^{\infty} \sum_{T=0}^R \frac{[S_k(\bar{n}_k + 1)]^{R-T} (S_k \bar{n}_k)^T}{(R-T)! T!} \times \exp[-i\nu t + i\omega_k(R-T)t - i\omega_k Tt] \quad (2)$$

which when integrated over  $t$  gives:

$$W = A e^{\left[ -\sum_k S_k (2\bar{n}_k + 1) \right]} \prod_{k=1}^N \sum_{R=0}^{\infty} \sum_{T=0}^R \frac{[S_k(\bar{n}_k + 1)]^{R-T} (S_k \bar{n}_k)^T}{(R-T)! T!} \times \delta(-\nu + \sum_k \omega_k [R-2T]) \quad (3)$$

When the temperature approaches zero, equation (3) can be written for two modes as:

$$W = A \left[ \sum_{R=0}^{\infty} \frac{e^{-S_1} S_1^R}{R!} \right] \left[ \sum_{J=0}^{\infty} \frac{e^{-S_2} S_2^J}{J!} \right] \delta(\nu - R\omega_1 - J\omega_2) \quad (4)$$

Equation (4) can be compared to the single site line shape used to model the transient hole burning data of Johnson et. al. [34] and a line shape can be written from equation (3):

$$G(\Omega - \nu) = e^{\left[ -\sum_k S_k (2\bar{n}_k + 1) \right]} \prod_{k=1}^N \sum_{R=0}^{\infty} \sum_{T=0}^R \frac{[S_k (\bar{n}_k + 1)]^{R-T} [S_k \bar{n}_k]^T}{(R-T)! T!} \times \delta(\Omega - \nu + \sum_k \omega_k [R - 2T]) \quad (5)$$

where a calculatable line shape can be obtained by substituting an appropriate continuous function in place of the delta function. The single site lineshape given in equation (5) differs from Johnson et. al.'s in that their lineshape was only for the case where the temperature equals zero kelvin. Equation (5) is good for any finite temperature. However, unless the temperature that the hole spectrum was obtained is greater than about 8 K (for coupling to a mode of 20 cm<sup>-1</sup>), the difference between the low temperature line shape and equation (5) is quite negligible. Above 8 K, three changes to the low temperature hole spectra can be observed. Figure 1 shows hole spectra taken from 1.8 to 16 K normalized at the zero phonon hole (ZPH) position. At 1.8, 4.2, and 8 K little change has occurred. At higher temperatures, however, the phonon side band on the high energy side begins to dominate the spectra and

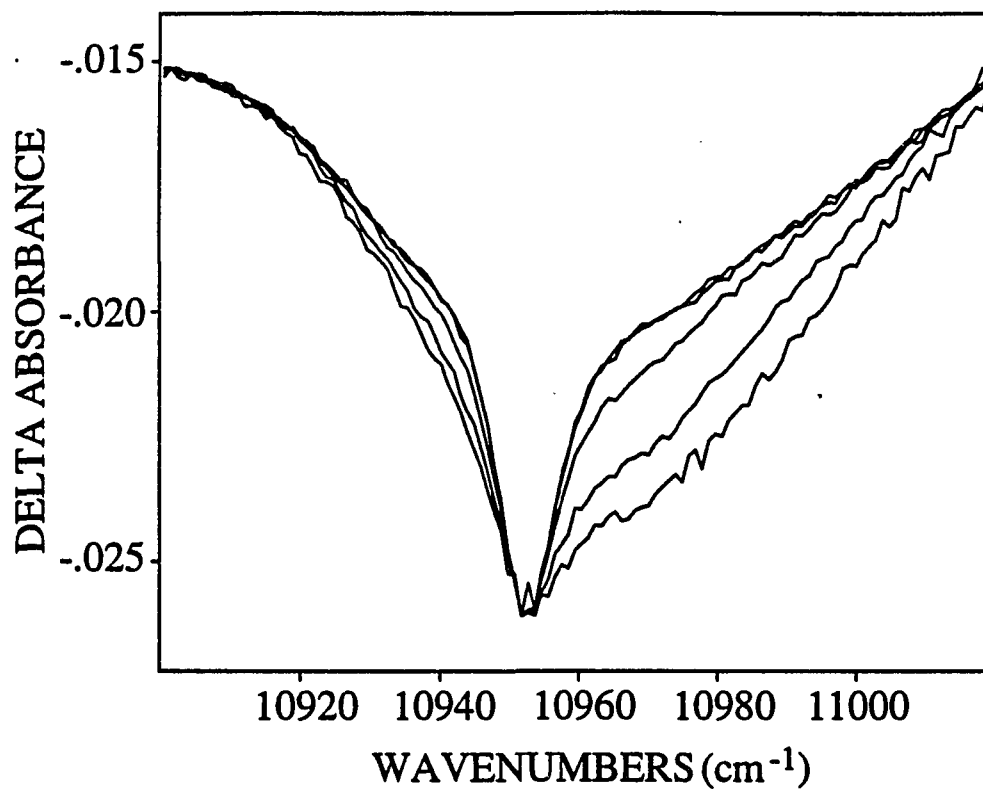


**Figure 1.** Spectra showing the increase of phonon absorption and emission processes with increasing temperature. The temperatures from top to bottom are: 1.8, 4.2, 8, 12, and 16 K. The spectra are normalized at the ZPH position

on the low energy side a smaller deviation is also evident. From equation (5), the phonon absorption process is  $(\bar{n}_k+1)$  and phonon emission  $\bar{n}$ . At 12 K  $\bar{n}$  is equal to .1 for a  $20\text{cm}^{-1}$  mode. Therefore, at 12 K phonon absorption dominates over emission processes. The temperature would have to be increased to greater than 100 K for the emission process to begin to approach the absorption process in intensity. The third change that occurs at higher temperatures is illustrated in Figure 2. This figure is the same as Figure 1 except that hole spectra are shown unnormalized. As the temperature increases, the ZPH loses intensity in a fairly monotonic fashion. By 16 K the ZPH is barely detectable, and at 20 K (not shown) was indistinguishable from the background. Equation (5) shows that the weight given to the zero-phonon process ( $R=0$ ,  $T=0$ ) is  $\exp[-\sum S_k(2\bar{n}+1)]$ . As the temperature increases, the effective Huang Rhys factor ( $S$ ) increases, and the zero phonon intensity decreases. For example, if the low temperature Huang Rhys factor is 2 (this value has been determined for the low frequency mode of Figures 1 and 2), the weight given to the zero phonon process is 0.14. By 12 K the weight has dropped to 0.09, and at 20 K to 0.04.

All that remains is to derive the width relationship between the  $R$  and  $T$  sums for each phonon process. This can be done by redefining Figure 4 of the introduction of Section II. For a zero phonon process  $R=0$  and  $T=0$  which leads to  $\delta(\Omega-\nu)$  meaning that the zero phonon process is centered at  $\Omega=\nu$ . For a one phonon process  $R=1$  and  $T=0$  and 1 which gives  $\delta(\Omega-\nu-\omega_k)$  and  $\delta(\Omega-\nu+\omega_k)$ . Therefore a similar diagram could be constructed with the 1, 2, 3 etc. replaced by  $1\omega_k$ ,  $2\omega_k$ ,  $3\omega_k$  etc. From the previous discussion it was shown that the 2, 3, 4 etc. phonon processes are built up of one phonon processes (i.e. for a 3 phonon process there



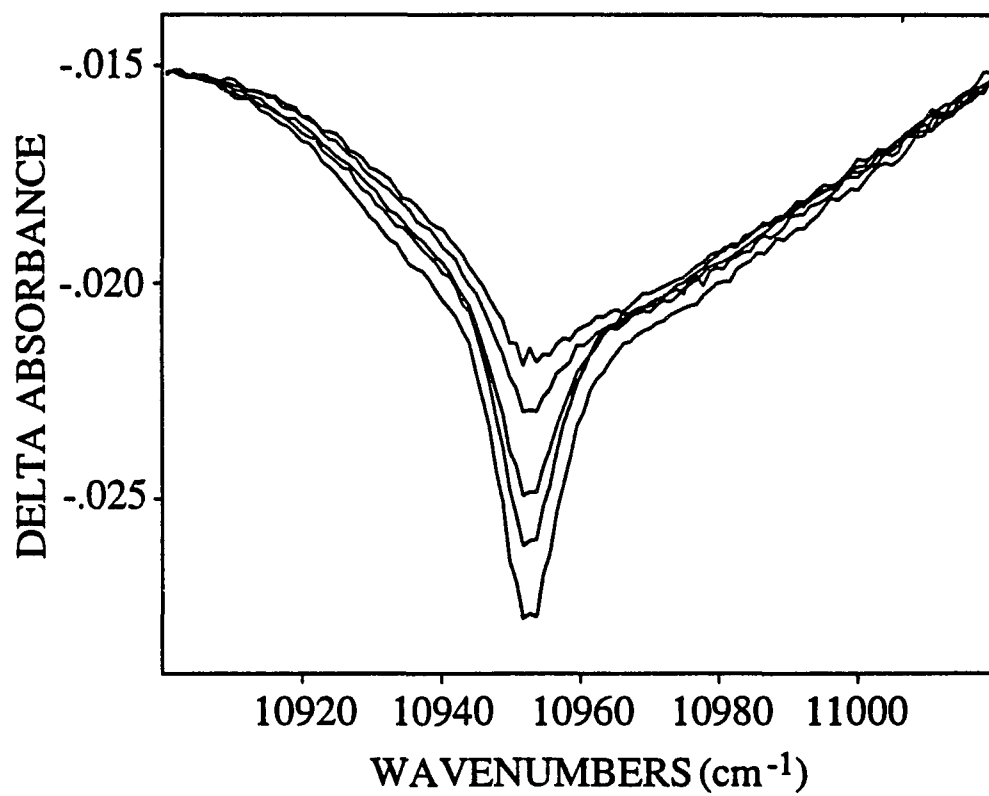


**Figure 2.** Same spectra as in Figure 1, but shown on the same intensity scale. The temperatures are increasing from bottom to top

could be 3 one phonon emissions or absorptions, 2 one phonon absorptions and one phonon emission, or a one phonon absorption and 2 phonon emissions). Mathematically, the phonon processes greater than a one phonon process are R-fold convolutions of the one phonon process. Referring to Figure 3, the convolution of the lineshape function which represents the one phonon absorption process is shown in parts a, b and c by the solid curves. The dotted curve is also the one phonon line shape function, but is shown being displaced from right to left in a, b, and c. Only when the curves overlap with each other does the new function have any intensity. Therefore, the two phonon lineshape function is composed of the three parts shown in d.

The convolution of two functions is written [35]:

$$f \cdot g = \frac{1}{\sqrt{2\pi}} \int_{-\infty}^{\infty} g(y) f(x-y) dy \quad (6)$$

where  $y$  can take on any value between  $-\infty$  and  $\infty$ , and the new function is calculated at each of these  $y$  points. If a functional form is chosen to represent the line shape for a one phonon process then the relationship between the widths of the 1-,2-,3-,... phonon processes can be determined.

Two functional forms are normally used, gaussian or lorentzian. The use of either one of these functions eventually leads to an analytical form for the hole spectrum [33,36] in the short burn time limit. For the long burn time limit no analytical form can be found and

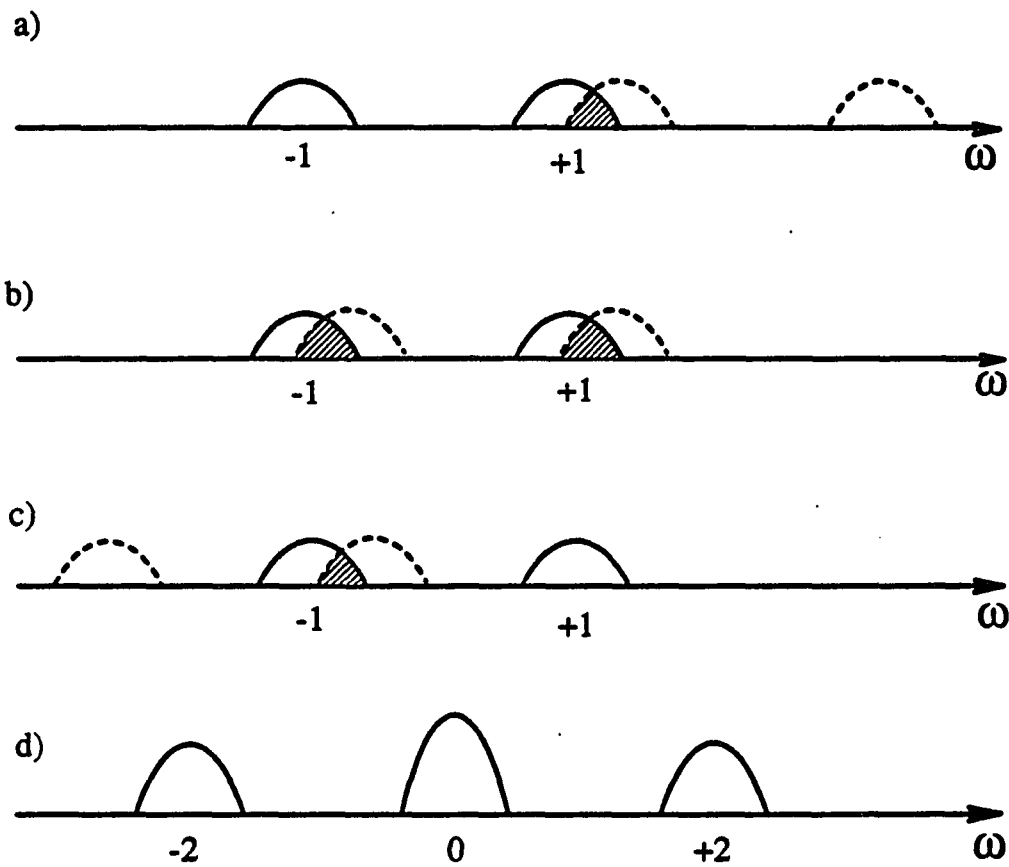


**Figure 3.** Diagram showing the convolution process for creating the two phonon process from the one phonon process. a, b, and c show the process from right to left, and d shows the two phonon process

thus, a more complex function may be used [34]. The convolution of the one phonon gaussian lineshape written to derive the two phonon lineshape is:

$$\frac{B}{\sqrt{2\pi}} \int d\omega' [\exp(-[\Omega - \omega - \omega']^2/\sigma^2) + \exp(-[\Omega + \omega - \omega']^2/\sigma^2)] \quad (7)$$

$$\times [\exp(-[\omega' - \omega]^2/\sigma^2) + \exp(-[\omega' + \omega]^2/\sigma^2)]$$

where B is a normalization term. By Fourier transforming the gaussian functions we can exploit one relationship of convolutions which is:

$$\int_{-\infty}^{\infty} g(y) f(x-y) dy = \int_{-\infty}^{\infty} F(t) G(t) e^{-ity} dt \quad (8)$$

Equation (8) shows that the convolution of two functions is the inverse fourier transform of the product of the fourier transforms of the original functions. The fourier transform of a gaussian is [37]:

$$\mathcal{F}[\exp(-P(y-b)^2)] = a \exp(-a\alpha^2/4) e^{-i\alpha b} \quad (9)$$

Applying equation 9 to equation 7, the width relationship between the one and two phonon process can be obtained:

$$\frac{B}{\sqrt{2\pi}} \exp(-(\Omega - 2\omega)^2/2\sigma_a^2) \quad (10)$$

where  $\sigma_a = (\sigma^2 + \sigma^2)^{1/2} = 2^{1/2}\sigma$ . Extension to three or more phonon processes would confirm

that the width increases as  $r^{1/2}$ . Equation 10 is one of four terms that are obtained when equation 9 is applied to equation 7. The existence of four terms is also evident from Figure 3. Part a shows the formation of the two phonon absorption, part b the formation of two terms corresponding to the one phonon emission plus one phonon absorption (zero phonon) process, and part c the two phonon emission term.

To obtain the hole spectrum, the usual method is followed [33]. The single site profile (equation (5) with the delta function replaced by either a gaussian, a lorentzian, or a combination of these two) is convolved with a gaussian zero-phonon site excitation function centered at  $\nu_m$  with a full width at half maximum of  $\Gamma_1 (N_o(\nu-\nu_m)/N)$  to give the absorption spectrum:

$$A_o = \int d\nu N_o(\nu-\nu_m) L(\Omega-\nu) \quad (11)$$

The spectrum after burning is formed by multiplying the site excitation function with  $N_o(\nu-\nu_m) \exp[\sigma I \phi \tau L(\omega_B-\nu)]$ , where  $\sigma$  is the absorption cross section and  $\phi$  the hole burning quantum yield, which gives the number of sites remaining at frequency  $\nu$ . The burn spectrum is then given by:

$$A_\tau = \int d\nu N_o(\nu-\nu_m) \exp[\sigma I \phi \tau L(\omega_B-\nu)] L(\Omega-\nu) \quad (12)$$

The difference of equations (11) and (12) can then be used to simulate experimental hole spectra.

PAPER I. HIGH RESOLUTION SIGNAL TO NOISE  
PHOTOCHEMICAL HOLE-BURNED  
SPECTRA OF PROTONATED AND  
DEUTERATED REACTION CENTERS OF  
*RHODOBACTER SPHAEROIDES*

**High Resolution Signal to Noise Photochemical  
Hole-Burned Spectra of Protonated and Deuterated  
Reaction Centers of *Rhodobacter Sphaeroides***

**P. A. Lyle, S. V. Kolaczowski, G. J. Small**

## INTRODUCTION

The structure that underlies the broad ( $\sim 100\text{-}500\text{ cm}^{-1}$  at 4.2 K) absorption profiles of the photocatalytic excited state ( $Q_y$ ) of chlorophylls and pheophytins is relevant to the energy- and electron-transfer dynamics of photosynthetic units, e.g., temperature dependence, dispersive kinetics, coherence effects. Spectral hole burning has proven to be an important and versatile tool for the determination of such structure (for recent reviews see 1-3). The burn-wavelength dependence of the hole profile yields the magnitudes of the site inhomogeneous broadening ( $\Gamma_I$ ) and homogeneous broadening ( $\Gamma_H$ ) contributions to the  $Q_y$  absorption profile. Studies of many protein complexes have yielded  $\Gamma_I \sim 50\text{-}200\text{ cm}^{-1}$ , depending on the complex and  $Q_y$ -band. Given the normal glass-like heterogeneity of the protein [4,5], most of  $\Gamma_I$  is intrinsic, rather than solvent- or detergent-induced. That is, it is the existence of a large number of conformational substates of the protein [6] that leads to a broad distribution of transition frequencies. An important contributor to  $\Gamma_H$  is the linear electron-phonon coupling ( $\Gamma_{ep}$ ). Based on hole burning studies on complexes of purple bacteria, cyanobacteria, green algae and photosystem I and II of green plants it is clear that coupling to a broad distribution of protein phonons with a mean frequency of  $\omega_m = 20\text{-}30\text{ cm}^{-1}$  is ubiquitous [2,3]. Furthermore, the coupling strength is weak ( $S < 1$ ) for antenna chlorophylls and moderately strong ( $S \sim 2$ ) for the special pair or primary donor state of reaction centers. Although not pertinent to this paper we note, for completeness, that for antenna protein complexes characterized by structural subunits containing strongly exciton-



coupled Chls, the contribution to  $\Gamma_H$  from exciton level structure/ultra-fast inter-exciton level relaxation can be very significant [7-11].

In this paper we present photochemical hole burned spectra of the bacteriochlorophyll (BChl) special pair or primary donor state  $Q_y$ -band, P870, of *Rhodobacter sphaeroides*. The results were obtained with a new apparatus that has resulted in a 20-fold improvement in S/N ratio relative to previously reported spectra from this laboratory [12-16]. The main objectives of our studies were to further test certain assumptions and the values of the theoretical parameters used in previous work and simulations [17] of the hole spectra and to generate data pertinent to the question of dispersive kinetics for the primary charge-separation process [18,19].

Our earlier studies, which are reviewed in [2], established that the absorption transition to P870\* (asterisk denoting lowest excited  $Q_y$ -dimer state of the special pair, i.e., the primary electron-donor state) couples quite strongly to a  $\sim 120\text{ cm}^{-1}$  mode with an S-value of 1.5. This mode was assigned [17] as an intermolecular mode of the special pair since the largest S-value for the intramolecular modes of Chl monomers is  $\sim 0.05$  [8,20]. In the uppermost row of Table I the frequency and S-value are denoted as  $\omega_{sp}$  and  $S_{sp}$  ( $sp \equiv$  special pair intermolecular "marker" mode). For the protein phonons,  $\omega_m = 30\text{ cm}^{-1}$  and  $S = 2.2$ . The values for P960\*, the analogous state for *Rhodospseudomonas viridis*, are given in the second row of Table I. Some of the dynamical implications of these results are reviewed in reference [2]. For example, it was argued that, along with the  $\sim 30\text{ cm}^{-1}$  phonons, the marker mode should be an important contributor to the reorganization energy associated with the

Table I. Structure of P870 and P960.<sup>a,b</sup>

	$\omega_{sp}/S_{sp}^c$	$\omega_m/S$	$\Gamma$	$\Gamma_I$	$\nu_m$
P960	135/1.1	25/2.1	40	120	9799
P870	115/1.5	30/2.2	30	170	11013

<sup>a</sup>From ref. 16.

<sup>b</sup>Units of  $\omega_{sp}$ ,  $\omega_m$ ,  $\Gamma$ ,  $\Gamma_I$  and  $\nu_m$  are in  $\text{cm}^{-1}$ .

<sup>c</sup>Homogeneous width of the ZPL for the marker mode level  $\omega_{sp}^1$  is  $50 \text{ cm}^{-1}$  and  $j$  ( $50 \text{ cm}^{-1}$ ) for the  $\omega_{sp}^j$  ( $j \geq 2$ ) levels.

<sup>d</sup>One-phonon profile on low and high energy sides is a Gaussian and Lorentzian, respectively, cf. ref. 16.

initial phase of charge separation as well as the temperature dependence [21] of this separation. On the other hand, it was suggested that the marker mode is not a promoting mode for charge separation since, if it were, it would lead to a  $\coth(\hbar\omega_{sp}/2kT)$  dependence for the kinetics, in sharp contrast to the findings that [21,22] the kinetics for *Rb. sphaeroides* and *Rps. viridis* speed up by a factor of 2 and 4 as the temperature is reduced from room temperature to 10 K. Another finding was that [14-16] the zero-phonon hole (ZPH) widths of P870 and P960 yielded P870\* and P960\* decay times equal, within experimental uncertainty ( $\pm 0.2$  ps), to those measured in the time domain in the low temperature limit [21,22]. This is important because the ZPH measures decay from the total zero-point level of P\*, whereas, in the time domain measurements it is the marker and phonon modes that are predominantly initially excited. The agreement in the decay rates indicates that thermalization of the relevant low frequency modes precedes charge separation, an assumption in most of the widely used electron-transfer theories [23].

Until recently [18], the data from hole burning had not been used to theoretically address any facet of charge separation. Hayes et al. simplified the usual nonadiabatic expression for the electron-transfer rate to a form valid in the strong electron-phonon coupling limit. As a result, they were able to study the effect of a distribution of values (stemming from normal glass-like structural heterogeneity) for the relevant P\* charge separated state energy gap on the temperature dependence of primary charge separation. Their work also examined whether or not the distribution was sufficiently broad, relative to the "homogeneous width" of the phonon-nuclear factor associated with electron-phonon coupling, to yield P\* decay kinetics

sufficiently dispersive to account for the non-exponential kinetics recently reported for P870\* at room temperature [24-29]. With regard to the last question they concluded that it was not. It was suggested that perhaps a distribution of values for the pure electronic coupling matrix element  $V$  is responsible for the nonexponentiality.

This suggestion is investigated in this paper by means of experimental results that establish, for the first time, whether there is a dependence of the P870\* lifetime on the burn laser frequency as it is tuned through the inhomogeneous distribution of P870 zero-phonon line absorption transition frequencies. The superior quality of the hole spectra allow us to also study in greater detail the underlying structure of P870.

## EXPERIMENTAL

Samples of deuterated wild type *Rb. sphaeroides* were prepared for the hole burning experiments by diluting the reaction centers (RCs) into a glycerol:water glass forming solvent along with 0.1% (w/v) LDAO (lauryldimethylamine-N-oxide), 20 mM Tris/HCl pH 8.0, and 250  $\mu$ M ascorbate. Protonated R-26 *Rb. sphaeroides* RCs were also dissolved in glycerol:water, but with 0.05% Triton X-100 and 20 mM Tris/HCL pH 8.0. UQ<sub>2</sub> (2,3-dimethoxy-5-decyl-benzoquinone), 40  $\mu$ m, was added to the protonated RCs to refill any of the Q<sub>a</sub> sites left vacant in the isolation procedure. For both samples the room temperature reversible bleaching of the P870 band was used to indicate the extent of the Q<sub>a</sub> sites being filled. The photochemical bottleneck state is P<sup>+</sup>Q<sup>-</sup> (Q  $\equiv$  quinone) which relaxes back to PQ in  $\sim$ 10 ms at 4.2 K. The optical density (OD) of the samples in this study was typically 0.25-0.4 at 870 nm.

Burn irradiation (linewidth = 0.03 cm<sup>-1</sup>) was provided by a Coherent 899 Ti:Sapphire CW ring laser pumped by 15 W of the visible multiline output of a Coherent Innova AR<sup>+</sup>-laser. Typical output at 870 nm was 200 mW/cm<sup>2</sup>, which was reduced to 10 mW/cm<sup>2</sup> with a variable neutral density filter to keep bleaching of the P870 band maximum at 4.2 K below 20%. Bleaching of up to 60% was possible with higher intensities.

Absorption and photochemical hole burned spectra over the range 24,000-8,750 cm<sup>-1</sup> were taken at 2 cm<sup>-1</sup> resolution with a Bruker IFS 120 high resolution Fourier Transform (FT) spectrometer. Hole spectra are defined as the difference in absorbance with the burn laser

on and off. The signal to noise ratio (S/N) of the hole spectra has increased 20-fold over previous spectra from this group primarily due to the FT spectrometer, scan averaging for ~8 minutes (200 scans), and with the use of improved sample handling techniques. Only glasses of very high quality were used in order to avoid interference of scattered laser light (which passes through the interferometer before impinging on the detector) with the zero-phonon hole (ZPH) of the hole spectra.

As emphasized in our earlier work [12-16], utilization of high quality RC samples and judiciously chosen host media/detergents, which minimize the site inhomogeneous broadening of the P-band, yield the most structured hole spectra. Typical 4.2 K absorption spectra for the protonated and deuterated RC samples used in the present study are shown in Figure 1. The FWHM of P870 is 437 and 420  $\text{cm}^{-1}$ , respectively; about 40  $\text{cm}^{-1}$  sharper than in the highest quality spectra previously reported.

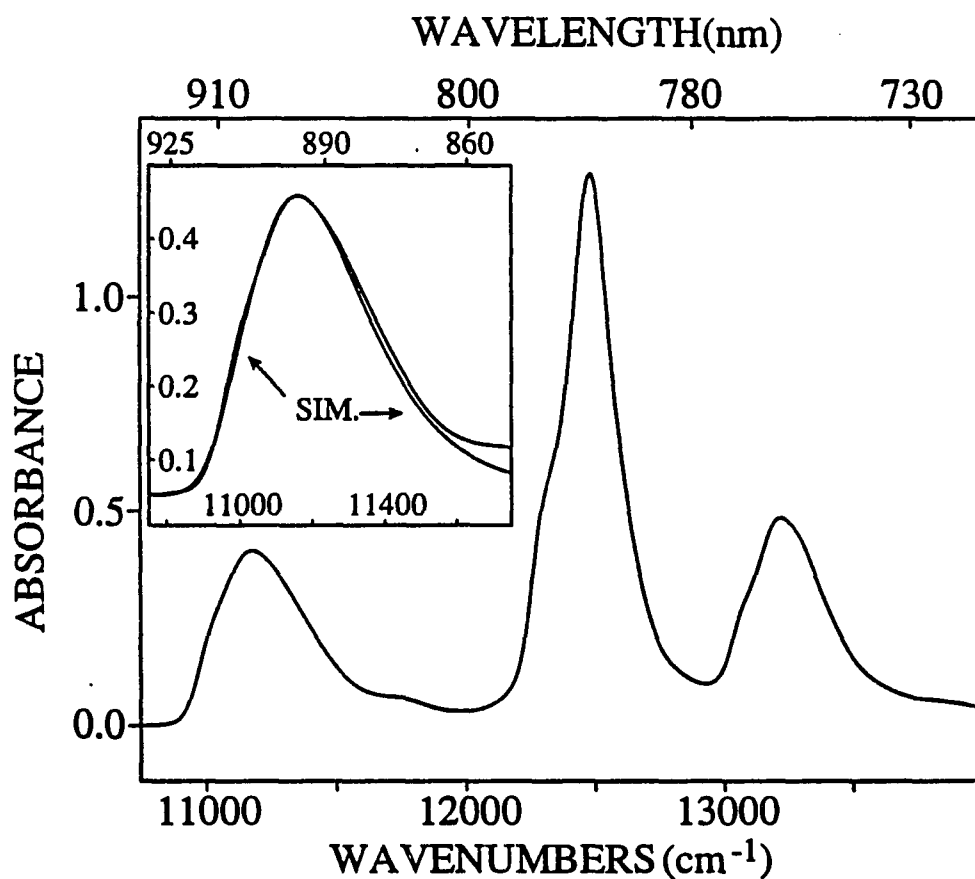


**Figure 1A.** 4.2 K absorption spectrum of the  $Q_y$ -region of deuterated RC of *Rb. sphaeroides* (wild type, strain 2.4.1). Inset shows simulation of P870 (FWHM = 420  $\text{cm}^{-1}$ ) with parameter values listed in Table II

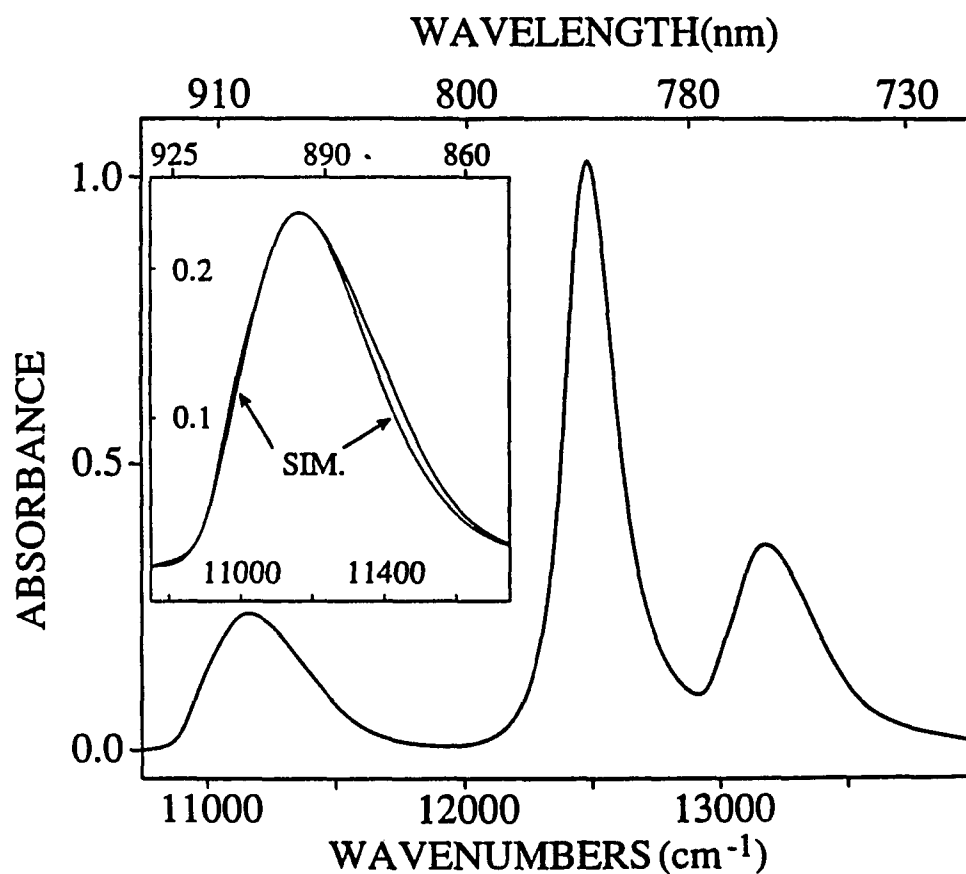


**Figure 1B.** 4.2 K absorption spectrum of the  $Q_y$ -region of protonated RC of *Rb. sphaeroides* (R-26 strain). Inset shows simulation of P870 ( $\text{FWHM} = 437 \text{ cm}^{-1}$ ) with parameter values listed in Table II.



## THEORY OF THE HOLE PROFILE

The theory of Hayes and Small [28,29] (the essential physics of the theory of Won and Friesner [30,31] is identical), which we employ, has been reviewed several times [1-3]. In reference 2, a non-mathematical discussion of the underlying physics and spectroscopy is given along with model calculations, which illustrate how the single site absorption profile and site heterogeneity are related to the hole profile. We give here only a brief account of the theory valid in the low temperature limit. A hole profile expression valid for all temperatures has recently been derived by Lyle [32].

The absorption profile of a single site with a ZPL frequency of  $\nu$  can be written as

$$L(\Omega - \nu) = \prod_{j=1}^N \left[ \sum_{r_j=0}^{\infty} \frac{e^{-S_j} S_j^{r_j}}{r_j!} \right] \sum_{r=0}^{\infty} \frac{e^{-S} S^r}{r!} \quad (1)$$

$$\times \ell \left( \Omega - \nu - r\omega_m - \sum_{j=1}^N r_j \omega_j \right)$$

where  $j$  runs over the discrete pseudo-localized or localized phonons [33] and, if necessary, the intramolecular Chl modes.  $S_j$  and  $\omega_j$  are the Huang-Rhys factor and frequency for the  $j$ th mode. The sum over  $r$  is isolated because it is meant to represent the contribution from the essentially continuous distribution of low frequency "phonons" of the protein network. The function  $\ell$  is the lineshape function. For  $r_j = 0$  and  $r = 0$ , then  $L$  describes the ZPL associated with the total zero-point level of the excited electronic state. The ZPL is a

Lorentzian with a homogeneous width we denote as  $\gamma$ . As discussed elsewhere [12-16], for P870\* in the low T limit we may set  $\gamma(\text{cm}^{-1}) = (2\pi\tau c)^{-1}$  where  $\tau$  is the lifetime of P870\* and  $c$  is the speed of light. The sequential nonzero values of  $r = 1, 2, 3, \dots$  correspond to the one-, two-, ... phonon profiles obtained by convolving the one-phonon profile with itself  $r$  times [28,29]. The width of the one-phonon profile centered at  $\omega_m$  (relative to the ZPL) is defined as  $\Gamma$ . Guided by experimental data from the one-phonon profile in organic crystals, we have previously used Gaussian and Lorentzian line shapes for the low and high energy sides of the one-phonon profile rather than a symmetric and unphysical Gaussian profile which has been recently utilized by Middendorf et al. [34]. Within the harmonic approximation, the phonon sidebands that build on the ZPLs associated with total zero-point and the discrete modes are identical.

In our previous simulations of P870 and its hole spectra we considered only the phonons and one discrete mode, the special pair marker mode with Huang-Rhys factor  $S_{sp}$  and frequency  $\omega_{sp}$  (cf. Table I), because the hole spectra did not indicate the existence of more than one discrete mode.

To obtain the absorption spectrum, the single site profile is convolved with a Gaussian zero-phonon site excitation distribution function centered at  $\nu_m$  with a FWHM of  $\Gamma_i$ :

$$A_o = \int d\nu N_o(\nu - \nu_m) L(\Omega - \nu) \quad (2)$$

where  $N_o(\nu - \nu_m)/N$  is the probability of finding a site with a zero-phonon transition

frequency equal to  $\nu$ . If a narrow band laser (computationally 1/10 of the homogeneous linewidth of a zero-phonon line (ZPL), in reality the laser linewidth used in the present studies is less than 1/1000 of the homogeneous width of the ZPH) is tuned to  $\omega_B$  (the burn frequency) with an intensity  $I$  for a time  $\tau$ , the number of sites that remain at frequency  $\nu$  is given by  $N_i(\nu - \nu_m) = N_o(\nu - \nu_m) \exp[-\sigma I \phi \tau L(\omega_B - \nu)]$ , where  $\sigma$  is the absorption cross section and  $\phi$  is the hole burning quantum yield. The absorption spectrum after burning is then:

$$A_\tau = \int d\nu N_o(\nu - \nu_m) \exp[-\sigma I \phi \tau L(\omega_B - \nu)] L(\Omega - \nu) \quad (3)$$

The expression is valid for photochemical hole burning (PHB) and population bottleneck hole burning, but not nonphotochemical hole burning where the contribution to  $A_\tau$  from the anti-hole must be taken into account. The hole burned spectrum is defined as  $A_\tau - A_o$ .

With reference to the caption of Table I, we comment briefly on the value of  $50 \text{ cm}^{-1}$  previously used for the homogeneous width of the ZPL associated with the one-quantum transition of the marker mode,  $\omega_{sp}^1$ . This large value, which corresponds to a longitudinal relaxation time of 100 fs, was mandated by two observations: (1) burning a ZPH into the origin ( $\omega_{sp}^0$ ) band did not produce discernible higher energy satellite ZPHs associated with the one-, two-, ... quantum transitions of the marker mode; and (2) burning directly into the region of the one-quantum transition did not produce a ZPH coincident with  $\omega_B$  or a satellite ZPH in the region of the  $\omega_{sp}^0$  band. Of course, if the marker mode feature of the hole spectra

is due to two or more unresolved modes then a relaxation time quite as short as 100 fs would not need to be invoked, cf. section V.

With regard to the simulations presented later, we emphasize again [1-3] that the  $\omega_B$ -dependent hole spectra themselves provide the ZPH width and good first approximations for  $\omega_m$ ,  $S$ ,  $\omega_{sp}$ , and  $S_{sp}$ . A reasonable estimate of  $\Gamma_I$  is available since the width of the P870 absorption band is  $\approx \Gamma_I + \sum_i S_i \omega_i$  [29]. Thus, the simulations of the  $\omega_B$ -dependent hole spectra and the absorption spectrum itself should be viewed, to a considerable extent, as a refinement of parameter values obtained directly from the hole spectra.

Finally, we remark that it should not be expected that the main conclusions of our earlier work would be altered by higher quality hole spectra. These are that: (1) the linear electron-phonon coupling is strong (with  $S_{total} \sim 3.5$  and a total optical reorganization energy of  $\sim 240 \text{ cm}^{-1}$ ); (2) the low frequency phonons have a mean frequency of  $\sim 30 \text{ cm}^{-1}$  with  $S \sim 2$ ; and (3) there is an "effective" pseudo-localized mode, which we have called the marker mode (frequency of  $\sim 120 \text{ cm}^{-1}$  and  $S_{sp} \sim 1.5$ ) that contributes a Franck-Condon progression to P870. The only unresolved questions are related to the nature and modeling of the  $\omega_m$ -phonons and the dynamical nature of the marker mode (or modes) in the near vicinity of  $\sim 120 \text{ cm}^{-1}$ . Simulations of the low temperature absorption spectrum of P870 which ignore these facts and the absence of satellite ZPH hole structure from discrete modes have no physical basis [35].

## RESULTS

### Experimental and Simulated Spectra

The two hole burned spectra of P870 for deuterated *Rb. sphaeroides* RC shown in Figure 2 illustrate the significant improvement in the S/N ratio afforded by the new apparatus and methodology. Both the old (upper) and new (lower) spectra were obtained with samples from the same RC batch and exhibited identical absorption spectra at 4.2 K, including the same FWHM value for P870. In each spectrum the relatively sharp ZPH is coincident with  $\omega_B$  (burn frequency). Of more importance is the increased structure evident in the lower spectrum, in particular the doublet hole structure indicated by the two arrows. The higher energy hole is displaced from the lower by  $30\text{ cm}^{-1}$  with the latter displaced from  $\omega_B$  by  $\sim 115\text{ cm}^{-1}$ . The frequency  $\omega_B$  is in the near vicinity of the center of the site excitation frequency distribution ( $\nu_m$ ) and thus the intensity of the ZPH relative to that of the entire hole is approximately given by  $\exp(-2S_{\text{total}})$  [29]. The value of  $S_{\text{total}}$  from Table I is 3.3. The weakness of the ZPH reflects the fact that the ZPL is quite highly Franck-Condon forbidden.

Hole burned spectra were obtained for a large number of  $\omega_B$ -values. Four are shown in Figure 3 for  $\omega_B$ -values that span the  $120\text{ cm}^{-1}$  (vide infra) width of the inhomogeneous ZPL frequency distribution associated with the total zero-point level of P870\*. As in previous work and for reasons discussed later, the ZPH could only be observed for  $\omega_B$  less than a characteristic frequency which in this case is  $\sim 11,050\text{ cm}^{-1}$ . Returning to the doublet hole

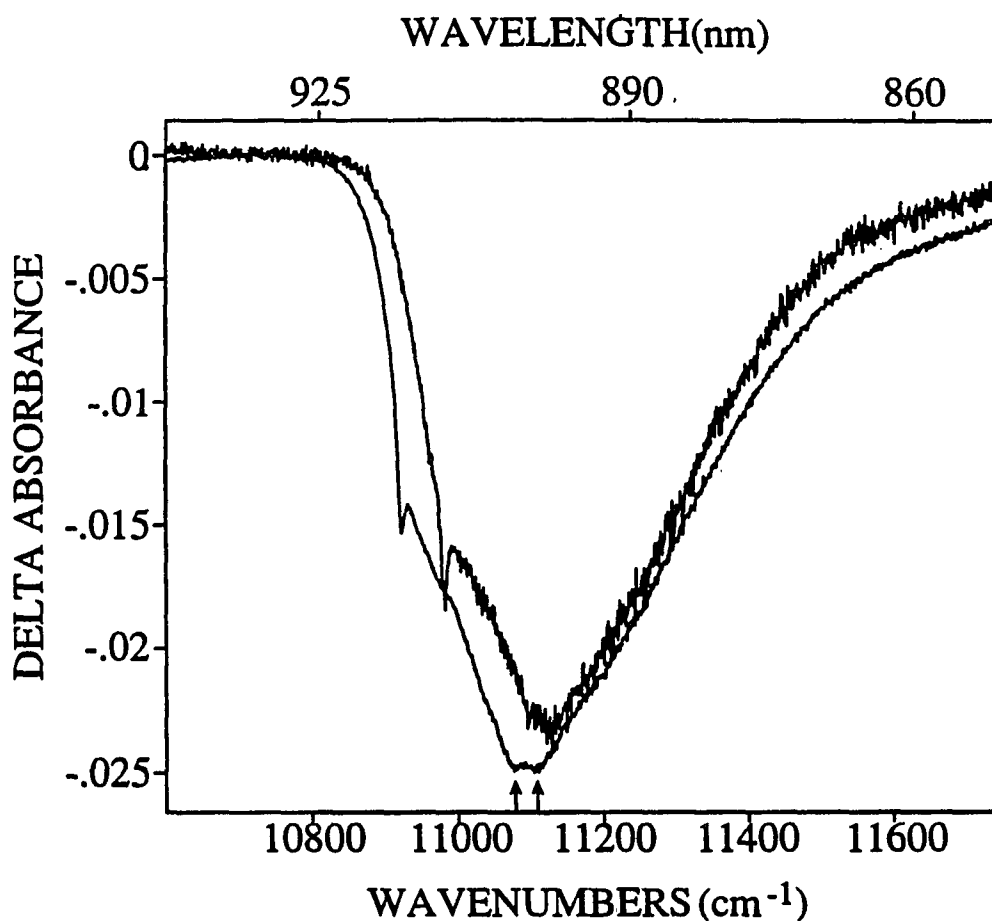


**Figure 2.** Comparison of current (bottom) and previous photochemical hole burned (PHB) spectra of P870 for the deuterated RC which show a  $\times 20$  improvement in S/N ratio, cf. section II.  $T = 4.2$  K. Note resolution of the doublet located by arrows in current spectrum, cf. text. The relatively sharp ZPH in each spectrum is coincident with the burn frequency ( $\omega_B$ ).

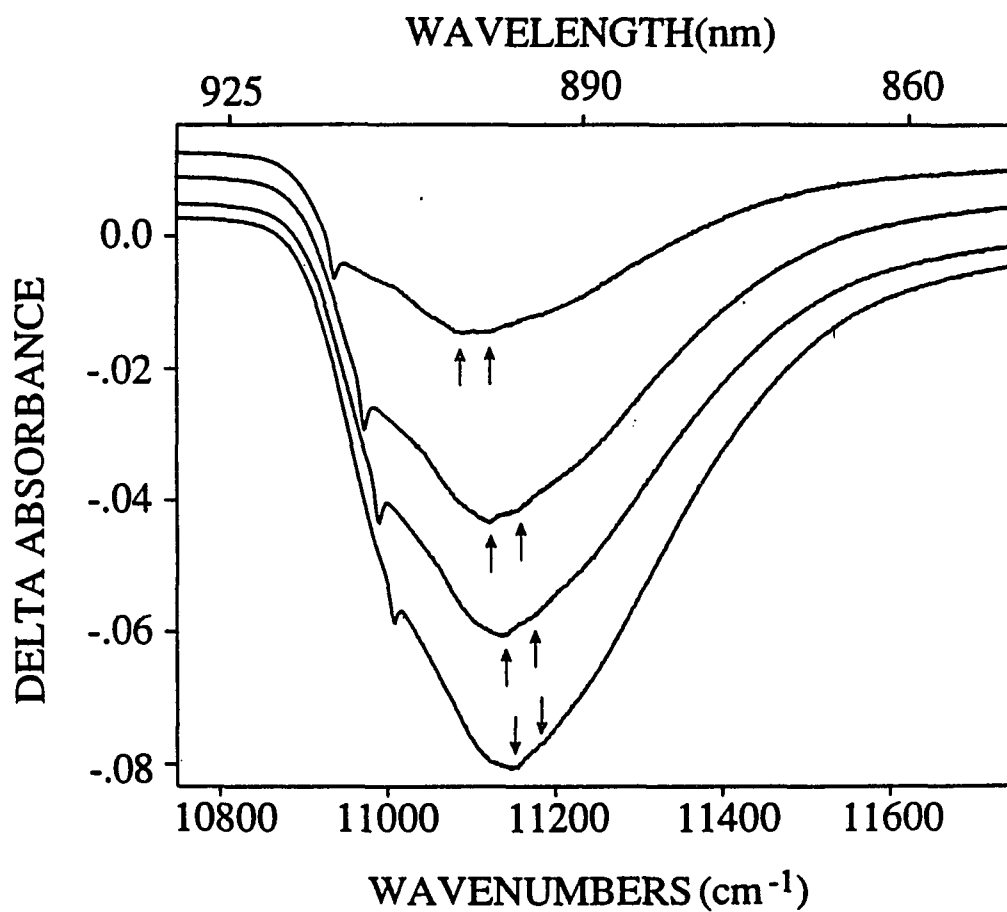


**Figure 3.** PHB spectra of P870 (deuterated, WT) for  $\omega_B = 10921, 10953, 10992$  and  $11040 \text{ cm}^{-1}$  (top to bottom),  $T = 4.2 \text{ K}$ . Note that the doublet hole structure (arrows) tracks the ZPH at  $\omega_B$ .

ZPH and, furthermore, that its intensity increases and decreases in parallel to the ZPH intensity across the range of  $\omega_B$ -values.

The hole burning spectroscopy of P870 for protonated *Rb. sphaeroides* RC was studied as extensively as for the deuterated RC. Spectra for the protonated RC analogous to those in Figure 3 are shown in Figure 4. For the protonated RC the ZPH could not be observed for  $\omega_B \geq 11,050 \text{ cm}^{-1}$ . The most apparent difference between the spectra of Figures 3 and 4 is that the doublet hole structure is not resolved for the protonated RC. We believe this to be significant since the P870 absorption bandwidth is very nearly the same for the two systems. Possible explanations of the doublet structure are considered in section V.

As attested to by Figures 3 and 4, there is a strong dependence of the hole spectrum on  $\omega_B$ . The objective of the simulations is to account for the  $\omega_B$ -dependence as well as the P870 absorption spectrum with a single set of values for the theoretical variables. However, for a given  $\omega_B$ -value that yields a structured hole spectrum, the structure will begin to wash out for sufficiently high burn intensities and, furthermore, the ZPH will be subject to saturation broadening in accordance with theory. Figure 5 shows hole spectra for P870 of the deuterated RC obtained burn intensities of 30 and 400 mW/cm<sup>2</sup>. On the basis of spectra of this type we have concluded that saturation broadening of the ZPH is absent for optical density change less than 20% as measured at the P870 maximum (cf. section B for the procedure used in the determination of the ZPH width). In our simulations we have focused on hole spectra with %-OD changes of <20%.



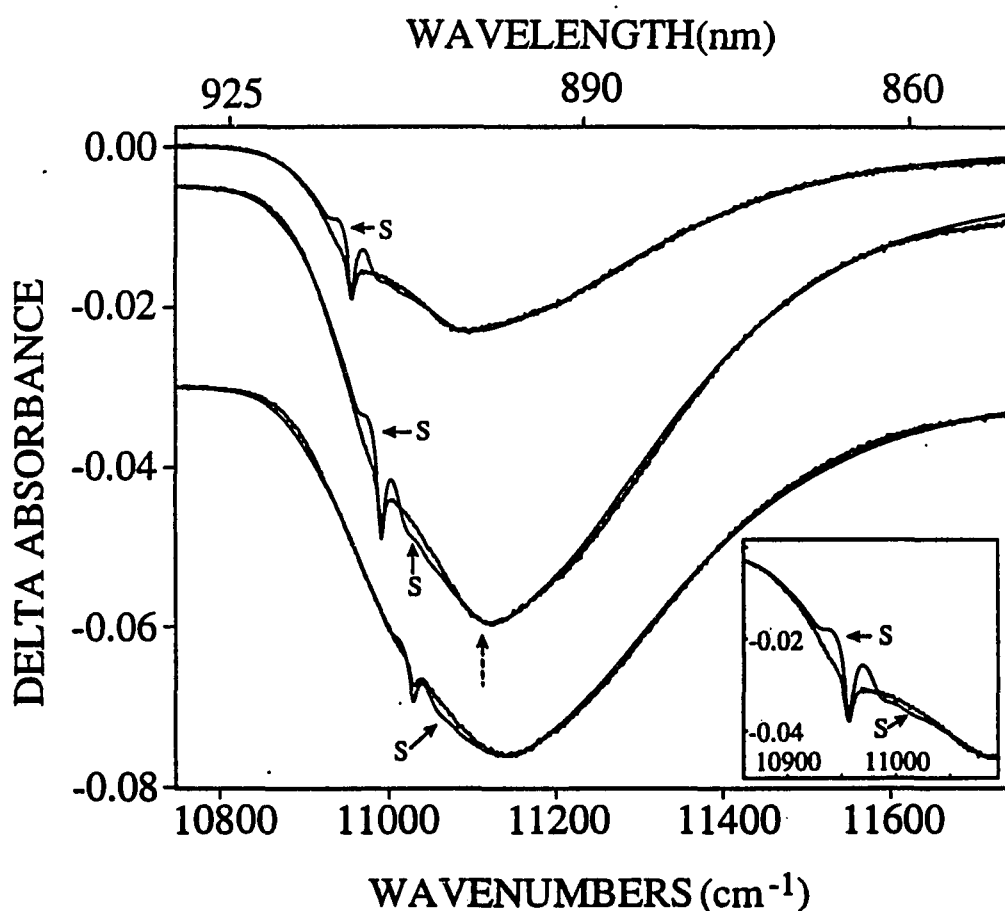


**Figure 4** PHB spectra of P870 (protonated, R-26) for  $\omega_B = 10921, 10992$  and  $11039 \text{ cm}^{-1}$  (top to bottom),  $T = 4.2 \text{ K}$ . Simulations (S) of these spectra were obtained with the parameter values of Table II. The dashed arrow indicates the position where the satellite ZPH of  $\omega_{sp}^1$  would occur if the marker mode were not damped, cf. text. The inset is a blow-up of the region around the ZPH for the upper spectrum.

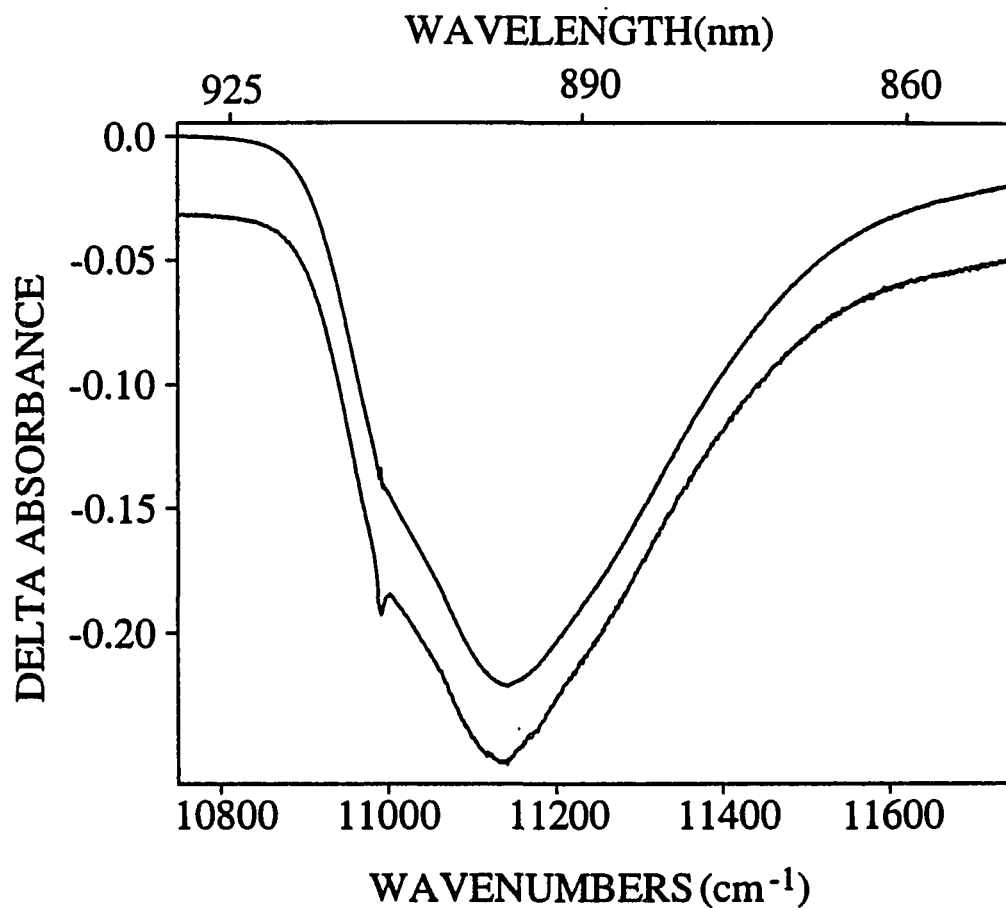


**Figure 5** Effect of burn intensity on the PHB spectrum of P870 (deuterated, WT),  $T = 4.2$  K. The  $\Delta A$  scale is for the lower spectrum obtained with  $I_B = 30$  mW/cm<sup>2</sup>. The upper spectrum ( $\div 6.4$ ) was obtained with  $I_B = 400$  mW/cm<sup>2</sup>; notice the washing out of structure including the ZPH.

For P870 of the protonated RC we found that a "two-mode model" ( $\omega_m$ ,  $\omega_{sp}$ ) sufficed for a good accounting of the absorption and hole spectra. (It was found sufficient to terminate the sums in Eq. (1) at  $r, r_{sp} = 10$ .) Our final parameter values are listed in Table II, see also the caption. The value of  $\gamma = 11 \text{ cm}^{-1}$  is the measured value, cf. next subsection. The fits to three of the hole spectra are shown in Figure 4. The dashed arrow in the middle spectrum locates where the  $\omega_{sp}^{-1}$  satellite ZPH would appear if the damping of the marker mode level was sufficiently reduced below  $50 \text{ cm}^{-1}$ , cf. Figure 6. The fit to the top spectrum of Figure 4 plus the insert illustrate that it is the region in the near vicinity of the ZPH that presents the greatest difficulty (this is also the case for the deuterated RC, vide infra). As discussed in section V, this is due to an inadequate functional description of the low energy side of the single-site, one-phonon profile.

A two-mode model was also used to simulate the spectra for P870 of the deuterated RC. The fit to absorption obtained with the parameter values listed in Table II is shown in an insert of Figure 1A. The fits to three hole spectra appear in Figure 7. The top spectrum of Figure 7 shows again that the fit to the region in the near vicinity of the ZPH is unsatisfactory. In addition, the simulation fails to reproduce the doublet (dashed arrows) hole structure discussed earlier. The dashed arrow in the middle spectrum is analogous to the one just discussed in Figure 5. That is, the position of  $\omega_{sp}^{-1}$  if the homogeneous width of  $50 \text{ cm}^{-1}$  for the one-quantum level of the marker mode was also used for the deuterated RC.

Table II. Structure of P870.<sup>a</sup>

P870	$\omega_{sp}/S_{sp}$ <sup>b</sup>	$\omega_m/S$	$\Gamma$ <sup>c</sup>	$\Gamma_I$	$\nu_m$	$\Gamma_{ZPH}$
Protonated	120/1.5	30/1.8	32.5	150	10992	$11.5 \pm 1.0$
Deuterated	115/1.5	30/2.0	32.5	130	10992	$11.3 \pm 1.0$

<sup>a</sup>Units of  $\omega_{sp}$ ,  $\omega_m$ ,  $\Gamma$ ,  $\Gamma_I$ ,  $\nu_m$  and  $\Gamma_{ZPH}$  (zero-phonon holewidth) are in  $\text{cm}^{-1}$ .

<sup>b</sup>Homogeneous width of the ZPL for the marker mode level  $\omega_{sp}^1$  is  $50 \text{ cm}^{-1}$ . Widths for the  $\omega_{sp}^j$  ( $j \geq 2$ ) are  $j (50 \text{ cm}^{-1})$  [a Fermi-Golden rule prediction with cubic anharmonicity].

<sup>c</sup>One-phonon profile on low and high energy sides is a Gaussian (half-width =  $10.0 \text{ cm}^{-1}$ ) and Lorentzian (half-width =  $22.5 \text{ cm}^{-1}$ ), respectively.

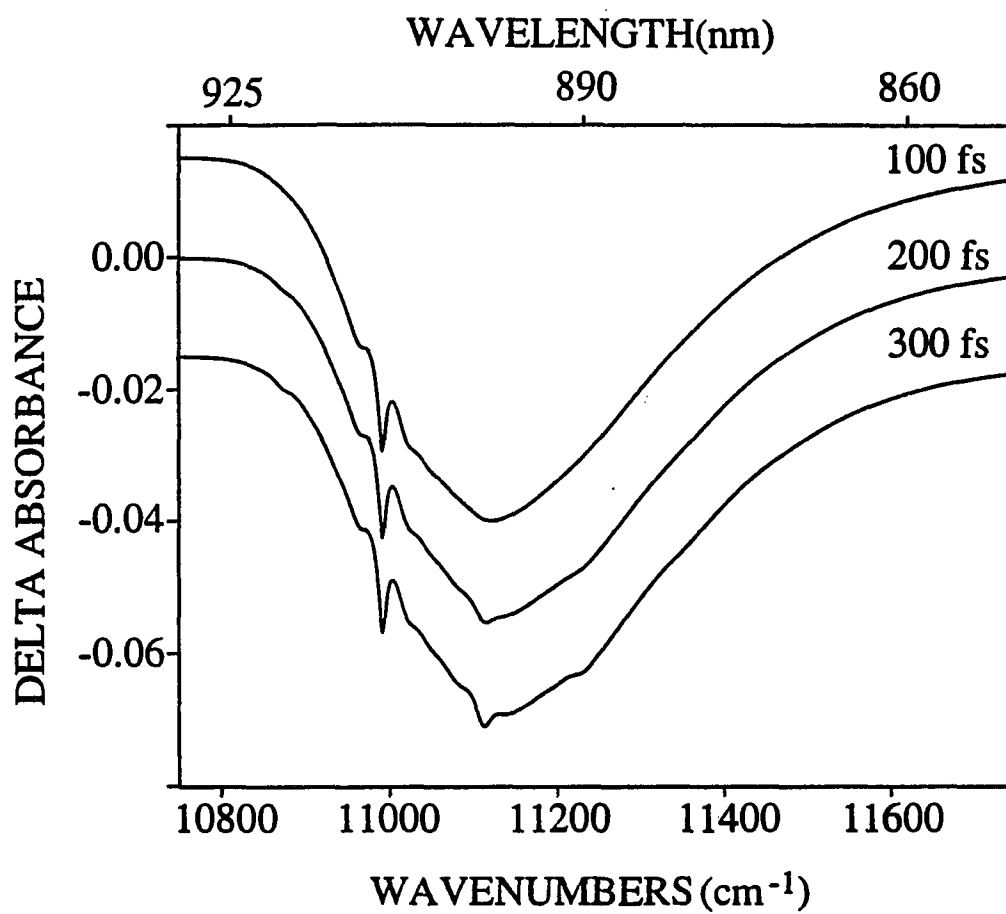


**Figure 6** Simulations of PHB spectrum of P870 (protonated, R-26) for different marker mode relaxation times.

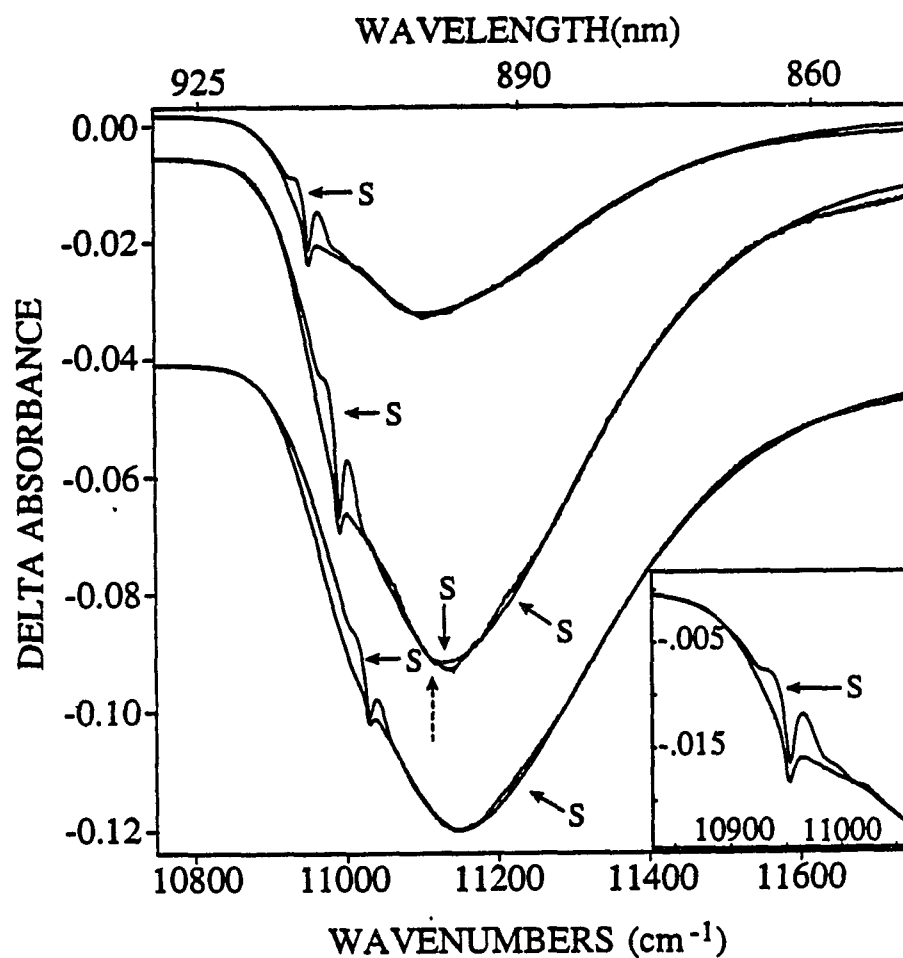


**Figure 7** PHB spectra of P870 (deuterated, WT) for  $\omega_B = 10921, 10992$  and  $11040 \text{ cm}^{-1}$  (top to bottom),  $T = 4.2 \text{ K}$ . The curves labeled with S are theoretical simulations, cf. Fig. 4 caption.

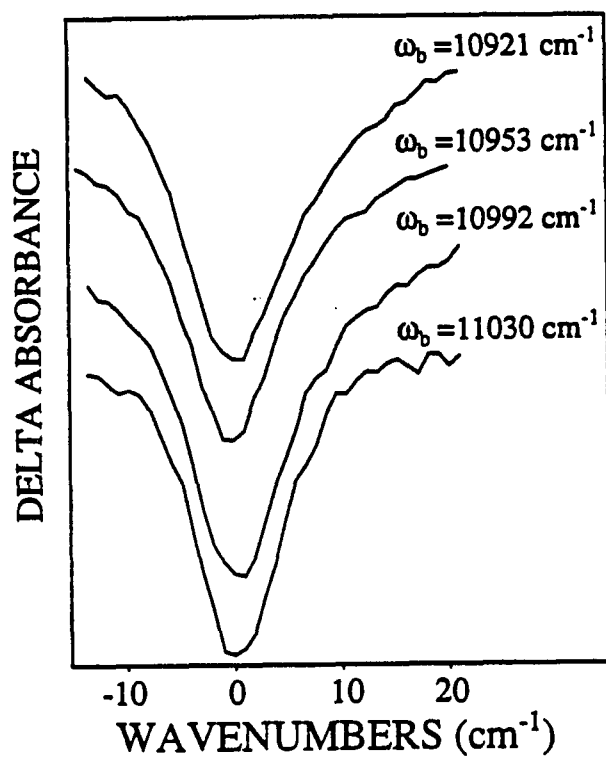
### Zero-Phonon Holewidths

For the protonated and deuterated RCs, P870 ZPH widths were measured at 4.2 K for 10 and 9  $\omega_B$ -values that spanned the range 10921-11049 and 10921-11068  $\text{cm}^{-1}$ , respectively. From Table II it can be seen that these ranges encompass the distribution of ZPL excitation frequencies for the total zero-point level. For all  $\omega_B$ -values the quality of the spectra was comparable to those of the spectra in Figures 3, 4, and 7. Examples of the ZPH profiles used for analysis are given in Figures 8 and 9. The ZPH profiles were systematically fit with a curve fitting program from Spectra Calc [36]. The fitting procedure used included a fit to the ZPH including  $\pm 20 \text{ cm}^{-1}$  of data with a Lorentzian lineshape. Because the ZPH rides on the broad hole, a linear baseline was fit simultaneously with the ZPH. The procedure was tested by simulating hole spectra with ZPH widths ranging from 5 to 20  $\text{cm}^{-1}$  and values of the other parameters as given in Table II. The hole spectra were then fit with the curve fitting program and the resulting widths were within  $\pm 0.5 \text{ cm}^{-1}$  of the simulated ZPH widths.

For both the protonated and deuterated RC the ZPH width did not show any dependence on  $\omega_B$ ; the widths for both are  $11.5 \pm 1.0 \text{ cm}^{-1}$ , corresponding to a P870\* lifetime of  $0.93 \pm 0.10 \text{ ps}$  at 4.2 K.

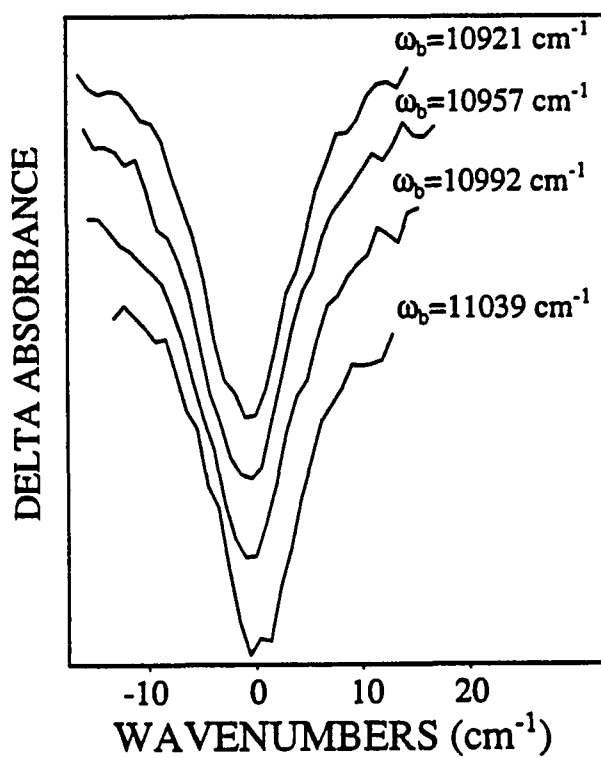
### Temperature Dependencies of the ZPH Intensity and Width

Figure 10 shows the temperature dependence of the zero-phonon hole profile ( $\omega_B = 10,992 \text{ cm}^{-1}$ ) for P870 of the deuterated RC. As can be seen, the ZPH peak intensity undergoes a marked decrease from 1.6 to 16 K. Johnson et al. [16] reported a similar



**Figure 8** Four representative ZPH profiles for the deuterated RC, T = 4.2 K. Burn frequencies are given in the figure. These profiles plus five others yielded at ZPH width of  $11.5 \pm 1.0 \text{ cm}^{-1}$  (95% confidence limit). The fits to the profiles, cf. text, are not shown because they would be indistinguishable from the exponential profiles.





**Figure 9** Four representative ZPH profiles for the protonated RC, T = 4.2 K. These profiles plus six others yielded a ZPH width of  $11.5 \pm 1.0 \text{ cm}^{-1}$  (95% confidence limit), cf. Fig. 8 caption.

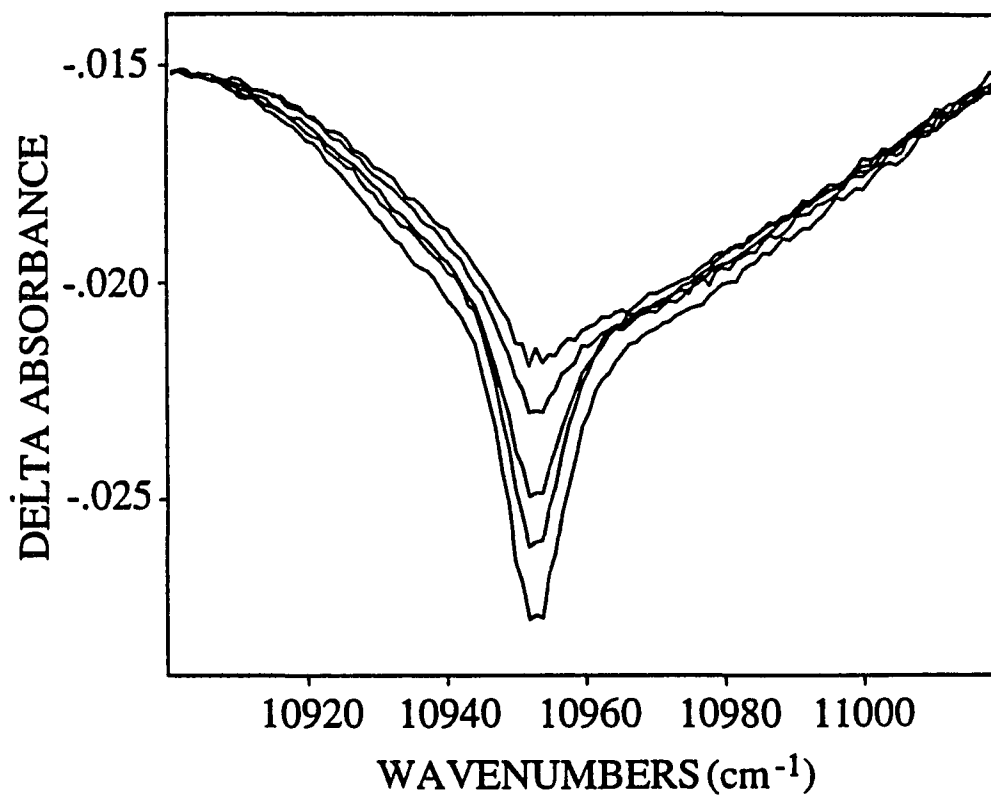


**Figure 10** Temperature dependence of the ZPH profile for the deuterated RC (WT). From top to bottom  $T_B = T_R = 16, 12, 8.0, 4.2$  and  $1.8$  K where  $T_B$  and  $T_R$  are the burn and read temperatures. Note how intensity from the ZPH is drained by the real-PSBH as  $T_B$  is increased.

dependence on temperature between 4.2 and 14 K for the protonated RC (R26). As in their experiments, we could not observe the ZPH at temperatures higher than ~16 K. Using the standard expression [29] for the T-dependence of ZPH intensity stemming from the linear electron-phonon coupling,  $I \propto \exp\{-2S(2\bar{n} + 1)\}$  when  $\bar{n} = [\exp(\hbar\omega/2kT) - 1]^{-1}$  is the occupation number for an effective mode frequency  $\omega$ , Johnson et al. obtained the value  $\omega = 23 \pm 4 \text{ cm}^{-1}$  (for  $S = 2.2$ ). Based on our results, we now believe the above expression to be an oversimplification of the physics of the low frequency modes of proteins and postpone the discussion of our analysis of Figure 10 until section V.

With increasing temperature, Figure 10 shows that the intensity of the phonon sideband holes increase, especially on the high energy side of the ZPH in accord with the expression derived by Lyle [32]. However, for 1.8, 4.2 and 8.0 K the interference is sufficiently low to permit a measurement of the ZPH width. We find that the width is invariant in this range, that is within  $\pm 1.0 \text{ cm}^{-1}$  of  $11.5 \text{ cm}^{-1}$ , cf. Table II. Based on the time domain measurements of the temperature dependence of the P870\* lifetime (10 K - room T) [21] and theoretical analyses [18,37] one would expect a weak (at best) dependence for  $T < 10 \text{ K}$ . Nonetheless, the present results are the first to establish that this is the case.

## DISCUSSION

### Dependence of the ZPH Width on Site Excitation Frequency ( $\omega_B$ )

Very recently, ultra-fast time domain experiments have shown that the decay of P870\* decay at room temperature is nonexponential [24-27]. For example, Vos et al. [24] fit the decay for the R26 mutant with a biexponential, 2.9 ps (0.65) and 12 ps (0.35). Stimulated by these results Small et al. [18] derived the following expression for the electron transfer rate of a single RC:

$$k = 2\pi V^2 \left[ 2\pi \tilde{S} (\sigma^2 + \omega_m^2) \right]^{-1/2} \exp \left[ -(\Omega - S \omega_m) / 2\tilde{S} (\sigma^2 + \omega_m^2) \right] \quad (4)$$

which is valid for strong linear electron-phonon coupling.  $S$  and  $\omega_m$  are as defined before,  $\tilde{S} = S \coth(\hbar\omega_m/2kT)$ ,  $V$  is the electronic coupling matrix element between  $P^*$  and relevant charge-separated state of the RC,  $\Omega$  is the adiabatic energy gap between these two states and  $2\sigma$  is the width of the one-phonon profile of the nuclear factor. For a Gaussian distribution of  $\Omega$ -values centered at  $\Omega_o$ , the average value of the rate is

$$\begin{aligned} \langle k \rangle &= 2\pi V^2 \left[ 2\pi (\tilde{\Gamma}^2 + \tilde{S} (\sigma^2 + \omega_m^2)) \right]^{-1/2} \\ &\times \exp \left[ -(\Omega_o - S \omega_m)^2 / 2(\tilde{\Gamma} + \tilde{S} (\sigma^2 + \omega_m^2)) \right] \end{aligned} \quad (5)$$

where  $2\tilde{\Gamma}$  is the width of the  $\Omega$ -distribution. Equations (4) and (5) are trivially generalized to include the special pair marker mode. Using hole burning data and low temperature optical data for charge-transfer organic crystals, Small et al. concluded that dispersive kinetics from the  $\Omega$ -distribution is very unlikely to be responsible for the aforementioned nonexponential decay of P870\*. They suggested dispersive kinetics from a distribution of  $V$ -values as another possibility.

The results presented in section IV.B prove that the electron-transfer time of P870\* (from total zero-point) is invariant to excitation frequency within the inhomogeneous distribution of zero-phonon line frequencies. Unfortunately, this negative result, by itself, cannot be interpreted as meaning that nonexponential decay kinetics for P\* could not arise from a distribution of values for the coupling matrix element  $V$ . The reason is that the inhomogeneous ZPL-absorption frequency distribution depends on the distribution functions for the ground and excited state energies ( $E$ ,  $E^*$ ) of the special pair,  $f_P(E)$  and  $f_P^*(E^*)$ , and the extent-type of correlation between them (for a detailed discussion see [38]). Noting that at any given value of  $E$  of  $P$  there is a high degree of accidental degeneracy, an absence of correlation means that  $\Gamma_I$  of P870 is the width of  $f_P^*(E^*)$  and, furthermore, that at any excitation frequency one essentially samples the entire ensemble of RCs, i.e., all possible  $V$ -values. At the other extreme there is perfect positive or negative correlation. In this case the width of  $f_P^*(E^*) < \Gamma_I$  of P870 and, also, different excitation frequencies would sample different subsets of the RC ensemble and, therefore, also different parts of the  $V$ -value distribution. The actual situation may lie between these two extremes.

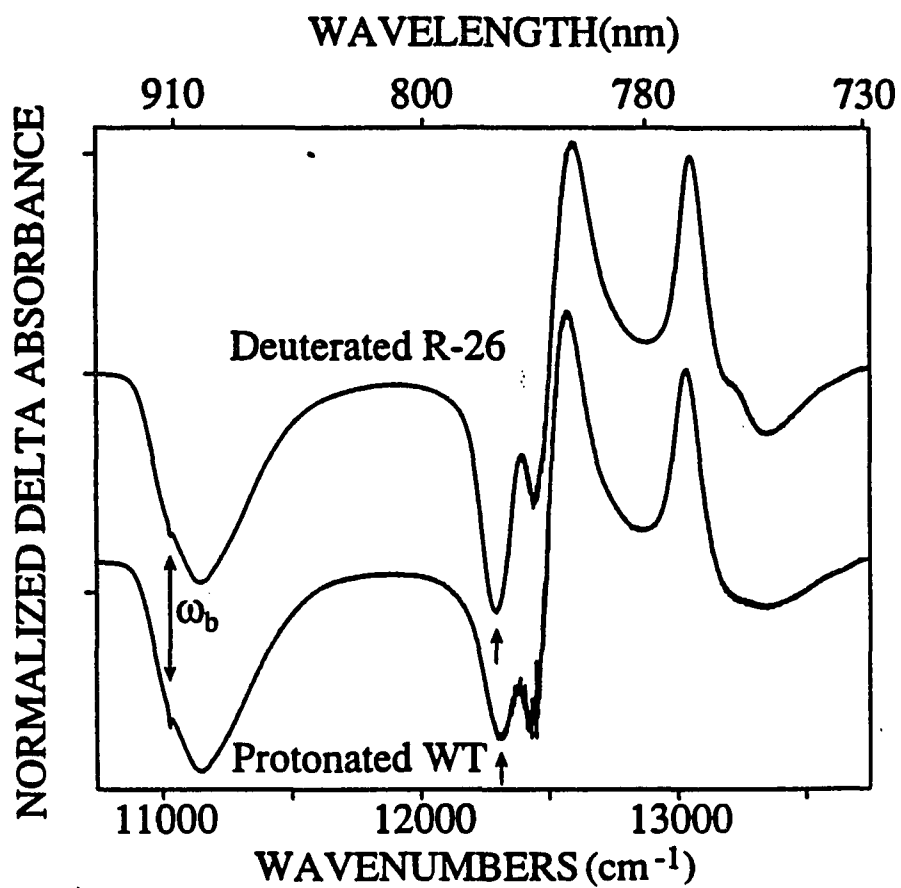


**Figure 11**  $\Delta$ -absorbance spectra of the entire  $Q_y$ -absorption region obtained by burning into P870. Upper and lower spectra are for the deuterated and protonated RC, respectively. The upper dimer component ( $P_+$ ) is located by the arrow.

However, the above negative result, when viewed in concert with two other recent findings, leads to the conclusion that a distribution of V-values is unlikely to be the source of the nonexponential decay of P870\*. The first finding, from  $\omega_B$ -dependent PHB spectra of the RCs from *Rps. viridis* and *Rb. sphaeroides*, is that the site excitation energies of P\*(P<sub>-</sub>) and P<sub>+</sub> (the upper excitonic dimer component of the special pair) are positively correlated [15]. The upper dimer component is the low energy shoulder of the most intense band at 830 nm in absorption, cf. Figure 1. This component is resolved in the hole burned spectra shown in Figure 11 for both the protonated and deuterated RC (cf. following paper for a detailed discussion of P<sub>+</sub> for *Rps. viridis*). Using the value of  $\nu_m$  from Table II and the frequencies of the P<sub>+</sub>-hole maxima in Figure 11 yields an adiabatic dimer splitting of 1303 and 1319 cm<sup>-1</sup> for the deuterated and protonated RC, respectively. The second finding is to be found in the following paper on the nonphotochemical hole burning of P960 of *Rps. viridis*, wherein a quite remarkable, persistent photoinduced structural transformation of the special pair is revealed. The transformation produces an antihole of P<sub>-</sub> that is shifted ~150 cm<sup>-1</sup> to the red of the P<sub>-</sub> hole and an anti-hole of P<sub>+</sub> that is shifted ~150 cm<sup>-1</sup> to the blue of the P<sub>+</sub> hole. This negative correlation is consistent with the simple excitonic dimer model. Thus, the above positive correlation establishes that the inhomogeneous broadening of P870 (P960) is due primarily to statistical fluctuations in protein structure around the cofactors rather than a distribution of special pair structures. Noting also that the dimer splitting is large, ~1300 cm<sup>-1</sup> while  $\Gamma_I$  for P870 is small, 130 cm<sup>-1</sup>, it is clear that variations in the structure of the special pair from RC to RC in the ensemble are very small. One can reasonably

assert, therefore, that the structure of the special pair and the two neighboring BChl monomers is also extremely well-defined and, as a consequence, that the distribution of V-values is very narrow.

Next we consider the possibility that the observed nonexponentiality of P870\* is the result of heterogeneity that is above and beyond the type we have referred to as "normal glass-like." That is, there are two distinct subsets of the RC ensemble, one yielding a P870\* decay time of ~3 ps (0.65) and the other a decay time of ~12 ps (0.35). We think this very unlikely since we have never observed a P870 ZPH profile that is a sharp feature hole superimposed on a broader hole of the type shown in Figures 3, 4, 8, and 9. Of course, one could always argue that the electron-phonon coupling for the (0.35) subset is very significantly greater than that of the (0.65) subset but there is no physical basis for this.

### The Underlying Structure of P870

A comparison of the results in Tables I and II shows that our earlier main conclusions regarding the underlying structure of P870 (and by implication P960 of *Rps. viridis*, see following paper) are left unchanged by the present experimental results (as well as the very recent results from Boxer and coworkers on the wild type RC of *Rb. sphaeroides* [34]). However, the present hole spectra now show clearly that the simulations are inadequate in the region of the ZPH and, for the deuterated RC, in the region of the marker mode. We consider now possible reasons for the discrepancies.



### Modeling of the Low Frequency "Phonons"

The inserts of Figures 3 and 4 show that the simulation underestimates the contribution of the low frequency modes ( $\leq 20 \text{ cm}^{-1}$ ) to higher and lower energy of the ZPH. (Inspection of the experimental profiles just to the red of the ZPH in Figures 3 and 4 show a distinct "bulging" at  $\sim 30 \text{ cm}^{-1}$  which is the pseudo-phonon sideband hole.) As discussed earlier we have used an asymmetric one-phonon profile centered at  $\omega_m$  with the lower and higher energy sides described by a Gaussian and broader Lorentzian, respectively. From Table II the respective half-widths for the protonated RC are 10 and  $22.5 \text{ cm}^{-1}$ . By significantly broadening the Gaussian it is possible to force agreement between experiment and simulation as one might expect (results not shown). However, from the form of the single site absorption profile (Eq. 1), it can be seen that this broadening leads to unphysical absorption to the red of the zero-phonon line at 0 K which, in turn, contaminates the region of the pseudo-phonon sideband in the hole spectrum. This is why in our simulations we have used Gaussian half-widths which are  $< \omega_m/2$ . Although a Gaussian should provide a reasonable approximation to the low energy side of the one-phonon profile for a Debye phonon density of states, which is proportional to  $\omega^2$ , it fails for the special pair of the RC. This suggests that the density of states of low frequency modes in the protein is anomalous, i.e., not Debye-like.

This suggestion finds strong support from recent neutron inelastic scattering [39], Raman [40] and hole burning [41-42] studies of amorphous and crystalline polymers. For example, Kanaya et al. [39] have reported that while crystalline polyethylene exhibits a Debye-phonon

density of states ( $\leq 80 \text{ cm}^{-1}$ ), amorphous polyethylene exhibits an additional density from special modes that peaks at  $\omega_p \sim 30 \text{ cm}^{-1}$ , tails to higher energy and, after a small decrease on the low energy side of  $\omega_p$  appears to level off. The above groups associate the special modes with the microscopic disorder of the polymer. This being the case they should not be referred to as phonons (acoustic). A variety of experimental investigations of inorganic glasses have also led to the identification of disorder-induced low frequency modes (see Buchenau et al. [43] and references therein) which may be highly anharmonic at sufficiently low energy, several Kelvin [44].

We believe that the temperature-dependence of the ZPH intensity shown in Figure 10 provides further evidence for the activity of such low frequency anomalous modes. As discussed in section IV.C., Johnson et al. [16] fit their T-dependent (4.2-14 K) intensity data to the standard theoretical expression (with  $S = 2.2$ ) to arrive at a mean phonon frequency of  $\omega_m = 23 \pm 4 \text{ cm}^{-1}$ . Using the same expression (with  $S = 2.0$ , Table II) to fit our data for 4.2 K and the higher temperatures we obtained a value of  $\omega_m = 17 \pm 2 \text{ cm}^{-1}$ . The problem is that with  $S = 2.0$  and  $\omega_m = 17 \text{ cm}^{-1}$ , the theory predicts that the ZPH intensities at 1.6 K and 4.2 K should be equal. This is at odds with the results of Figure 10. The significant decrease in intensity from 1.6 to 4.2 K indicates considerable activity of modes of very low frequency which, in turn, means that the theoretical expression used above is inappropriate. In future simulations of hole profiles in polymers, glasses and proteins, we believe that it will be important to account for the contribution to the one-phonon profile from the special low frequency modes associated with the amorphous solid.

### The Special Pair Marker Mode $\omega_{sp}$

We have previously assigned the  $\omega_{sp}$ -mode as an intermolecular pseudo-localized vibration whose amplitude is highly localized on the special pair. The argument against the assignment as a low frequency intramolecular mode of BChl *a* was based on the fact that the largest S-value for an intramolecular mode ( $\sim 740\text{ cm}^{-1}$ ) of Chl *a* and BChl *a* is 0.05 [8,20], which is about a factor of 30 times lower than  $S_{sp}$ , Table II. Furthermore, in ref. 20 no intramolecular mode with a frequency lower than  $260\text{ cm}^{-1}$  was observed which meant that their S-values are  $\leq 0.001$ . Very recently, nonphotochemical hole burned spectra of the BChl *a* B870 and B895 bands of the antenna of *Rb. sphaeroides* have been reported [9]. Both of these bands are associated with states that are characterized, in part, by a strong dimer interaction. However, the marker mode of the special pair is absent in the spectra and, furthermore, the electron-phonon coupling of the low frequency modes is weak ( $S < 1$ ). Thus, it continues to seem likely that [1-3] the strong activity of the low frequency modes and marker mode is due to a significant amount of charge-transfer character for P870\* [45-47].

Before considering the dynamical nature of the marker mode further, it is appropriate first to discuss the doublet hole structure observed in the region of the marker mode for P870 of the deuterated RC, see arrow-labeled features of Figure 2. According to the simulations of the spectra, vide supra, the lower energy component is a two-quantum transition involving the marker mode plus one-phonon profile ( $\omega_m = 30\text{ cm}^{-1}$ ). Since the higher energy component of the doublet is displaced  $\sim 30\text{ cm}^{-1}$  to higher energy of the lower component and given that  $S = 2.0$ , a plausible assignment for the higher energy component is  $\omega_{sp}^1 + 2\times\omega_m$ ,

i.e., one quantum of  $\omega_{sp}$  plus the two-phonon transitions (profile). However, with our theoretical model it was not possible to satisfactorily simulate the doublet component structure in this manner nor explain why this structure is not observed for the protonated RC, Figure 4. But as discussed in the previous section, the assumption of the model that the low frequency phonons are Debye-like is most likely incorrect, i.e., glass-like anomalous modes appear to be very important. Until we understand how to model the one-phonon profile and how to generate the multi-phonon profiles from it, the above interpretation of the doublet structure cannot be dismissed. The absence of the doublet structure for P870 of the protonated RC is interesting. If one assumes that the above interpretation for the doublet structure is correct, one is forced to consider that either the one-phonon profile is sensitive to deuteration (which seems unlikely given the low mode frequencies) or that the marker mode relaxation time (100 fs in our simulations) is lengthened by deuteration so as to yield a more structured spectrum, see Figure 11. The latter possibility finds support from the picosecond data of Dlott and coworkers [48] on optical phonon relaxation times in protonated and deuterated organic crystals. They were able to explain the dependence of the relaxation time on optical phonon frequency using a simple phonon density of states argument. Since the marker mode frequency is high ( $120\text{ cm}^{-1}$ ) and comparable to the effective Debye frequency ( $\omega_D$ ) of organic solids and, for example,  $\omega_D$  for naphthalene is reduced by 20% upon deuteration [48], it is conceivable that  $\omega_{sp}$  for the deuterated RC has a longer relaxation time which, together with an accurate one-phonon profile, could lead to agreement between the experimental and simulated spectra.

A second interpretation of the doublet structure is that it is due to two marker modes with frequencies of  $\sim 120$  and  $\sim 150 \text{ cm}^{-1}$  (although here again one is left with the question of why the doublet is not observed for the protonated RC). Based on our experience with simulations it is clear that the model with phonons plus two marker modes (whose S-values sum approximately equal to  $S_{sp}$  of Table II) could simulate the doublet structure, although it would still fail to fit the region around the ZPH. However, such a simulation at this time is not deemed worthwhile given that we do not know how to accurately model the one-phonon profile.

We turn next to a consideration of the relevance of the data from recent resonance Raman studies of P870 (protonated RC) [35,49,50] to the hole spectra, i.e., the underlying vibrational structure of the P870 band. These works (in particular ref. 35) have revealed considerable mode activity in the important low frequency region ( $\leq 200 \text{ cm}^{-1}$ ). The lowest frequency mode observed by Shreve et al. is  $36 \text{ cm}^{-1}$  with a width of  $\sim 15 \text{ cm}^{-1}$  comparable to that of the intramolecular modes, while Palaniappan et al. were not able to access the region below  $50 \text{ cm}^{-1}$ . At the outset it must be emphasized that in these works Raman excitation profiles for the modes are not reported and overtones were not observed. This means that S-factors, damping constants and the site inhomogeneous band broadening are not obtainable from the Raman spectra.

Important also to the discussion is an understanding of the irrefutable results from hole burning studies. We emphasize again only that low frequency modes with a "mean" frequency  $\omega_m \sim 30 \text{ cm}^{-1}$  couple strongly to the  $\text{P870}^* \leftarrow \text{P870}$  transition with an S-value of

~2.0 (as emphasized in the Introduction the coupling of such "phonons" to the  $Q_y$ -transition of Chls in proteins is ubiquitous with a one-phonon profile that carries a width of  $\sim 40\text{ cm}^{-1}$ ). The high S/N spectra presented here simply further confirm the correctness of our earlier physics, e.g., direct observation of the  $30\text{ cm}^{-1}$  pseudo-phonon sideband hole, Figures 3 and 4, and the temperature dependence of the ZPH intensity, Figure 10, which cannot be understood by invoking discrete modes in the Raman spectrum with frequencies  $\geq 36\text{ cm}^{-1}$ ! The reader is also referred to the following paper in which the real-phonon sideband hole for P960 of *Rps. viridis* at  $\sim 25\text{ cm}^{-1}$  is resolved for the first time and a novel line-narrowed P960 absorption spectrum is presented that is obviously consistent with our earlier results on the marker mode.

Palaniappan et al. report 25 K resonance Raman spectra for P870 that show 18 bands between  $52$  and  $404\text{ cm}^{-1}$  with widths of  $\leq 10\text{ cm}^{-1}$ . They assign the bands as intramolecular modes of BChl. The intensity distribution over this range is more or less uniform although they report that the relative intensities are accurate to no better than about a factor of about 3. One must assume that this uncertainty extends across the above frequency range. Therefore, it follows ("by eye") that the Raman intensities cannot be directly used to model the P870 low temperature absorption profile and, therefore, the hole spectra. Thus, Palaniappan et al. were forced to use a multi-parameter model with variable weighting coefficients (with most of the above modes plus several additional higher frequency modes, up to  $736\text{ cm}^{-1}$ ) to simulate the P870 band (i.e., a stick-model with  $\Gamma_1 = 140\text{ cm}^{-1}$ ). The resulting S-factors bear no relationship to the observed Raman intensities. Of particular

interest, in view of our earlier and present results, is that their fits yield S-factors of 0.63, 0.43 and 0.43 (for a total of 1.5, cf. our  $S_{sp}$  value in Table II) for modes at 105, 130 and 140  $\text{cm}^{-1}$ . Their two lowest frequency modes at 52 and 80  $\text{cm}^{-1}$  have S-factors of 0.30 and 0.23. The S-factor for the 15 modes with frequency  $>140 \text{ cm}^{-1}$  are a factor of 10 or more smaller than 0.63. The highest frequency mode at 736  $\text{cm}^{-1}$  has an S-factor of 0.03. It should be obvious that Palaniappan et al.'s 20-parameter fit arrives, more or less, at the results of Table II, albeit with three modes in the near vicinity of our marker mode ( $s_{sp} = 120 \text{ cm}^{-1}$ ) and the 52 and 80  $\text{cm}^{-1}$  modes as unphysical substitutes for the critically important low frequency phonons. It is also the case that their model for P870 (inhomogeneously broadened discrete modes) would lead to calculated hole spectra that bear no relationship to the experimental spectra [28-31]. Furthermore, Palaniappan et al. provide no Raman data that support the high S-values of the 52, 80, 105, 130 and 140  $\text{cm}^{-1}$  modes which they assign as out-of-plane intramolecular BChl modes of the special pair. Stated, without proof, is that the intensities of the low frequency ( $\leq \sim 200 \text{ cm}^{-1}$ ) Raman modes of P870 are about a factor of 10 higher than those obtained for the two BChl monomers of the RC.

This statement does seem consistent with the Raman intensities reported by Shreve et al. and our measurements of intramolecular Franck-Condon factors (vide supra). Shreve et al. report relative intensities for their modes at 36, 71, 94, 127, 202, 337, 685 and 730  $\text{cm}^{-1}$  modes of 0.4, 0.2, 0.6, 1.0, 0.6, 0.3, 0.2 and 0.7. (The origin of the discrepancies between the frequencies of the low frequency modes reported by the two groups is not clear [35]).

Since a Franck-Condon factor of 0.05 for a pronounced intramolecular mode near  $730\text{ cm}^{-1}$  has been measured for the  $Q_y$ -transition of antenna Bchl *a* and Chl *a*, vide supra, and (from the same works) the Franck-Condon factors for modes with frequency lower than  $260\text{ cm}^{-1}$  are  $\leq 0.001$ , Franck-Condon factors of  $\approx 0.05$  for the 36, 71, 94 and  $127\text{ cm}^{-1}$  modes of P870 are plausible. However, such a value is still an order of magnitude lower than those obtained from the P870 band simulation of Palaniappan et al. Indeed, if the 105, 130 and  $140\text{ cm}^{-1}$  modes carried the large S-factor values reported by Palaniappan et al. one would expect to be able to observe their overtones and combinations since the above  $730\text{ cm}^{-1}$  mode with its S-factor of  $\sim 0.05$  is readily observed. As Palaniappan et al. state, they are not observed. One further point is that if the  $36\text{ cm}^{-1}$  Raman mode reported by Shreve et al. is real (the S/N ratio of the spectra is poor), it is far too sharp, vide supra, to be assignable to the low frequency phonons observed in the hole spectra. It may be due to the  $\sim 30\text{ cm}^{-1}$  acetyl torsion modes of BChl calculated by Palaniappan et al.

Given the above discussion and that the resonance Raman studies provide no proof that the observed low frequency discrete modes observed (assigned as intramolecular by Palaniappan et al.) make a significant contribution to P870, we are not inclined to change our assignment of the special pair marker mode as an intermolecular pseudo-localized phonon of the pair especially since charge-transfer states of stacked 1:1  $\pi$ -molecular donor-acceptor complexes are well known to couple very strongly to intermolecular modes of the complex [51]. The failure of resonance Raman to identify the distribution of low frequency phonons that couple to the  $P^* \leftarrow P$  transition cannot be overemphasized. This failure suggests that the marker



mode and its progression of P870 could be silent on the resonance Raman spectra because of the ultra-fast relaxation dynamics of the marker mode(s) and its overtones, vide supra.

## REFERENCES

1. Johnson, S. G.; Lee, I.-J.; Small, G. J. In *Chlorophylls*; Scheer, H., Ed.; CRC Press, Inc.: Boca Raton, Florida, 1991; pp. 739-768.
2. Reddy, N. R. S.; Lyle, P. A.; Small, G. J. *Photosyn. Res.* 1992, 31, 167.
3. Jankowiak, R.; Small, G. J. In *Photosynthetic Reaction Centers*; Deisenhofer, J., Norris, J., Eds.; Academic Press: New York, in press.
4. Singh, G. P.; Schink, H. J.; Lohneysen, H.; Parak, F.; Hunklinger, S. *Z. Phys.* 1984, B55, 23.
5. Yang, I.-S.; Anderson, A. C. *Phys. Rev. B* 1986, 34, 2942.
6. Frauenfelder, H.; Sligar, S. G.; Wolynes, P. G. *Science* 1991, 254, 1598.
7. Reddy, N. R. S.; Small, G. J. *J. Chem. Phys.* 1991, 94, 7545.
8. Reddy, N. R. S.; Small, G. J.; Seibert, M.; Picorel, R. *Chem. Phys. Lett.* 1991, 181, 391.
9. Reddy, N. R. S.; Picorel, R.; Small, G. J. *J. Phys. Chem.* 1992, 96, 6458.
10. Reddy, N. R. S.; Cogdell, R. J.; Zhao, L.; Small, G. J. *Photochem. Photobiol.*, accepted.
11. Johnson, S. G.; Small, G. J. *J. Phys. Chem.* 1991, 95, 471.
12. Tang, D.; Jankowiak, R.; Gillie, J. K.; Small, G. J.; Tiede, D. M. *J. Phys. Chem.* 1988, 92, 4012.
13. Tang, D.; Jankowiak, R.; Small, G. J.; Tiede, D. M. *Chem. Phys.* 1989, 131, 99.
14. Tang, D.; Johnson, S. G.; Hayes, J. M.; Jankowiak, R.; Tiede, D. M.; Small, G. J. *J. Phys. Chem.* 1989, 93, 5953.
15. Tang, D.; Johnson, S. G.; Jankowiak, R.; Hayes, J. M.; Small, G. J.; Tiede, D. M. In *Twenty-Second Jerusalem Symposium: Perspectives in Photosynthesis*; Jortner, J., Pullman, B., Eds.; Kluwer Academic Publ.: Boston, Massachusetts, 1990; pp. 99-120.

16. Johnson, S. G.; Tang, D.; Jankowiak, R.; Hayes, J. M.; Small, G. J.; Tiede, D. M. *J. Phys. Chem.* 1990, 94, 5849.
17. Reference 2 and references therein.
18. Small, G. J.; Hayes, J. M.; Silbey, R. J. *J. Phys. Chem.* 1992, 96, 7499.
19. Kolaczowski, S. V.; Lyle, P. A.; Small, G. J. In *Structure, Function and Dynamics of the Bacterial Reaction Center*; Breton, J., Ed.; Plenum Press: New York, NY, in press.
20. Gillie, J. K.; Small, G. J.; Golbeck, J. H. *J. Phys. Chem.* 1989, 93, 1620.
21. Fleming, G. R.; Martin, J.-L.; Breton, J. *Nature* 1988, 333, 190.
22. Breton, J.; Martin, J.-L.; Fleming, G. R.; Lambry, J.-C. *Biochem.* 1988, 27, 8276.
23. Jortner, J. *Biophys. Acta* 1980, 594, 193.
24. Vos, M. H.; Lambry, J. C.; Robles, S.; Youvan, D. C.; Breton, J.; Martin, J.-C. *Proc. Natl. Acad. Sci. U.S.A.* 1991, 88, 8885.
25. Zinth, W. *Ultrafast VIII*: Springer-Verlag: Berlin, 1992; abstract.
26. Holtzwarth, A. *Ultrafast VIII*: Springer-Verlag: Berlin, 1992; abstract.
27. Du, M.; Rosenthal, S. J.; Xie, X.; DiMagno, T. J.; Schmidt, M.; Schiffer, M.; Hanson, D. K.; Norris, J. R.; Fleming, G. R. *Proc. Natl. Acad. Sci. U.S.A.* 1992, 89, 8517.
28. Hayes, J. M.; Small, G. J. *J. Phys. Chem.* 1986, 90, 4928.
29. Hayes, J. M.; Gillie, J. K.; Tang, D.; Small, G. J. *Biochim. Biophys. Acta* 1988, 932, 287-305.
30. Won, Y.; Friesner, R. A. *Proc. Natl. Acad. Sci. U.S.A.* 1987, 84, 5511-5515.
31. Won, Y.; Friesner, R. A. *J. Phys. Chem.* 1988, 92, 2214; 1988, 93, 1007.
32. Lyle, P. A. *Ph.D. Dissertation*: Iowa State University, 1992.

33. Small, G. J. *J. Chem. Phys.* 1970, 52, 656 and many references therein.
34. Middendorf, T. R.; Mazzola, L. T.; Gaul, D. F.; Schenck, C. C.; Boxer, S. G. *J. Phys. Chem.* 1991, 95, 10142.
35. Palaniappan, V.; Aldema, M. A.; Frank, H. A.; Bocian, D. F. *Biochem.*, in press.
36. Galactic Industries Corp. Salem, N.H., U.S.A.
37. Bixon, M.; Jortner, J. *Chem. Phys. Lett.* 1989, 159, 17.
38. Sevian, H. M.; Skinner, J. L. *Theor. Chim. Acta* 1992, 82, 29.
39. Kanaya, T.; Kaji, K.; Ikeda, S.; Inoue, K. *Chem. Phys. Lett.* 1988, 150, 334.
40. Saikan, S.; Kishida, T.; Kanematsu, Y.; Aota, H., Harada, A.; Kamachi, M. *Chem. Phys. Lett.* 1990, 166, 358.
41. Furasawa, A.; Horie, K.; Mita, I. *Chem. Phys. Lett.* 1989, 161, 227.
42. Furasawa, H.; Horie, K.; Suzuki, T.; Machida, S.; Mita, I. *Appl. Phys. Lett.* 1990, 57, 141.
43. Buchenau, U.; Galperin, M.; Gurevich, V. L.; Parshin, D. A.; Ramos, M. A.; Schober, H. R. *Phys. Rev. B* 1992, 46, 2798.
44. Buchenau, U.; Zhou, H. M.; Nücker, N.; Gilroy, K. S.; Phillips, W. A. *Phys. Rev. Lett.* 1988, 60, 1318.
45. Lösche, M.; Feher, G.; Okamura, M. Y. *Proc. Natl. Acad. Sci. U.S.A.* 1987, 84, 7537.
46. Lockhart, D. J.; Boxer, S. G. *Proc. Natl. Acad. Sci. U.S.A.* 1988, 85, 107.
47. Parson, W. W.; Warshel, A. *J. Am. Chem. Soc.* 1987, 109, 6152.
48. Dlott, D. D. *Ann. Rev. Phys. Chem.* 1986, 37, 157-187 and references therein.
49. Donohoe, R.; Dyer, R. B.; Swanson, B. I.; Violette, C. A.; Frank, H. A.; Bocian, D. F. *J. Am. Chem. Soc.* 1990, 112, 6716.

50. Shreve, A. P.; Cherepy, N. J.; Franzen, S.; Boxer, S. G. and Mathies, R. A. *Proc. Natl. Acad. Sci. U.S.A.* 1991, 88, 11207.
51. Haarer, D.; Philpott, M. In *Spectroscopy and Excitation Dynamics of Condensed Molecular Systems*; Agranovich, V. M., Hochstrasser, R. M., Eds.; North-Holland Publ. Co.: Amsterdam, The Netherlands, 1983; pp. 29-80.

## SECTION CONCLUSIONS

The hole burning results obtained in this section confirm earlier results. The higher signal to noise ratio obtained in the current setup allowed for even more structure to be seen in the hole profiles than in previous experiments. Fitting the profiles proved to be difficult and has indicated that the current theory used is inadequate. One modification required in the hole simulation program is that the functional form of the phonon side band needs to have more contribution from the low energy phonons than is currently used. The need for more weighing of the low energy phonons comes from the temperature dependent data obtained in this study.

Zero phonon holes were obtained for the first time over the entire inhomogeneous width of the absorption profile. The zero phonon hole widths showed no dependence on wavelength and the range the holes were obtained over gave good agreement with the inhomogeneous value obtained during the hole simulations.

## SECTION REFERENCES

1. Deisenhofer, J.; Epp, O.; Miki, K.; Huber, R.; Michel, H. *J. Mol. Biol.* 1984, 180, 385
2. Deisenhofer, J.; Epp, O.; Miki, K.; Huber, R.; Michel, H. *Nature* 1985, 318, 618
3. Deisenhofer, J.; Michel, H. In *Annual Review of Cell Biology*, Spudich, J. A., Alberts, B. M., Palade, G. E., Eds.; Annual Reviews Inc.: Palo Alto; 1991, p.1
4. Allen, J. P.; Feher, G.; Yeates, T. O.; Rees, D. C.; Deisenhofer, J.; Michel, H.; Huber, R. *Proc. Natl. Acad. Sci. U. S. A.* 1986, 83, 8589
5. Chang, C. H.; Tiede, D. M.; Tang, J.; Smith, U.; Norris, J.; Schiffer, M. *FEBS Lett.* 1986, 205, 82
6. Yeates, T. O.; Komiyama, H.; Chirino, A.; Rees, D. C.; Allen, J. P.; Feher, G. *Proc. Natl. Acad. Sci. U. S. A.* 1988, 85, 7993
7. Kellog, E. C.; Kolaczowski, S.; Wasielewski, M. R.; Tiede, D. M. *Photosynth. Res.* 1989, 22, 47
8. Yeates, T. O.; Koyima, H.; Chirino, A.; Rees, D. C.; Allen, J. P.; Feher, G. *Proc. Natl. Acad. Sci. U. S. A.* 1988, 85, 7993
9. Michel, H.; Epp, O.; Deisenhofer, J. *EMBO J.* 1986, 3, 2445
10. Thompson, M. A.; Zerner, M. C. *J. Am. Chem. Soc.* 1990, 112, 7828
11. Zoller, M. J.; Smith, M. *Nucleic Acids Res.* 1982, 10, 468
12. Bylina, E. J.; Youvan, D. C. *Z. Naturforsch. C* 1987, 42, 769
13. DiMagno, T. J.; Norris, J. R. *Chemical Reviews* 1992, submitted
14. Shuvalov, V. A.; Duysens, L. N. M. *Proc. Natl. Acad. Sci. U. S. A.* 1986, 83, 1690
15. Holzappel, W.; Finkle, U.; Kaiser, W.; Oesterhelt, D.; Scheer, H.; Stiltz, H. U.; Zinth, W. *Proc. Natl. Acad. Sci. U. S. A.* 1990, 87, 5168

16. Parson, W. W.; Scherz, A.; Warshel, A. In *Antennas and Reaction Centers of Photosynthetic Bacteria*; Springer-Verlag: Berlin, 1985, 122
17. Breton, J.; Martin, J. -L.; Migus, A.; Antonetti, A.; Orszag, A. *Proc. Natl. Acad. Sci. U. S. A.* 1986, 83, 5121
18. Marcus, R. A. *Chem. Phys. Lett.* 1987, 133, 471
19. Bixon, M.; Jortner, J.; Michel-Beyerle, M. E.; Ogrondik, A.; Lersch, W. *Chem. Phys. Lett.* 1987, 140, 626
20. Creighton, S.; Hwang, J. -K.; Warshel, A.; Parson, W. W.; Norris, J. R.; *Biochemistry* 1988, 27, 774
21. Bixon, M.; Jortner, J.; Michel-Beyerle, M. E. *Biochim. Biophys. Acta* 1991, 1056, 301
22. Holzapfel, W.; Finkle, U.; Kaiser, W.; Oesterheld, D.; Scheer, H.; Stiltz, H. U.; Zinth, W. *Chem. Phys. Lett.* 1989, 160, 1
23. Martin, J. -L.; Breton, J.; Lambry, J. -C.; Fleming, G. R. In *The Photosynthetic Bacterial Reaction Center: Structure and Dynamics*; Plenum Press: New York, 1988; 195
24. Fleming, G. R.; Martin, J. -L.; Breton, J. *Nature* 1988, 333, 190
25. Alden, R. G.; Cheng, W. D.; Lin, S. H. Submitted
26. Kirmaier, C.; Holten, D.; Parson, W. W.; *Biochim. Biophys. Acta* 1985, 810, 49
27. Breton, J.; Martin, J. -L.; Fleming, G. R.; Lambry, J. -C. *Biochemistry* 1988, 27, 8276
28. Kirmaier, C.; Holten, D. *Proc. Natl. Acad. Sci. U. S. A.* 1990, 87, 3552
29. Boxer, S. G.; Lockhart, D. J.; Middendorf, T. R. *Chem. Phys. Lett.* 1986, 123, 476
30. Boxer, S. G.; Middendorf, T. R.; Lockhart, D. J. *FEBS Lett.* 1986, 200, 237
31. Johnson, S. G.; Tang, D.; Jankowiak, R.; Hayes, J. M.; Small, G. J.; Tiede, D. M. *J. Phys. Chem.* 1989, 93, 5953



32. Tang, D.; Johnson, S. G.; Jankowiak, R.; Hayes, J. M.; Small, G. J. In *Twenty Second Jerusalem Symposium Quantum Chemistry and Biochemistry: Perspectives in Photosynthesis*, Jortner, J., Pullman, B. Eds.; Kluwer Academic Publishers: Dordrecht; 1990, p. 99
33. Hayes, J. M.; Gillie, J. K.; Tang, D.; Small, G. J. *Biochim. Biophys. Acta* 1988, 932, 287
34. Johnson, S. G.; Tang, D.; Jankowiak, R.; Hayes, J. M.; Small, G. J.; Tiede, D. M. *J. Phys. Chem.* 1990, 94, 5849
35. Arfken, G. *Mathematical Methods for Physicists*; Academic Press Inc.: Orlando; 1985, p. 811
36. Middendorf, T. R.; Mazzola, L. T.; Gaul, D. F.; Schenck, C. C; Boxer, S. G. *J. Phys. Chem.* 1991, in press
37. *Handbook of Chemistry and Physics*, Beyer, H. B., Astle, M. J., Lide, D. R., Weast, R. C. Eds.; CRC Press Inc.: Boca Raton; 70<sup>th</sup> edition, 1989 - 1990, p. A-83

## GENERAL CONCLUSIONS

Pump probe and hole burning spectroscopies were used in this work to study photosynthetic antenna and bacterial reaction center dynamics. The research focused on determining how electronic excitation and initial charge separation occurs in these systems. Theoretical models were defined and used to simulate the data obtained and determine how well the present assumptions used in the models can successfully describe the systems.

Pump probe studies in section I on *Prosthecochloris aestuarii* led to a possible model for electronic excitation transport (EET). Relaxation between exciton components occurs in approximately 100 fs at 4.2 K. EET hopping to adjacent subunits from the one in which excitation localizes takes between 2 and 4 ps. Thermalization was shown to be complete within 2 ps. General forms of the polarized time dependent profiles for chromoproteins in solution and in oriented monolayers were also described in section I. The results of simulations with the equations show that the initial parallel to perpendicular ratio is always 3:1 regardless of the system. The simulations also show that complete depolarization can not arise from EET between chromophores in identical environments.

Chl a antenna of native photosystem I particles from spinach were used in section II to investigate temperature dependent polarized photobleaching dynamics. The results show different temperature sensitivities for the isotropic and anisotropic decays. Between 290 K and 38 K the anisotropic decay is lengthened by one order of magnitude while the isotropic shows very little temperature dependence. A multiphonon excitation theory was described

and used along with pertinent hole burning data to show that EET is phonon assisted with a frequency of  $20\text{ cm}^{-1}$  and a coupling strength of 0.8.

Section III detailed theoretical models for simulating hole spectra. Both a zero temperature limit expression and a more general temperature dependent expression were derived. The low temperature expression was used to simulate photochemical hole burning results from reaction centers of the purple bacterium *Rhodobacter sphaeroides*. The data showed the invariance to the burn frequency of the ZPH width within the inhomogeneous distribution. Temperature dependent studies of the ZPH width were also shown to be invariant between 1.6 and 8.0 K. The superior signal to noise obtain in the study confirmed earlier hole burning results on reaction centers and allowed more structure to be seen in the hole profiles than was possible in earlier studies. The simulations and temperature dependent data show that the modeling of the low frequency phonon distribution is inadequate.

## GENERAL REFERENCES

1. Hall, D. O.; Rao K. K. In *Photosynthesis*; Edward Arnold: Baltimore, 1974
2. Wraight, C. A.; Clayton, R. K. *Biochim. Biophys. Acta* 1974, 33, 246
3. Parson, W. W.; Clayton, R. K.; Cogdell, R.J. *Biochim. Biophys. Acta* 1975, 387, 265
4. Stryer, L. In *Biochemistry*; W. H. Freeman and Company: New York, 1988, p. 517
5. Golbeck, J. H. *Biochim. Biophys. Acta* 1987, 895, 167
6. Golbeck, J. H.; Bryant, D. A. In *Current Topics in Bioenergetics*; Lee, C. P. Ed.; Academic Press: New York, 1991, p 83.
7. Gregory, R. P. F. In *Photosynthesis*; Chapman and Hall: New York, 1989
8. Zuber, H.; Brunisholz, R.; Sidler, W. In *Photosynthesis. New Comprehensive Biochemistry*, Vol. 15; Ames, J. Ed.; Elsevier: Amsterdam, 1987, p. 223
9. Deisenhofer, J.; Epp, O.; Miki, K.; Huber, H. *J. Mol. Biol.* 1984, 180, 385
10. Michel, H.; Deisenhofer, J. *Chemica Scripta* 1987, 27B, 173
11. Deisenhofer, J.; Michel H. In *Annual Review of Cell Biology*, Spudich, J. A., Alberts, B. M., Palade, G. E. Eds.; AnnualReviews: Palo Alto, 1991
12. Chang, C.-H.; Tiede, D.; Tang, J.; Smith, U.; Norris, J. R.; Schiffer, M. *FEBS Lett.* 1986, 205, 82
13. Chang, C. -H.; El-Kabbani, O.; Tiede, D.; Norris, J. R.; Schiffer, M. *Biochemistry* 1991, 30, 5352
14. Woodbury, N.W.; Becker, M.; Middendorf, D.; Parson, W. W. *Biochemistry* 1985, 24, 7516
15. Paschenko, V. Z.; Korvatovskii, B. N.; Kononenko, A. A.; Charmorovsky, S. K.; Rubin, A. B. *FEBS Lett.* 1985, 191, 245
16. Martin, J. -L.; Breton, J.; Hoff, A.; Migus, A.; Antonetti, A. *Proc. Natl. Acad. Sci. USA* 1986, 83, 957

17. Rockley, M.; Windsor, M. W.; Codgell, R. J.; Parson, W. W. *Proc. Natl. Acad. Sci. USA* 1975, 72, 2251
18. Kaufmann, K. J.; Dutton, P. L.; Netzel, T. L.; Leigh, J. S.; Rentzepis, P. M. *Science* 1975, 188, 1301
19. Parson, W. W. *Biochim. Biophys. Acta* 1969, 189, 384
20. Wraight, C. A. *Biochim. Biophys. Acta* 1977, 459, 525
21. Vermiglio, A.; Clayton, R. K. *Biochim. Biophys. Acta* 1985, 810, 49
22. DeVault, D.; Chance, B. *Biophys. J.* 1965, 6, 825
23. DeVault, D.; Parkes, J. H.; Chance, B. *Nature* 1967, 215, 642
24. Van Duyne, R. P.; Fischer, S. F. *Chem. Phys.* 1974, 5, 183
25. Levich, V. O. *Adv. Electrochem. Electrochem. Eng.* 1966, 4, 249
26. Grigororov, L. N.; Chernavskii, D. S. *Biofizika* 1972, 17, 195
27. Hopfield, J. J. *Proc. Natl. Acad. Sci. USA* 1974, 71, 3640
28. Jortner, J. J. *Chem. Phys.* 1976, 64, 4860
29. Kakitani, T.; Kakitani, H. *Biochim. Biophys. Acta* 1981, 635, 498
30. Marcus, R. A. *J. Chem. Phys.* 1956, 24, 966
31. Marcus, R. A. *J. Chem. Phys.* 1965, 43, 679
32. Marcus, R. A.; Sutin, N. *Biochim. Biophys. Acta* 1985, 811, 265
33. Bixon, M.; Jortner, J. *Chem. Phys. Lett.* 1989, 159, 17
34. Förster, T. *Naturwissenschaften* 1946, 33, 166
35. Dexter, L. J. *Phys. Chem.* 1953, 21, 836
36. DeVault, D. In *Quantum-Mechanical Tunneling in Biological Systems*, 2nd Edn.; Cambridge University Press: New York, 1984

37. Blankenship, R. E.; Parson, W. W. In *Photosynthesis in Relation to Model Systems*; Barber, J., Ed.; Elsevier/North-Holland: Amsterdam, 1979, p. 71
38. Buhks, E.; Bixon, M.; Jortner, J. *Chem. Phys.* 1981, 55, 41
39. Bixon, M.; Jortner, J. *J. Phys. Chem.* 1986, 90, 3795
40. Fleming, G. R.; Martin, J. L.; Breton, J. *Nature* 1988, 333, 190
41. Chan, C.-K.; Chen, L. X.-Q.; DiMagno, T. J.; Hanson, D. K.; Nance, S. L.; Schiffer, M.; Norris, J. R.; Fleming, G. R. *Chem. Phys. Lett.* 1991, 176, 366
42. Bixon, M.; Jortner, J. *Chem. Phys. Lett.* 1989, 159, 17
43. Frauenfelder, H.; Hartmann, H.; Karplus, M.; Kuntz, Jr., D.; Kuriyan, J.; Parak, F.; Petsko, G. A.; Ringe, D.; Tilton, Jr., R. F.; Connolly, M. L.; Max, N. *Biochemistry* 1987, 26, 254
44. DiMagno, T. J. Ph. D. Dissertation, Department of Chemistry, The University of Chicago, 1991
45. Small, G. J.; Hayes, J. M.; Silbey, R. J. Submitted 1992
46. Englman, R.; Jortner, J. *Molec. Phys.* 1970, 18, 145
47. Allen, R. G.; Cheng, W. D.; Lin, S. H. Submitted 1992
48. Warshel, A. *Proc. Natl. Acad. Sci. USA* 1980, 77, 3105
49. Jortner, J. *Biochim. Biophys. Acta* 1980, 594, 193
50. Miller, J. R. In *Electron Transfer in Inorganic, Organic, and Biological Systems*; Bolton, J. R., Mataga, N., Mclendon, G. Eds.; American Chemical Society: Washington, 1991, p. 267
51. Vos, M. H.; Lambry, J.-C.; Robles, S. J.; Youvan, D. C.; Breton, J.; Martin, J.-L. *Proc. Natl. Acad. Sci. USA* 1991, 88, 8885
52. Vos, M. H.; Lambry, J.-C.; Robles, S. J.; Youvan, D. C.; Breton, J.; Martin, J.-L. *Proc. Natl. Acad. Sci. USA* 1991, 89, 613
53. Tang, D.; Johnson, S. G.; Jankowiak, R.; Hayes, J. M.; Small, G. J.; Tiede, D. M. In *Perspective in Photosynthesis*; Jortner, J., Pullman, B., Eds.; Kluwer Academic Press: London, 1990, p. 23

54. Marcus, R. A.; Almeida, R. *J. Phys. Chem.* 1990, 94, 2973
55. Almeida, R.; Marcus, R. A. *J. Phys. Chem.* 1990, 94, 2978
56. Jean, J.; Freisner, R. A.; Fleming, G. R. *Ber. Bunsenges. Phys. Chem.* 1991, 95, 253
57. Booth, P. J.; Crystall, B.; Giorgi, L. B.; Barber, J.; Klug, D. R.; Porter, G. *Biochim. Biophys. Acta* 1990, 1016, 141
58. Woodbury, W. T.; Parson, W. *Biochim. Biophys. Acta* 1984, 767, 345
59. Goldstein, R. A.; Takiff, L.; Baxer, S. G. *Biochim. Biophys. Acta* 1988, 934, 253
60. Mullet, J. E.; Burke, J. J.; Arntzen, C. J. *Plant Physiol.* 1980, 65, 814
61. Golbeck, J. H. *Methods in Enzymol.* 1980, 69, 129
62. Causgrove, T. Ph. D. Dissertation, Department of Chemistry, Iowa State University, 1989
63. Couillard, B.; Fossati-Bellani, V. *Lasers & Applications* 1985, 4, 91
64. Hayes, J. M.; Small, G. J. *Chem. Phys.* 1978, 27, 151
65. Small, G. J. In *Spectroscopy and Excitation Dynamics of Condensed Molecular Systems*; Agranovich, V. M., Hochstrasser, R. M., Eds.; North-Holland: Amsterdam, 1983, p. 515
66. Johnson, S. G.; Tang, D.; Jankowiak, R.; Hayes, J. M.; Small, G. J.; Tiede, D. M. *J. Phys. Chem.* 1990, 94, 5849
67. *Persisitent Spectral Hole Burning: Science and Applications*; Moerner, W. E., Ed.; Springer-Verlag: West Berlin, 1988
68. Freidrich, J.; Haarer, D. *Angew. Chem., Int. Ed. Engl.* 1984, 23, 113
69. Völker, S, In *Relaxation Processes in Molecular Excited States: Optical Relaxation Processes at Low Temperature*, Funfschilling, J., Ed.; Kluwer Academic Press: Dordrecht; 1989, p.113
70. Hayes, J. M.; Gillie, J. K.; Tang, D.; Small, G. J. *Biochim. Biophys. Acta* 1988, 932, 287

## ACKNOWLEDGEMENTS

I would first like to thank my co-research advisors Prof. Gerald Small and Prof. Walter Struve for allowing me to take on a dual project. Without their guidance, support, and insight the work presented here would not have been possible. Thus this work is as much theirs as it is my own.

There are also a multitude of former and present group members without whose help would have made research life a lot harder. First in Prof. Struve's group I would like to thank Tim Causgrove for showing me the ropes in the pump probe lab. To Sandy Bellefeuille and Shumei Yang for their friendship in my early research career. I would also like to thank the two postdoctoral students Herbert van Amerongen and Su Lin for their help in my last research projects.

In Prof. Small's group I would like to thank Kevin Gillie for breaking me in with my first experiments in hole burning. Dr. John Hayes for his guidance in the use and working of the hole simulation programs and hole theory, and to Dr. Ryszard Jankowiak for discussions of the bacterial reaction centers. Thanks must also go to postdoctoral students Raja Reddy and Steve Kolaczowski for all their help in working out experimental details.

A general thanks to Luchuan Shu, Inja Lee, Wook-Hyun Kim, Chuck Smith, and Hai Chou Chang for keeping the research atmosphere a good one to work in.

A large thank you also goes to William E. Catron whose Graduate Scholarship over the last three years of my research helped me to pursue my course of research.



Most importantly, I thank my wife Kari for her love and support during the last five years and forcing me to take much needed breaks from my research, and to my family whose support in my early school days prepared me for what was to come.

**APPENDIX A: RATE EQUATION PROGRAMS**

Following are the two programs used to fit the temperature dependent data of PSI-200 described in the paper of Section II. The first program was used to fit to the localized model which was deemed most reasonably able to fit the data. The source of the equation used is specified and the calculation is straight forward. Since in the localized model the same values of the Huang Rhys factor and vibrational frequency were used, these values were combined when convenient in the program. Otherwise the program logic is straight forward.

The second program is a very similar program that was used to fit the to the delocalized model. The delocalized model uses only one frequency and Huang Rhys factor as opposed to the localized model which used two values of each. Since the programs are so similar I have only commented in the second program where differences occur from the first program.

## LOCALIZED MODEL CALCULATION

- c This program uses the modified Bessel function to fit
- c temperature dependent, energy transport data, to equation 3a
- c found in the paper by J. Jortner, *J. Chem. Phys.* 64, 12, 4860

DIMENSION B(2)

- c ALPHA is equal to  $2\pi V^2/(\hbar^2\omega)$ . Where  $\omega$  is the frequency of the
- c relevant mode and V the coupling matrix element between acceptor
- c and donor configurations.

TYPE\*, 'INPUT ALPHA'  
ACCEPT\*, ALPHA

- c BETA holds the Huang Rhys factor for the vibrational mode.

TYPE\*, 'INPUT BETA'  
ACCEPT\*, BETA

- c P1 is the number of phonons required to make up the energy gap
- c for the vibration  $\hbar\omega$ .

TYPE\*, 'INPUT P'  
ACCEPT\*, P1

- c ZW is the frequency of the mode.

TYPE\*, 'INPUT HW'  
ACCEPT\*, ZW

B(1)=ALPHA  
B(2)=BETA

CALL RATE(B,P1,ZW)  
STOP  
END

c The B array holds the Huang Rhys factor in B(2) and in B(1) the  
c prefactor for the rate equation (Alpha in this program). ZBES is  
c an array that holds values of the modified Bessel function for  
c each possible value of the energy gap from zero to P1 phonons.

$$\text{PHONON} = 1.0 / (\exp(ZW / (.6938 * Z)) - 1.0)$$

$$ZX = \exp(-2.0 * B(2) * (2.0 * \text{PHONON} + 1.0))$$

$$ZV=((\text{PHONON}+1.0)/\text{PHONON})^{**}(\text{P1}/2.0)$$

c Calculate the modified Bessel function for each phonon from zero  
c to P1 and store in ZBES.

```

DO 300 JM=0,P1
  P2=JM
  ZBES(JM+1)=0.0
  ZBES(JM+1)=BESS1(PHONON,B,P2,ZW)
300 CONTINUE

```

c Multiply together the appropriate combinations of the modified  
c Bessel functions according to how many of each is required to  
c make up the energy gap and sum.

```

      ZP=0.0
      DO 325 JK=0,P1
        ZP=ZP+(ZBES(JK+1)*ZBES(P1-JK+1))
325    CONTINUE

```

c F is the rate. 1/F and the temperature are then written to the  
c file.

```
F=B(1)*ZX*ZP*ZV
WRITE 500, Z, 1.0/F
```

350 CONTINUE

**CLOSE(UNIT=1)**

```
500  FORMAT(F7.2,X,F10.5)
      RETURN
      END
```

[illegible]

c FUNCTION BESS1(COMPUTES VALUE OF MODIFIED BESSEL FUNCTION) See  
c *Handbook of Mathematical Functions*, M. Abramowitz and I.A. Stegun page  
c 375, equation number 9.6.10

```

FUNCTION BESS1(PHONON,B,P1,ZW)
DIMENSION B(2),ZNUM(50)
ZQ=0.0

```

- c Z is the operand of the modified Bessel function. ZQ is the  
c value required to calculate the modified Bessel function.

```

Z=2.0*B(2)*SQRT((PHONON*(PHONON+1.0)))
ZQ=(Z/2.0)**P1

```

- c End initializations. Start calculation.

```

BESS1=0.0

```

- c 40 was deemed enough iterations to get convergence.

```

DO 200 JK=0,40
  ZNUM(1)=1.0
  IF (JK.GT.0) THEN
    DO 100 JY=1,JK
100      ZNUM(JY)=(Z*Z/4.0)
    END IF
    DO 110 JL=2,JK
      ZNUM(JL)=ZNUM(JL)/(JL*JL)
110    CONTINUE
    ZA=0.0
    IA=0
    ZA=(P1+JK)
    IA=INT(ZA)
    ZNUM1=1.0
    IF (JK.EQ.0) THEN
      DO 120 JO=2,IA
        ZNUM(1)=ZNUM(1)/JO
120      CONTINUE
        ZNUM1=ZNUM(1)
      ELSE
        IB=JK-1
        DO 130 JO=JK+1,IA
          IB=IB+1
          ZNUM(IB)=ZNUM(IB)/JO

```

```
        IF (IB.EQ.JK) THEN
            IB=0
        ENDIF
130     CONTINUE
    END IF
    DO 140 JS=1,JK
        ZNUM1=ZNUM(JS)*ZNUM1
140     CONTINUE
        BESS1=ZNUM1+BESS1
200 CONTINUE

    BESS1=BESS1*ZQ
    RETURN
    END
```

## DELOCALIZED MODEL CALCULATION

```
c This program uses the modified Bessel function to fit
c temperature dependent, energy transport data, to equation 4
c found in the paper by J. Jortner, J. Chem. Phys. 64, 12, 4860
```

## DIMENSION B(2)

```
TYPE*, 'INPUT ALPHA'
ACCEPT*, ALPHA
```

```
TYPE*, 'INPUT BETA'
ACCEPT*, BETA
```

```
TYPE*, 'INPUT P'
ACCEPT*, P1
```

TYPE\*, 'INPUT HW'  
ACCEPT\*, ZW

**B(1)=ALPHA**  
**B(2)=BETA**

```
CALL RATE(B,P1,ZW)
STOP
END
```

[illegible]

```

SUBROUTINE RATE(B,P1,ZW)
DIMENSION B(2)

```

```
OPEN(UNIT=1, FILE='TEMP7.DAT', STATUS='NEW')
```

DO 350 J=10, 300, 10  
ZV=0.  
ZP=0.



```
PHONON=0.  
ZX=0.  
Z=FLOAT(J)
```

- c At this point I can calculate the rate in a straight forward  
c manner since only one value exists for the number of phonons.

```

      PHONON=1/(EXP(ZW/(.6938*Z))-1)
      ZX=EXP(-B(2)*(2*PHONON+1))
      ZV=((PHONON+1)/PHONON)**(P1/2)
      ZP=0.
      ZP=BESS1(PHONON,B,P1,ZW)
      F=B(1)*ZX*ZP*ZV
      WRITE (500,UNIT=1) Z, 1.0/F
350  CONTINUE

```

```

CLOSE(UNIT=1)
500  FORMAT(F7.2,X,F10.5)
      RETURN
      END

```

[illegible]

- c Function bess1 (computes value of modified Bessel function)**

```
REAL FUNCTION BESS1(PHONON,B,P1,ZW)
DIMENSION B(2),ZNUM(50)

ZQ=0.
Z=2*B(2)*SQRT((PHONON*(PHONON+1)))
ZQ=(Z/2)**P1
```

- c End initializations. Start calculation.**

```

BESS1=0.
DO 200 JK=0,40
    ZNUM(1)=1.
    IF (JK.GT.0) THEN
        DO 100 JY=1,JK
100        ZNUM(JY)=(Z*Z/4)

```

```

      END IF
      DO 110 JL=2,JK
        ZNUM(JL)=ZNUM(JL)/(JL*JL)
110    CONTINUE
      ZA=0.
      IA=0
      ZA=(P1+JK)
      IA=INT(ZA)
      ZNUM1=1.
      IF (JK.EQ.0) THEN
        DO 120 JO=2,IA
          ZNUM(1)=ZNUM(1)/JO
120    CONTINUE
          ZNUM1=ZNUM(1)
        ELSE
          IB=JK-1
          DO 130 JO=JK+1,IA
            IB=IB+1
            ZNUM(IB)=ZNUM(IB)/JO
            IF (IB.EQ.JK) THEN
              IB=0
            ENDIF
130    CONTINUE
          END IF
          DO 140 JS=1,JK
            ZNUM1=ZNUM(JS)*ZNUM1
140    CONTINUE
          BESS1=ZNUM1+BESS1
200  CONTINUE

      BESS1=BESS1*ZQ
      RETURN
      END

```

## APPENDIX B. HOLE CALCULATION PROGRAM

The following program was originally written by Dr. John Hayes to calculate hole profiles analytically in the short burn time limit according to equation 25 in our groups hole burning theory paper Hayes, J. M.; Gillie, J. K.; Tang, D.; Small, G. J.; *Biochim. Biophys. Acta* 1988, 933, 287. The program was modified by Dr. Inja-Lee to extend the calculation to arbitrary burn times by calculating the integrals of equations (11) and (12) of the introduction of Section III for the single mode case. Dr. Hayes extended the program further to include a second mode and Dr. Luchuan Shu added the normalization required to use a lorentzian high energy side and gaussian low energy side phonon line shape.

My contribution to the program was two fold. First I extended the program to three modes so that I could explore the possible causes of the increased structure of the deuterated rection center from *Rb. sphaeroides*. The second contribution was to increase the computational speed of the program. As originally programmed the three mode caculation took nearly 100 minutes to execute. By precalculating several expressions, analyzing and fixing the slowest parts of the program with the help of Jim Coyle from the computation center here on campus, and analyzing the actual tolerances of the integration range required, the computation time was dropped to three minutes.

The program is divided into five subsections. Namecheck checks the output file name to ensure that one does not overwrite an already existing file. Bode calculates the weighting factors required to do the integration bode's rule. Precalc precalcualtes all complicated or

---

time consuming calculations that are only required once during the run time of the program. Burn calculates the part of equation (12) that has to do with the exponential function. Hole calculates the rest of equations (11) and (12). The program is liberally commented indicating what is being calculated and why. At times helpful guides are included as to what ranges of values will give the best results.

---

# PROGRAM HOLEPROFILE

```
PRINT *, 'NUMBER OF PHONON OVERTONES, & BOTH MM OVERTONES:'
READ (5,*) M,NV,MM
```

```
PRINT*, 'ENTER NUMBER OF INTEGRATION POINTS:'  
READ(5,*) NINT
```

```
CALL NAMECHECK
CALL BODE(NINT)
CALL PRECALC(M,NV,MM)
CALL BURN(NINT,M,NV,MM)
CALL HOLE(NINT,M,NV,MM)
END
```

[illegible]

c See *Handbook of Mathematical Functions*, M. Abramowitz and I.A. Stegun page 886, equation number 25.4.14 for details concerning the form of bodes rule.

```

SUBROUTINE BODE(NINT)
IMPLICIT DOUBLE PRECISION(A-H,O-Z)

```

```
c The V array is used to hold the integration points. The WT
c array holds the weighting for each of the V points according
c to bode's approximation.
```

COMMON /INTE/ V(1000),WT(1000)

c The integration range required is solely based on the width  
c used for the inhomogeneous gaussian function. This is because  
c since all of the functions are multiplied together, if any  
c one of them is zero for a given point the whole calculation  
c is zero. Three standard deviations of a gaussian gives 99%  
c of its total area (Actually this will over estimate the needed  
c integration range since the FWHM is related to the standard deviation  
c by  $2(2\ln(2))^{1/2}\sigma$ . Therefore, if the inhomogeneous width is  
c  $100\text{ cm}^{-1}$  the proper integration range is  $-150\text{ cm}^{-1}$  to  $150\text{ cm}^{-1}$

- c (the center of the site distribution function is defined in
- c this program to be 0 cm<sup>-1</sup>). The number of integration points
- c (NINT) is dependent on the parameters of the calculation.
- c However normal ranges are from 75 to 200 points.

```
PRINT*, 'ENTER INTEGRATION RANGE: VINI,VFIN:'
READ (5,*) VINI,VFIN
```

- c XDIF is the increment of the integration points.

```
XDIF=(VFIN-VINI)/(NINT*4.0d0)
```

- c The following are the weightings for bode's rule

```
CN0=14.0d0/45.0d0
CN1=64.0d0/45.0d0
CN2=24.0d0/45.0d0
CN3=64.0d0/45.0d0
CN4=14.0d0/45.0d0
```

- c The following loads the V and WT arrays with there values.

```
I=1
V(I)=VINI

DO 20 K=1,NINT
  WT(I)=CN0*XDIF
  I=I+1
  V(I)=V(I-1)+XDIF
  WT(I)=CN1*XDIF
  I=I+1
  V(I)=V(I-1)+XDIF
  WT(I)=CN2*XDIF
  I=I+1
  V(I)=V(I-1)+XDIF
  WT(I)=CN3*XDIF
  I=I+1
20  V(I)=V(I-1)+XDIF

  WT(I)=CN4*XDIF
```

```
DO 30 K=1,NINT-1
  WT(I)=WT(I)+CN4*XDIFF
  I=I+4
```

[illegible]

## IMPLICIT DOUBLE PRECISION(A-H,O-Z)

```
c The RNL array holds nine precalculated values for up to three
c modes for later use in BURN and HOLE. GZPL holds two pre-
c calculated for the zero phonon line calculations. PI holds
c the value pi and XLG2 the log(2). The FACT array holds the
c inverse of the factorials of the integers from 0 to 10.
```

```
COMMON /BS/ RNL(10,10,10,9),GZPL(10,10,2)
COMMON /CONST/ PI,XLG2
DIMENSION FACT(11)
```

c S is the Huang Rhys factor for the low frequency mode. ZPL  
c is the zero-phonon line width.

```
PRINT*, 'ENTER HUANG-RHYS FACTOR AND ZPL:'  
READ(5,*) S,ZPL
```

c WM is the mean phonon frequency. GRG is the gaussian full  
c width at half maximum (FWHM) for the low energy side of the  
c phonon line shape, and GRL the lorentzian FWHM for the high  
C side.

```

PRINT*, 'ENTER PHONON FREQUENCY, HALF-WIDTH G, &
        HALF-WIDTH L:'
READ(5,*) WM,GRG,GRL

```

- c SSP is the Huang Rhys factor for the first marker mode and
- c SSP2 that of the second one. OMEGASP is the frequency of
- c the first marker mode and OMEGASP2 the frequency of the
- c second. GAMMASP is the broadening factor for the overtone
- c zero phonon line.

```

PRINT*, 'ENTER MM HUANG-RHYS FACTORS, FREQUENCIES,
        & BROADENING:'
READ(5,*) SSP,SSP2,OMEGASP,OMEGASP2,GAMMASP

```

```

PI=ATAN(1.0d0)*4.0d0
PIO2=PI*0.5d0
XLG2=LOG(2.0d0)
CSQRT=SQRT(PI/XLG2)
CEXP=EXP(-S-SSP-SSP2)
FACT(1)=1.0d0

```

- c Calculate the factorials.

```

DO 5 I=1,10
    FACT(I+1)=FACT(I)*I
5    CONTINUE

DO 6 I=1,11
    FACT(I)=1.0d0/FACT(I)
6    CONTINUE

```

- c Calculate the prefactors for the zero phonon line.

```

DO 7 JV=1,NV
    V1=JV-1
    DO 8 JT=1,MM
        Z1=JT-1
        GZPL(JT,JV,1)=(V1*GAMMASP+Z1*GAMMASP+ZPL)*0.5d0
        GZPL(JT,JV,2)=GZPL(JT,JV,1)/PI
        GZPL(JT,JV,1)=GZPL(JT,JV,1)*GZPL(JT,JV,1)
    
```



```

      RNL(JT,JV,1,8)=V1*OMEGASP+Z1*OMEGASP2
      RNL(JT,JV,1,9)=CEXP*(SSP**V1)*FACT(JV)*
1      (SSP2**Z1)*FACT(JT)

```

```

8      CONTINUE
7      CONTINUE

```

c Calculate the rest of the precalculations.

```

      DO 20 JR=2,M
        R1=JR-1

      DO 10 JV=1,NV
        V1=JV-1

      DO 30 JT=1,MM
        Z1=JT-1
        RNL(JT,JV,JR,3)=SQRT(R1)*GRL+V1*GAMMASP+Z1*GAMMASP
        RNL(JT,JV,JR,4)=SQRT(R1)*GRG+V1*GAMMASP+Z1*GAMMASP
        RNL(JT,JV,JR,1)=1.0d0/(PIO2+0.5d0*RNL(JT,JV,JR,4)/
1        RNL(JT,JV,JR,3)*CSQRT)
        RNL(JT,JV,JR,2)=2.0d0*RNL(JT,JV,JR,1)
        RNL(JT,JV,JR,5)=RNL(JT,JV,JR,2)/RNL(JT,JV,JR,3)
        RNL(JT,JV,JR,6)=(RNL(JT,JV,JR,1)*RNL(JT,JV,JR,3))*0.5d0
        RNL(JT,JV,JR,4)=(RNL(JT,JV,JR,4)*0.5d0)*(RNL(JT,JV,JR,4)
1        *0.5d0)
        RNL(JT,JV,JR,3)=(RNL(JT,JV,JR,3)*0.5d0)*(RNL(JT,JV,JR,3)
1        *0.5d0)
        RNL(JT,JV,JR,7)=-XLG2/RNL(JT,JV,JR,4)
        RNL(JT,JV,JR,8)=R1*WM+V1*OMEGASP+Z1*OMEGASP2
        RNL(JT,JV,JR,9)=CEXP*(S**R1)*FACT(JR)*(SSP**V1)*FACT(JV)
1        *(SSP2**Z1)*FACT(JT)

30      CONTINUE
10      CONTINUE
20      CONTINUE

      RETURN
      END

```

```

CCCCCCCCCCCCCCCCCCCCCCCCCCCCCCCCCCCCCCCCCCCCCCCCCCCCCCCCCCCC
CCCCCCCCCCCCCCCCCCCCCCCCCCCCCCCCCCCCCCCCCCCCCCCCCCCCCCCCCCCC

```

```
SUBROUTINE BURN(NINT,M,NV,MM)
```

```
IMPLICIT DOUBLE PRECISION(A-H,O-Z)
```

- c V and WT are previously described in BODE. RNL and GZPL are
- c previously described in PRECALC as are PI and XLG2.

```

COMMON /INTE/ V(1000),WT(1000)
COMMON /BS/ RNL(10,10,10,9),GZPL(10,10,2)
COMMON /CONST/ PI,XLG2

```

- c GINH is the inhomogeneous broadening of the single sites.

```

PRINT*, 'ENTER GINH:'
READ(5,*) GINH

```

- c TAU is the burn time. Since the prefactor for TAU is SQITD
- c and SUM the border line of the short burn time limit is
- c dependent on the inputs, but is typically 1E-06 to 1E-04.

```

PRINT*, 'ENTER BURN TIME:'
READ(5,*) TAU

```

- c WB is the burn wavelength relative to  $0 \text{ cm}^{-1}$ .

```

PRINT*, 'ENTER BURN WAVENUMBER:'
READ(5,*) WB

```

- c SQITD is a factor that takes into account the absorption
- c section, quantum yield, and burn intensity. Since tau is
- c variable this practically only serves to change the input
- c value of TAU (i.e., it doesn't matter what SQITD is).

```

SQITD=-4.4E04*TAU
PA1=(2.0d0/GINH)*SQRT(XLG2/PI)
GINH=GINH*0.5d0
GINH=1.0d0/GINH

```

c IF TAU is zero then we are going to calculate an absorption  
c spectrum only and can skip the BURN part of the program.

IF(TAU.EQ.0.0) THEN

DO 20 J=1,NINT\*4+1

ARG =-V(J)\*V(J)\*XLG2\*GINH\*GINH

WT(J)=WT(J)\*PA1\*EXP(ARG)

20 CONTINUE

c Otherwise we skip the above and calculate the number of sites  
c remaining at each wavelength following the burn.

ELSE

DO 30 J=1,NINT\*4+1

SUM1=0.0d0

ARG=-V(J)\*V(J)\*XLG2\*GINH\*GINH

PA=PA1\*EXP(ARG)

CON1=WB-V(J)

DO 31 MV=1,NV

DO 32 MT=1,MM

VV=CON1-RNL(MT,MV,1,8)

PB=GZPL(MT,MV,2)/(VV\*VV+GZPL(MT,MV,1))

SUM1=SUM1+RNL(MT,MV,1,9)\*PB

32 CONTINUE

31 CONTINUE

DO 50 MR=2,M

DO 40 MV=1,NV

DO 60 MT=1,MM

VV=CON1-RNL(MT,MV,MR,8)

IF(VV.GT.0) THEN

PB=RNL(MT,MV,MR,6)/(VV\*VV+

1 RNL(MT,MV,MR,3))

ELSE

ARG=VV\*VV\*RNL(MT,MV,MR,7)

PB=RNL(MT,MV,MR,5)\*EXP(ARG)

ENDIF

SUM1=SUM1+RNL(MT,MV,MR,9)\*PB

60 CONTINUE

40 CONTINUE

**50**      **CONTINUE**

c WT will end up holding the hole spectrum. The minus one in  
c with the EXP function serves to subtract off the absorption  
c spectrum so that we don't need to calculate the difference  
c of the pre and post-burn spectra.

```

30      WT(J)=WT(J)*PA*(EXP(SQITD*SUM1)-1)
        CONTINUE

```

```
ENDIF
RETURN
END
```

[illegible]

SUBROUTINE HOLE(NINT,M,NV,MM)

## IMPLICIT DOUBLE PRECISION(A-H,O-Z)

c All of the following parameters in the common statements have  
c been previously defined.

```
COMMON /INTE/ V(1000),WT(1000)
COMMON /BS/ RNL(10,10,10,9),GZPL(10,10,2)
COMMON /CONST/ PI,XLG2
```

c OINI is the calculation starting point, OFIN the ending  
c point, and OINC the increment.

```
PRINT*, 'ENTER CALCULATION RANGE: START, STOP, & INC:'  
READ(5,*) OINI, OFIN, OINC
```

c NPTS is the number of points to be calculated/

$$\text{NPTS} = ((\text{OFIN} - \text{OINI}) / \text{OINC}) + 1$$

c CUTOFF specifies a tolerance for the exponentials calculated  
c in the following loops. Because the exponential function is  
c a costly one to calculate (about 7 times slower than a normal

c multiplication) the exponential is not calculated if the  
 c value is close to zero. CUTOFF is not used in BURN because  
 c its use would not affect the run time very much. This is  
 c because BURN has far less loops than HOLE.

```
CUTOFF=LOG(1.0d-10)
OMEGA=OINI
```

```
DO 50 I=1,NPTS
  RINTENH=0.0d0
  DO 71 JV=1,NV
    DO 72 JT=1,MM
      Y=0.0d0
      CONA=GZPL(JT,JV,2)
      CONB=GZPL(JT,JV,1)
      DO 81 J=1,NINT*4+1
        VV=OMEGA-V(J)-RNL(JT,JV,1,8)
        PC=CONA/(VV*VV+CONB)
        Y=Y+WT(J)*PC
81      CONTINUE
        RINTENH=RINTENH+RNL(JT,JV,1,9)*Y
72      CONTINUE
71      CONTINUE
      DO 70 JR=2,M
        DO 80 JV=1,NV
          DO 90 JT=1,MM
            Y=0.0d0
            CON2 = RNL(JT,JV,JR,6)
            CON3 = RNL(JT,JV,JR,3)
            CON5 = RNL(JT,JV,JR,7)
            CON6 = RNL(JT,JV,JR,5)
            DO 100 J=1,NINT*4+1
              VV=OMEGA-V(J)-RNL(JT,JV,JR,8)
              CON7 = VV*VV
              IF (VV.GT.0) THEN
                PC=CON2/(CON7+CON3)
                Y=Y+WT(J)*PC
              ELSE
                ARG = CON7*CON5
                IF (ARG .GT. CUTOFF) THEN
                  PC=CON6*EXP(ARG)
```

```

      Y=Y+WT(J)*PC
      ENDIF
      ENDIF
100      CONTINUE
      RINTENH=RINTENH+RNL(JT,JV,JR,9)*Y
90      CONTINUE
80      CONTINUE
70      CONTINUE
      WRITE(1,*) OMEGA,RINTENH
      OMEGA=OMEGA+OINC
50      CONTINUE

      CLOSE(UNIT=1)
      RETURN
      END

```

[illegible]

### SUBROUTINE NAMECHECK

```

      CHARACTER*14 NAMF
800  PRINT*, 'ENTER OUTPUT FILE NAME: '
      READ (5,100) NAMF
100  FORMAT(A)

      OPEN (UNIT=1, FILE=NAMF, STATUS='OLD', FORM='FORMATTED',
1     ERR=802)

      CLOSE(UNIT=1)

      PRINT *, 'FILE NAME ALREADY IN USE:'

      GOTO 800
802  OPEN (UNIT=1, FILE=NAMF, STATUS='NEW', FORM='FORMATTED',
1     ERR=1000)

      RETURN
1000 PRINT *, 'BAD FILE SPEC, TRY AGAIN'
      GOTO 800
      END

```